Institute of Astronomy and NAO
Bulgarian Academy of Sciences

Title:

Magnetic activity in selected evolved stars

Svetla Valentinova Tsvetkova

A thesis submitted for the degree of Doctor of Philosophy in the field of "Astrophysics and Stellar Astronomy", code 01.04.02

PhD Advisor: Assoc. Prof. Dr. Renada Konstantinova-Antova

Sofia
2014

Contents

List of abbreviations

Abbreviation	Meaning
AGB	Asymptotic Giant Branch
CFHT	Canada-France-Hawaii Telescope
DI	Doppler Imaging
HRD	Hertzsprung-Russell Diagram
LSD	Least Squares Deconvolution method
RGB	Red Giant Branch
RV	Radial Velocity
S/N	Signal-to-Noise ratio
TBL	Télescope Bernard Lyot
ZDI	Zeeman Doppler imaging

Introduction

Variety of objects throughout the entire Hertzsprung-Russell diagram possess magnetic fields – from very low-mass dwarfs to very massive stars, from young star-forming molecular clouds and protostellar accretion discs to evolved giants and magnetic white dwarfs and neutron stars. These fields range from a few $\mu\ G$ in molecular clouds to $\sim 10^{12}\ G$ and more in magnetic neutron stars. In non-degenerate stars magnetic fields feature large-scale topologies varying from simple nearly-axisymmetric dipoles to complex non-axisymmetric structures, and from mainly poloidal to mainly toroidal topology (reviews by Berdyugina 2005, Donati & Landstreet 2009, Reiners 2012).

Magnetic fields may be of fossil nature, originating in the interstellar cloud from which the star forms, or generated through dynamo operation. These two theories are discussed in Sec. 1.4.

The existence of stellar magnetic fields could be manifested in a various of magnetic phenomena including starspots in the photosphere, chromospheric plages, network, coronal loops, flares, prominences, UV, X-ray and radio emission. Evolution of starspots on various time scales allows to study the stellar differential rotation, activity cycles and global magnetic fields.

The first detection of a magnetic field in a star was for the Sun. It was obtained one century ago by Hale (1908), who applied the Zeeman effect, which was discovered by Zeeman only 12 *yr* before the pioneering work of Hale. In 1947 Babcock discovered the simple large-scale field of the chemically peculiar star 78 Vir via the Zeeman effect (Babcock 1947). In the same year, Kron (1947) was the first who considered the hypothesis that spottedness of the stellar surface was the reason for periodic brightness variations, which cause distortions of the light curves, by studying the line profile variations in spectra of the RS CVn-type star AR Lac. The first Doppler image of a spotted star was obtained by Vogt & Penrod (1983) for the RS CVn star HR 1099.

Pulsars were detected for the first time through their radio emission (Hewish et al. 1968) with strengths of the magnetic fields of the order of 10^{12} G. Shortly afterwards, it was reported a detection of circularly polarized light from a white dwarf with magnetic field of about 10^7 G (Kemp et al. 1970).

The idea that rotation plays a crucial role in the generation of stellar activity in late-type stars was proposed by Skumanich (1972). Later, such relations have been reported between rotation and coronal emission (Pallavicini et al. 1981, Walter & Bowyer 1981), chromospheric CaII and $H\alpha$ emission (Vaughan et al. 1981, Middelkoop 1981, Mekkaden 1985), ultraviolet line fluxes (Vilhu 1984, Simon & Fekel 1987) and radio emission (Drake et al. 1989).

The first direct detections for magnetic fields on cool solar-type stars were obtained in 1980 (Robinson et al. 1980) for $G8V$ star ξ Boo A and $K0V$ star 70 Oph A.

Early programs for searching longitudinal magnetic fields in stars from all spectral classes were presented by Brown & Landstreet (1981), studying 26 stars, and Borra et al. (1984), studying about 50 stars. Both programs search for circular polarization using methods, which add information from many spectral lines in order to enhance the polarization signal. Unfortunately, they did not detect undoubtedly any polarization signals in late-type stars, confirming the belief that magnetic fields are very weak, because of flux cancellation and complicated field geometries.

Nowadays, there are many observational tools and diagnostic techniques for studying surface inhomogenities due to magnetic fields – long-term photometric observations reveal the evolution of active regions and stellar activity cycles; high-resolution spectroscopy along with the Doppler Imaging technique reveal the structure of active regions and stellar differential rotation; observations of molecular lines provide information about the spatially unresolved starspots (Berdyugina 2002) and their temperature (O'Neal et al. 1996); spectropolarimetry along with the Zeeman Doppler Imaging (ZDI) technique reveal the distribution of magnetic fields on the stellar surface; and the new proxies of interferometry, microlensing, astroseismology, etc.

The idea of using the ZDI for mapping the stellar surface was first formulated by Deutsch (1958) and applied to the star HD 125248. The first inversion technique was developed by Goncharskii et al. (1977) for mapping chemical peculiarities on the surface of the Ap star HD 124224.

The new high-resolution fiber-fed spectropolarimeters *MuSiCoS*, *Narval* and *ESPaDOnS*, which are dedicated to spectropolarimetry, give the rise of the studies of magnetic felds and activity in stars spread all over the HR diagram. The operation of *MuSiCoS* began in 1996 at the 2-m Télescope

Bernard Lyot (TBL) at Pic du Midi Observatory, France. A brief review of that instrument is given by Wade (2003). Later, in 2006, it was replaced by *Narval*, which has been working on till the present time (Sec. 2.2). The spectropolarimeter *ESPaDOnS* has been operating at the 3.6-m $CFHT$ since 2005 (Sec. 2.2). The observational data from these instruments (Stokes I and V and sometimes when is possible Stokes Q and U), combined with the powerful LSD and ZDI methods, reveals a lot of information about stellar magnetic activity.

Spectropolarimeters, which give access to the Southern Hemisphere, are SemelPol at the 3.9-m Anglo-Australian Telescope (AAT) and HARPSpol at the 3.6-m ESO telescope, La Silla, Chile (the second one commissioned in 2010).

Thesis structure

The structure of this thesis is as follows – Chapter 1 begins with a short introduction about different magnetically active stars and then continues with the structure and evolution of the red giants; lithium and $^{12}C/^{13}C$ ratio as indicators of the evolutionary stages in giants; the evolutionary hypotheses for the magnetic activity in fast and slowly rotating giants. Chapter 2 is a brief overview of the equipment and methods, which are used. The next two chapters contain the results of the study for three stars – for the two slowly rotating single giants β Ceti and EK Eri in Chapter 3, and for the fast rotating V390 Aur in Chapter 4. Then, the sections of Conclusions, Main contributions, List of publications, noticed citations and References follow.

Chapter 1

Red giants among the other magnetically active stars

This chapter begins with a short review about different magneticaly active stars. Then, the internal structure of the red giants and their evolution in the *Hertzsprung-Russell Diagram* (HRD) is given. Also, it is important to get additional information for these stars by finding the abundances of lithium and $^{12}C/^{13}C$ ratio, since they are key tracers of the evolutionary processes. Later, the main hypotheses for the magnetic activity of red giants are discussed – their magnetic fields are generated by a dynamo action or they are fossil fields, which originate in the interstellar cloud from which the star forms.

1.1 *Magnetically active stars*

Magnetism is spread all over the evolutionary stages, but a summary for the following non-degenerated magnetically active stars is given – pre-main sequence stars, Solar-type stars, M dwarfs, RS CVn, FK Com and single G, K and M giants.

Pre-main sequence stars

For the pre-main sequence stars T Tauri is believed that accretion of circumstellar material onto the stellar surface is controlled by the stellar magnetic field (Bouvier et al. 2007). There are two possible explanations for the origin of their magnetic fields – first one is that they may be generated by a dynamo, which could be similar to the one in low-mass M-type dwarfs,

because these two types of stars are deeply convective; the second one is that they may possess primordial fields, which are not yet dissipated, since these stars are young (few million years). Starspots, flare activity, accretion processes and stellar winds are the result of the existence of magnetic fields in T Tauri stars.

First measurements of magnetic field strengths in T Tauri stars were reported by Basri et al. (1992). A lot of stars have been studied since then. Magnetic maps from Stokes I and V, brightness maps and in addition a magnetospheric topology were reconstructed for many pre-main sequence stars. For examples: $K7$-type BP Tau (Donati et al. 2008 a), $G8$-type CV Cha and $K2$-type CR Cha (Hussain et al. 2009), $K5$-type V2129 Oph (Donati et al. 2011 a), $K5$-type V4046 Sgr (Donati et al. 2011 b), etc. The first two young early-G stars, for which the large-scale magnetic topologies have been determined are HD 171488 (Marsden et al. 2006) and HD 141943 (Marsden et al. 2011), both being $G2$-type.

Large-scale magnetic fields of these stars could be studied by Stokes V signatures from photospheric lines (for non-accreting regions of the stellar surface) and by Stokes V signatures from emission lines (for accreting regions). Average longitudinal fields from accreting regions typically reach several kG and display smooth and simple rotational modulation, suggesting a simple large-scale magnetic geometry. Longitudinal fields from the quiet photosphere rarely exceed a few hundred G and show complex Zeeman signatures, which reveal that the large-scale field is significantly more complex than a dipole and includes in particular a strong octupole component (Donati & Landstreet 2009).

It is considered that pre-main sequence stars may host distributed dynamo (Donati et al. 2003 a), i.e. dynamos that operate across the entire convective zone, which is much closer to the stellar surface than in the solar case. The strongest evidence for this are large regions of near-surface azimuthal magnetic field seen on such stars. These regions are believed to be the near-surface toroidal components of the large-scale dynamo field.

Examples of the magnetic and magnetospheric topologies are shown in Fig. 1.1 and Fig. 1.2 for the star BP Tau (Donati et al. 2008 a), which is still fully convective. Magnetic topology consists of a dominant dipole (with about 50 % of the magnetic energy concentrating in $l = 1$ modes and the corresponding dipole strength is about 1.2 kG), but also a strong octupole (with about 30 % of the magnetic energy concentrating in $l = 3$ modes and the corresponding octupole strength is about 1.6 kG), both slightly tilted with respect to the rotation axis. Accretion spots coincide with the two main magnetic poles at high latitudes and overlap with dark photospheric spots.

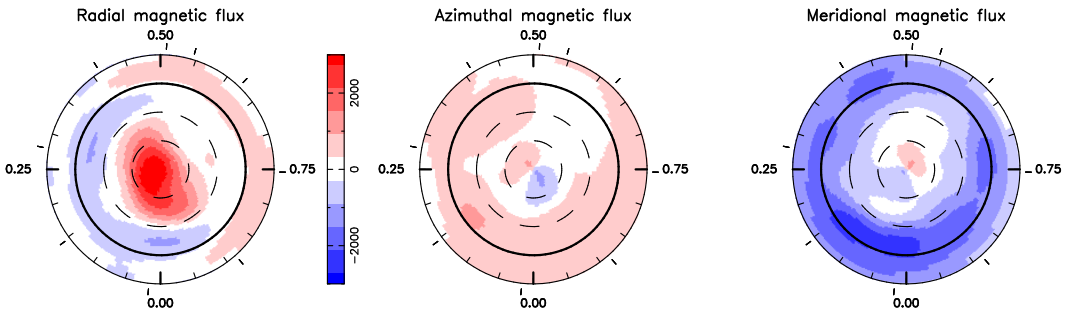

Figure 1.1: *Magnetic topology of BP Tau (Donati et al. 2008 a). The three components of the field in spherical coordinates are displayed with magnetic fluxes labelled in G.*

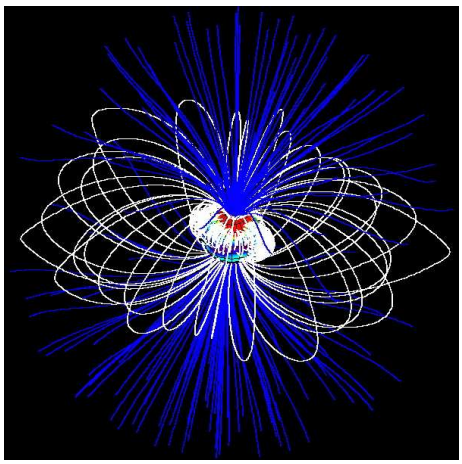

Figure 1.2: *Magnetospheric topology of BP Tau (Donati et al. 2008 a). The magnetosphere is assumed to expand up to the inner disc radius of* 7.5 $R\star$. *The star is shown at a rotational phase 0.0. The colour patches at the surface of the star represent the radial component of the field with red and blue corresponding to positive and negative polarities; open and closed field lines are shown in blue and white, respectively.*

The large-scale magnetic topology of the classical T Tauri star V2129 is rather complex and dominated by an octupole component ($l = 3$) and a weak dipole ($l = 1$) with strengths of about 1.2 and 0.35 kG, respectively, both slightly tilted with respect to the rotation axis (Donati et al. 2007). There is a 2 kG high latitude positive radial field spot. This star is no longer fully convective and hosts a small radiative core.

Solar-type stars

Solar-type stars are stars on the lower part of the main sequence, which show chromospheric activity (Wilson 1978). Measurements of the photometric variability, $H\alpha$ and CaII K&H emission lines suggest the existence of active regions with emission plages and dark spots, similar to that on the Sun (Dorren & Guinan 1982). Rotational modulation by active regions, which can persist for several rotation periods are described by Lockwood et al. (1984).

The first detections of Zeeman polarization signatures from solar-type stars were made by Donati et al. (1997). Some of the studied stars are – HD 190771 showing two types of evolution (polarity switches and conversion of magnetic energy from the toroidal to the poloidal field component)(Petit et al. 2009); ξ Bootis A showing a strong dominant toroidal field component and values of the surface-averaged longitudinal magnetic field B_l between about 5 and 11 G (Morgenthaler et al. 2012); and several stars from the sample of 19 FGK-type stars by Morgenthaler et al. (2011 a). Some of the stars were monitored for a period of several years and because of that they had more than one ZDI map reconstructed. In this way it is possible to trace the evolution of the surface magnetic fields. The main characteristics from these studies are that stars show complex magnetic structures and magnetic polarity reversals.

It is believed that in these stars operates the solar-like interface-layer dynamo – it is a dynamo, which operates in an interface layer between the convective and the radiative zones.

Examples of ZDI maps of solar-type stars are shown in Fig. 1.3 for ξ Bootis A, which is one of the 7 reconstructed maps of this star from the sudy of Morgenthaler et al. (2012), and in Fig. 1.4 for HD 190771 (Morgenthaler et al. 2011 a).

A "snapshot" survey of 170 solar-type stars, was carried out by Marsden et al. (2014), using high-resolution spectropolarimetric observations from *Narval* and *ESPaDOnS*. They detected a magnetic feld on the surface of 39 % of their targets. The values of the measured maximum unsigned longitudinal magnetic field are smaller than 10 G, in general.

M dwarfs

The early-M flare star AD Leo ($M4.5V$) is the first M-type star, which is Zeeman detected (Saar & Linsky 1985). These M-type stars are the lowest mass stars, from 0.08 $M_\odot$ to 0.50 $M_\odot$, and have radii of approximately half

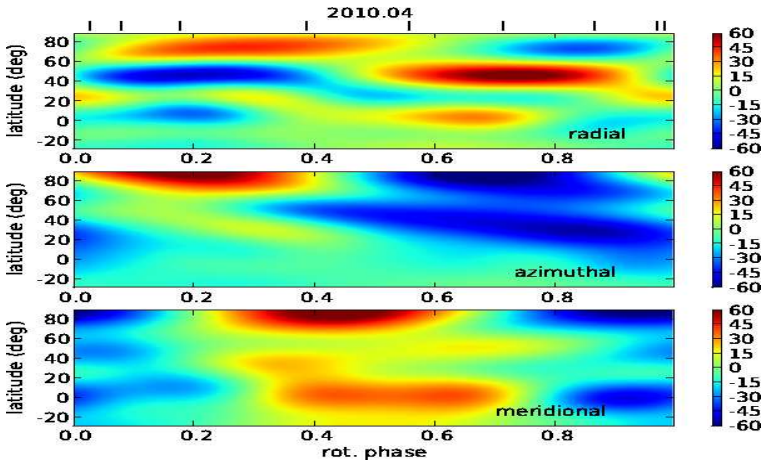

Figure 1.3: *A magnetic map of ξ Bootis A (Morgenthaler et al. 2012). From top to bottom are shown the radial, azimuthal and meridional field components. The magnetic field strength is expressed in Gauss.*

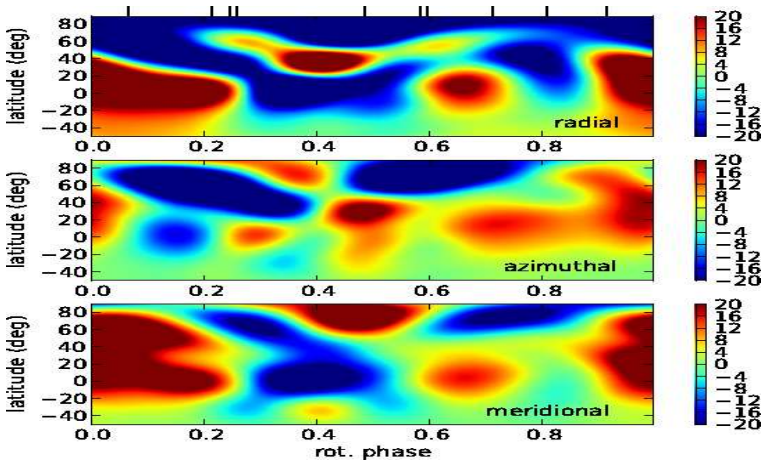

Figure 1.4: *Same as Fig. 1.3 for HD 190771 (Morgenthaler et al. 2011 a).*

a solar radius or less. Strong chromospheric and coronal emission and flares are the result of the existence of magnetic fields.

The transition from partly convective to fully convective stars happens around spectral type $M3/M4$. Cool stars with masses lower than 0.35 $M_{\odot}$ are fully convective.

In partly convective Sun-like stars, dynamo processes presumbly concentrate where differential rotation is strongest, at the interface layer, called

tachocline, between their radiative cores and convective envelopes. In fully convective stars there is no such a tachocline, even though these stars are able to trigger axisymmetric large-scale poloidal fields without differential rotation.

Spectropolarimetric data of $M4$ dwarf V374 Peg for almost three complete rotaion periods demonstrated that this fully convective star ($M = 0.28 \pm 0.05\ M_{\odot}$) hosts a strong mostly axisymmetric poloidal field despite rotating almost rigidly, in contradiction with theoretical expectations (Morin et al. 2008 a). The spot occupancies is of about 2 % of the overall photosphere. The magnetic topology of the star remains globally stable over a time-scale of 1 yr. The average field strength at the surface of the star is about 700 G.

A sequence of 3 papers, Donati et al. (2008 b), Morin et al. (2008 b) and Morin et al. (2010), study the magnetic topologies of M dwarfs from spectral classes from $M0$ to $M8$, which aim is to investigate observationally how dynamo processes operate in partly to fully convective stars (the threshold being $M3/M4$).

The first study of Donati et al. (2008 b) contains 6 early M dwarfs with spectral types ranging from $M0$ to $M3$ and masses in the interval $0.48 - 0.75\ M_{\odot}$. In 4 of these stars is detected significant differential rotation with a strength comparable to that of the Sun. The authors conclude that for stars with masses $M > 0.5\ M_{\odot}$ the large-scale magnetic topologies have much larger fraction of toroidal fields and a lower axisymmetric degree of poloidal fields, while for stars below $0.5\ M_{\odot}$ the poloidal field is largery dominant and axisymmetric. The stars from this survey have longitudinal magnetic fields ranging from about -110 G to about 100 G.

The second study of Morin et al. (2008 b) contains 5 stars of spectral type $\sim M4$, i.e. with masses close to the full convection threshold of $\simeq 0.35\ M_{\odot}$. All of these stars host mainly axisymmetric large-scale poloidal fields. Magnetic topologies are globally stable on time-scale 1 yr. The longitudinal magnetic fields of these stars are in the range from about -800 G to about 500 G. The magnetic topologies of fully convective stars considerably differ from those of the warmer and with radiative cores G and K stars, which usually host a srong toroidal component in the form of azimuthal field rings.

The third study of Morin et al. (2010) contains 11 fully convective late M dwarfs of spectral types $M5 - M8$ and with masses $0.08 - 0.22\ M_{\odot}$. It appears that the stars form two distinct categories of magnetic topologies – first group hosts strong axisymmetric dipolar fields, similar to mid M dwarfs, and second one hosts weak fields generally featuring a significant non-axisymmetric component and sometimes a significant toroidal one. The longitudinal magnetic fields are measured in the range from about -1800 G to about 100 G.

Magnetic maps were derived from time-series of Stokes I and V measurements for almost all the M dwarfs from the surveys, which are mentioned above. An example of ZDI map is shown in Fig. 1.5 of the $M6$ dwarf WX UMa (Morin et al. 2010). There is a strong polar cap of radial field of negative polarity. The reconstructed magnetic field is almost purely poloidal, mostly axisymmetric.

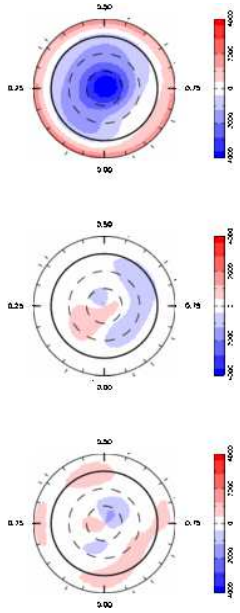

Figure 1.5: *A magnetic map of WX UMa (M6) (Morin et al. 2010). From top to bottom – radial, azimuthal and meridional field components.*

RS CVn and FK Com

RS CVn stars are close detached binaries – the primary component is more massive and is a G-K giant or subgiant and the secondary is a subgiant or dwarf of spectral classes G to M. This class of variable stars was proposed by Hall (1976), because of their photometric variability, strong CaII K&H emission lines and short orbital periods (2-14 days). Their activity consist of optical variability outside eclipse due to rotationally modulated effect of cool spots on their surfaces, emission cores in the CaII K&H resonance lines, strong chromospheric plages, UV, radio, X-ray and microwave emissions and flares.

Magnetic field measurements using ZDI of the active $K1$ component of the RS CVn system HR 1099 are presented by Donati et al. (1990). They report about a monopolar magnetic region with a mean field strength of about 985 G, which covers about 18 % of the total stellar surface and may be colocalized with a bright photospheric spot. This system, HR 1099, has been studied and mapped in continuous works by Donati (1999), Donati et al. (2003 a) and Petit et al. (2004 b) and the longitudinal magnetic field is measured of about 10 G. The latest authors, Petit et al. (2004 b), report about a detection of a weak surface differential rotaion and that the equator rotates faster than the pole, with a difference in rotation rate between the pole and the equator about four times smaller than that of the Sun. In all the studies, the star shows stable azimuthal field regions at photometric level, which indicates that the parent large-scale toroidal structure is not generated at the base of the convective zone, as in the Sun (Donati 1999). The author does not agree with the suggestions that these magnetic features represent the emergence of magnetic flux loops carried upwards either by granular convection or magnetic buoyancy, because if this is the case, the features would only be stable on very short time scales. But for HR 1099 they are observable in many rotational cycles. Even more, if the rising flux tubes come from the base of the convective zone, they are expected to emerge at high latitudes, but for HR 1099 they emerge at latitudes about 30°. The conclusion of Donati (1999) is that the global field is generated by a distributed dynamo, with both α- and ω- effects located within the convective zone (for HR 1099 the convective zone is as deep as 0.85 $R_\star$). Moreover, the author concludes that poloidal and toroidal field components have similar strengths, while for the Sun the poloidal field is several orders of magnitude smaller than the inferred toroidal component.

Through the ZDI, four more RS CVn systems out of sample of 9 are detected by Donati et al. (1992). A ZDI map of the $K2III$ primary of the RS CVn binary IM Peg is reconstructed by Berdyugina & Marsden (2006) showing both positive and negative radial and azimuthal fields.

The first detection of the linear polarization in line profiles of cool active stars is presented by Kochukhov et al. (2011) for the RS CVn binary HR 1099. They used all four Stokes parameters and the LSD method for measuring the magnetic field. The detected linear polarization in spectral lines has an amplitude of the order of 10^{-4} of the unpolarized continuum, which is about a factor of 10 lower than the amplitude of the circular polarization signal. Linear polarization for four more RS CVn stars is detected by Rosén et al. (2013).

Another studied and mapped RS CVn binary is II Peg ($K2IV$ primary and $M0-M3V$ secondary)(Kochukhov et al. 2013) by Stokes V signatures.

They observed the star in the period 2004-2010 and the study reveals complex topologies with mean longitudinal magnetic fields $50 - 100\ G$. According to the authors, the magnetic activity is due to an $\alpha^2 - \omega$ dynamo, but not due to a distributed dynamo like in HR 1099, because the contribution of the azimuthal fields of II Peg is relatively smaller than that of HR 1099. The surface magnetic field is highly non-axisymmetric and dynamically evolution over time is observed. That's why the operation of the dynamo should rely more strongly on the convective turbulence, called the α effect. One of the magnetospheric maps from that paper is shown in Fig. 1.6.

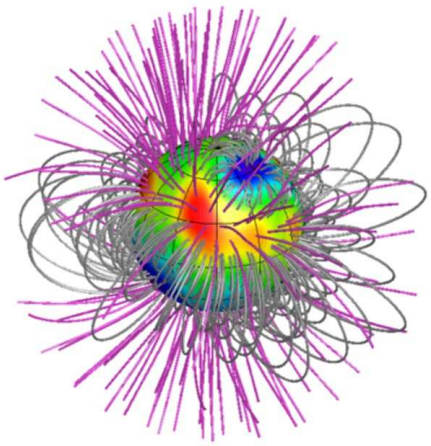

Figure 1.6: *Magnetospheric topology of II Peg (Kochukhov et al. 2013). The open and closed magnetic field lines are shown in different colours.*

FK Com stars were defined as a new group of active stars in the early 1980's (Bopp & Rucinski 1981, Bopp & Stencel 1981). FK Com stars are late-type giants with spectral types ranging from G to early K, rotation of only a few days and $v \sin i$ of about $50 - 100\ km/s$ (FK Com star itself has a $v \sin i = 155\ km/s$). This odd rapid rotation is explained by the scenario, in which these stars may represent the further evolution of W UMa contact binaries into a coalesced single star (Bopp & Rucinski 1981, Bopp & Stencel 1981). The magnetic activity is expresed by photometric variability, strong chromospheric emission in the CaII K&H and $H\alpha$ lines, cool spots, X-ray emission.

Several magnetic maps of the FK Com star HD 199178 ($G5$ subgiant primary) in the observational period 1998-2003 are reconstructed by Petit et al. (2004 a), showing that the magnetic feld is mainly azimuthal, suggesting that

the dynamo processes generating the magnetic activity of the star may be active very close to the stellar surface. Local short-term evolution of surface brightness and magnetic structures are observed on time-scales as short as a couple of weeks, but the largest features of the brightness and magnetic topologies remain stable over several years. Also, it is reported a solar-like differential rotation, with difference in rotation rate between equatorial and polar regions being about 1.5 times that of the Sun.

Single G, K and M giants

Single giants of spectral class G and K are another group of stars, which show magnetic activity. They possess large convective zones, potentially allowing the operation of a dynamo. Weak surface magnetic fields, ranging from a few gauss to a few tens of gauss, are detected in several single G and K giants, which are divided in two groups – fast and slowly rotating giants. Observational data is obtained with *Narval* and *ESPaDOnS* and magnetic activity is studied by Stokes V signatures.

Magnetic fields in several fast rotating giants of spectral classes $G5 - G9$ are detected by Konstantinova-Antova et al. (2008 a, b, 2009). Their $v \sin i$ values are in the interval $9 - 29\ km/s$ and have masses in the interval $1.9 - 4.2\ M_{\odot}$. Their measured longitudinal magnetic fields vary from about $-16\ G$ to about $6\ G$. Evolutionary tracks are determined, which show that these stars are at a stage of deepening of the convective zones. The activity of the stars is explained in the terms of $\alpha - \omega$ dynamo.

Magnetic fields in several slowly rotating giants of spectral classes $G3.5 - K0$ are detected by Aurière et al. (2009 a). These stars have $v \sin i = 1.5 - 7.0\ km/s$, masses of $1.7 - 3.5\ M_{\odot}$ and measured longitudinal magnetic fields of the order of a few gauss.

Pollux is a slowly rotating, $v \sin i = 1.7\ km/s$, $K0$ giant and it has been known for some time to be weakly active (Strassmeier et al. 1990 a). A very weak longitudinal magnetic field, less than $1\ G$, is detected in Pollux by Aurière et al. (2009 b). The evolutionary track of the star is computed and it appears that Pollux is either at the base of the red giant branch or it is burning He in its core. Fitting the Li abundance with evolutionary models, the authors show that the progenitor of Pollux is a moderate rotator, which is either a normal A-type star or a magnetic Ap star. According to the authors, the magnetic activity of the star is more likely generated by a dynamo, which occurs naturally during the evolution of a normal A star, rather than being a result of the evolution of the large-scale fossil magnetic field of an Ap star.

Arcturus is a slowly rotating, $v \sin i = 1.5\ km/s$, $K1.5$ giant, which is

ascending the red giant branch. Its weak longitudinal magnetic field of about 0.5 G is detected by Sennhauser & Berdyugina (2011). The authors suggest that the origin of the magnetic field of Arcturus is most likely generated by a solar-like $\alpha - \omega$ dynamo, driven by convection and differential rotation.

The surface magnetic topology and sometimes its temporal evolution have been reconstructed using ZDI for a small number of cool giants – the Ap star descendants EK Eri (Aurière et al. 2011) and β Ceti (Tsvetkova et al. 2013), the fast rotating effectively single giant V390 Aur (Konstantinova-Antova et al. 2012). Giants, which are part of binary systems (for example RS CVn) and have ZDI maps, are mentioned earlier.

The first detection of magnetic field in M giant is reported by Konstantinova-Antova et al. (2009) for the $M6$ AGB giant EK Boo. The star has a mass of 1.9 $M_{\odot}$, $v \sin i = 11$ km/s and detected longitudinal magnetic field from -7 G to -3 G. The study of EK Boo is extended by Konstantinova-Antova et al. (2010), where the authors suggest that an $\alpha - \omega$ dynamo operates in that star.

Studies of magnetic activity in two samples of single G, K and M giants are presented by Konstantinova-Antova et al. (2013, 2014) and Aurière et al. (2014, in prep.).

The first sample presented by Konstantinova-Antova et al. (2013) and Aurière et al. (2014, in prep.) includes 50 single G and K giants and 9 M giants with different rotation and situated at different stages of evolution – red giant branch, He-burning phase, tip of the RGB. The main aim of the sudy is to understand the origin of the magnetic field and activity in giants – for the fast rotators it could be angular momentum dredge-up from the stellar interior that accelerates the stellar rotaion and causes an $\alpha - \omega$ dynamo operation, or triggering of magnetic dynamo and activity by planet engulfment, or remnant fast rotation from the main sequence, while for the slow rotators it could be a fossil field. Measured longitudinal magnetic fields for G and K giants are in the interval $0.25 - 100$ G, and for M giants ($M0 - M6$) in the interval from about -8 G to about 13 G. About the reasons for the magnetic activity, the authors give the following explanations:

- G and K giants with periods up to 200 days host $\alpha - \omega$ dynamo. These are intermediate mass stars and most of them are situated near the base of the RGB, experiencing the first dredge-up phase (Fig. 1.7).

- G and K giants with long rotational periods, but with strong magnetic field and activity, are descendants of Ap stars on the main sequence and possess fossil fields.

- All giants with periods less than 70 days are situated in the first dredge-up phase. This clumping does not support the planet engulfment hypothesis, because in a case of planet engulfment, the fast rotating active giants should be observed along the whole RGB. The authors support the hypothesis of the angular momentum dredge-up, which causes the fast rotation and dynamo operation in the stars with masses less than 4 $M_{\odot}$. For more massive stars fast rotation may be a remnant of the rotation they had on the main sequence.

- M giants from that study are situated at the tip of RGB and in the early AGB phase. At that phase stars experience the second dredge-up and additional angular momentum transition from the rapidly rotating core appears. This could result in an $\alpha - \omega$ dynamo action.

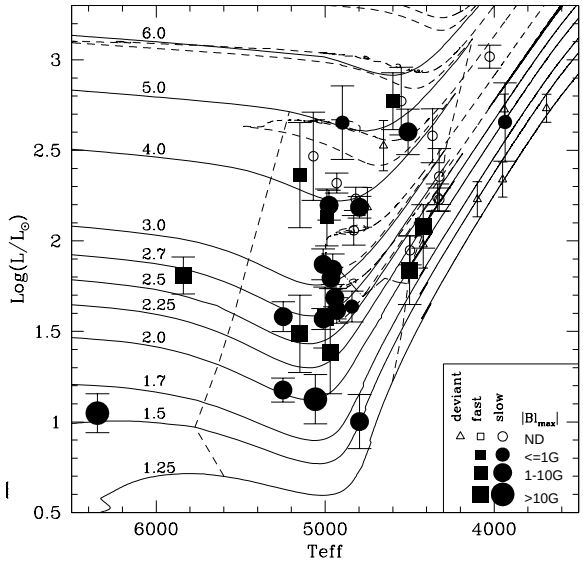

Figure 1.7: *HRD for G and K single giants (Konstantinova-Antova et al. 2013). Squares are for giants with fast rotation ($v \sin i > 8$ km/s). Open symbols are for non-detected stars. The two vertical dashed lines indicate the region of the first dredge-up.*

The second sample presented by Konstantinova-Antova et al. (2014) contains all single G, K and M giants up to $V = 4$ mag in the Solar vicinity (45 stars), selected independently of activity signatures, rotation, etc. These stars are situated at different evolutionary stages after the main sequence –

Hertzsprung gap, the region of the dredge-up phase and He-burning, stars ascending the RGB and AGB stars. This study is still ongoing and up to now 29 of 45 stars are observed and 15 of the observed stars are detected. The authors report about a tendency of clumping of stars at certain evolutionary phases:

- for less massive giants there are two clumping regions – (1) the region of the first dredge-up phase and He-burning; (2) the region near the upper RGB/early AGB.
- for the more massive giants the clumping region is AGB.

Except dynamo action and fossil fields, a third possible contributor to the surface magnetism of cool giants may be a high tangled magnetic pattern coming from a small-scale dynamo. While local dynamos are probably active in all stars with convective zones, their direct observational signatures may only be detectable in the most evolved objects (cool supergiants), for which the larger pressure scale height results in much larger convective cells (Schwarzschild 1975). This last type of magnetism is presumably responsible for the weak magnetic field detected at the surface of the slowly rotating supergiant Betelgeuse (Aurière et al. 2010, Petit et al. 2013).

1.2 *Structure and evolution of the Red Giants*

The life of a star as a red giant depends on its mass on the main sequence. They are divided in three groups mainly:

- low-mass stars – with masses $M \approx 0.8 \div 2\ M_{\odot}$; they develop a degenerate helium core after the main sequence and ignite helium in a so-called *helium flash*.
- intermediate-mass stars – with masses $M \approx 2 \div 8\ M_{\odot}$; they ignite helium stably in a non-degenerate core after the main sequence; after central He-burning phase they develope a degenerate carbon-oxygen core; at the end of their evolution they become CO white dwarfs.
- massive stars – with masses $M > 8\ M_{\odot}$; they ignite helium in a core after the main sequence; in a following stage of evolution they ignite carbon in a non-degenerate core and after that they ignite heavier elements in the core until a Fe core is formed.

Detailed descriptions of all evolutionary stages for stars with different masses could be found in Iben (1967 c, 1991). Our selected stars are of intermediate mass, so here we pay special attention to the evolution of such stars. As an example is taken an evolutionary track of a 5 $M_{\odot}$ star in the HRD in Fig. 1.8 (adapted from Iben 1967 c).

Stars are in thermal equilibrium while they are on the main sequence, the so called ***central hydrogen burning phase***. Hydrogen is converted into helium via the CN-cycle reactions near the center of a convective core. After the main sequence, one star has an inert helium core, which is hydrogen-exhausted. It is surrounded by a hydrogen-burning shell and a hydrogen-rich envelope. At that stage thermal equilibrium is no longer possible. Then, the helium core contracts and builds up a temperature gradient, which adds to the pressure gradient that is needed to balance gravity. The temperature gradient also causes an outward heat flow from the core.

Point B in Fig. 1.8 corresponds to the start of the overall contraction phase near the end of the main sequence. Point C corresponds to the exhaustion of hydrogen in the core and the disappearance of the convective core. It denotes the transition from hydrogen burning in the center to hydrogen burning in a shell.

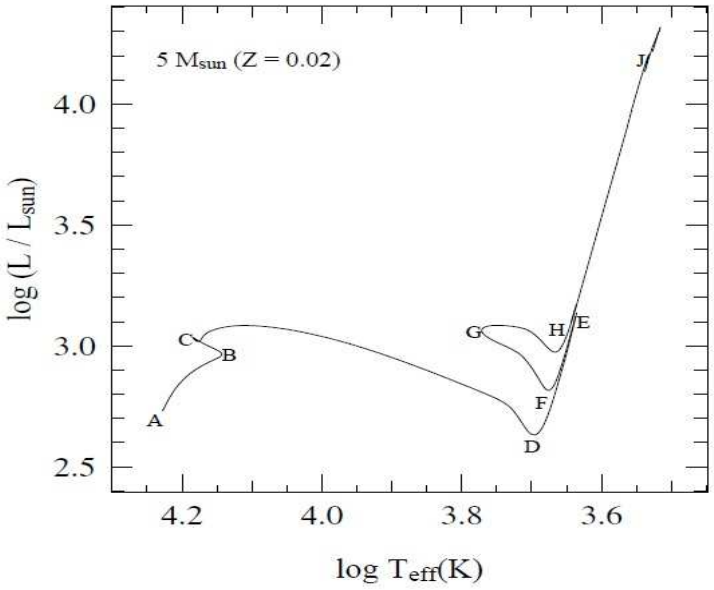

Figure 1.8: *The evolution track in the Hertzsprung-Russell Diagram of a 5 $M_{\odot}$ star (adapted from Iben 1967 c).*

The ***hydrogen-shell burning phase*** takes place after points C in Fig. 1.8. Between points $C-D$ a substantial fraction of the energy, generated by shell burning, is absorbed by the expanding envelope, which results in a decrease of the surface luminosity between these two points. Approaching point D, the temperature of the envelope decreases and the opacity increases. Shortly before point D, convection becomes the dominant mode of energy transport in a growing envelope, which extends inward from the surface.

Between points $D-E$ the star is a ***red giant*** with a deep convective envelope. That part of the evolution track is called ***Red Giant Branch*** *(RGB)*. Beyond the point D, the core continues its contractions, the temperature decreases, while the luminosity begins to increase.

Near the base of the RGB (point D) occurs an important process, called ***the first dredge-up*** (Iben 1964). Mainly, ***dredge-up*** is a convective mixing process, which leads to changes in the surface chemical composition. It occurs after the end of a dominant nuclear burning event, when the envelope deepens and cools, while the core contracts. It brings to the surface of a star material, which was processed by the nucleosynthesis. There are three dredge-up periods. The first dredge-up occurs when a star turns into a red giant. According to Sackmann & Boothroyd (1999), the convective envelope reaches its deepest penetration during the first dredge-up. The second dredge-up refers to the time, when the star turns from a core He-burning star into an asymptotic giant branch (AGB) star. The third dredge-up refers to the thermal pulses on the AGB.

During the entire ***H-shell burning phase*** $C-E$ the helium core remains non-degenerate. At point E the temperature (approaching 10^8 K) and the density in the helium core have become high enough that the 3α-reaction starts to produce energy, the core stops to contract. Immediately after the triple-alpha ignition at point E, the luminosity of the star drops. Helium ignition marks the end of the red giant phase.

The ***helium burning phase*** $E-H$ starts and the star describes the so called ***blue loop***. The extension of the loops in the HRD increases with increasing the mass of the stars. The core is non-degenerate, so the nuclear burning is thermally stable. Between points E and G, the stellar envelope contracts and the temperature increases. The major source of nuclear-energy production is still the hydrogen burning shell, which contributes about 85 % of the star's energy output. But the rate of energy production in the core increases relative to the rate of energy production in the hydrogen burning shell. Beyond point G, the core begins to contract. When He is exhausted in the core, the star enters the ***He-shell burning state*** and approaches the RGB asymptotically. Helium-core burning leaves a C/O core, which is surrounded by both a He- and a H-burning shells.

After point H, the luminosity begins to rise. These stars are called ***asymptotic giant branch (AGB) stars***. The convective envelope extends deeper into the star.

1.3 *Lithium and $^{12}C/^{13}C$ ratio as tracers of the evolutionary processes*

Lithium abundance and $^{12}C/^{13}C$ ratio are key tracers of the evolutionary processes of stars and provide an important check on the extent of convective mixing in stars.

Lithium is destroyed at temperatures around $2 \times 10^6\ K$. Because of that, it is expected to be destroyed in all but the top 2-3 %, approximately, by mass of a main sequence star (Iben 1967 c).

A red giant is theoretically expected to have a lithium abundance of $log\ \epsilon(Li) < 1.5$ (Iben 1967 a, b). This value is based on the mass fraction, in which lithium is expected to survive in a main sequence star and from the assumption that the star left the main sequence with its initial surface lithium abundance of $log\ \epsilon(Li) = 3.0 - 3.2$. Then, the star leaves the main sequence and evolves as a red giant. Its convective envelope is too cool to cause destruction of lithium. The envelope expands inward – it brings up processed material from the interior to the surface, but in the same time it transports Li and other light elements from the surface to the interior, where they are destroyed. Thus, the convective mixing causes the surface abundances of Li and other light elements to decrease (Iben 1967 a, b, Gilroy 1989).

After the second dredge-up, the abundance of Li again decreases.

Another tracer of the mixing events during the evolution along the RGB is the carbon isotopic ratio $^{12}C/^{13}C$. The CN-cycle is responsible for the conversion of ^{12}C into ^{13}C and ^{14}N by the reactions $^{12}C(p,\gamma)^{13}N(\beta^+,\nu)^{13}C(p,\gamma)^{14}N$. As the convective envelope deepens, the mixing begins to carry ^{14}N outward and ^{12}C inward, so the abundances of ^{13}C and ^{14}N in the envelope gradually increases, while the abundance of ^{12}C drops (Iben 1967 c).

A decrease of the carbon isotopic ratio from about 90, the solar value, to about 20-25, is expected due to the first dredge-up (Dearborn et al. 1976). But peculiar abundances have been observed in open clusters (Gilroy 1989, Gilroy & Brown 1991, Tautvaišiene et al. 2000, 2005), globular clusters (Pilachowski et al. 2003) and field stars (Gratton et al. 2000) with ratios down to 3-4, the CN cycle equilibrium value.

In standard evolutionary models (non-rotating, non-magnetic stars), con-

vection is the only mechanism that drives mixing in stellar interiors. But these low values of the carbon ratio indicate a non-standard mixing. The extra-mixing might be related to meridional circulation and turbulence induced by rotation (Charbonnel 1994, 1995). In later papers, Charbonnel & Zahn (2007), Charbonnel & Lagarde (2010), Charbonnel et al. (2012), discuss in details the effects of the rotation-induced mixing and the thermohaline instability. The rotation-induced mixing modifies the internal chemical structure of main sequence stars, but its signatures are revealed only later in the evolution, when the first dredge-up occurs. On the other hand, the thermohaline mixing is expected to set in after the first dredge-up, when the star reaches the central helium burning phase, and it is induced by the inversion of molecular weight by the $^3He(^3He, 2p)^4He$ reaction.

1.4 *Evolutionary hypotheses for the magnetic activity*

Two main mechanisms have been proposed to explain the presence of magnetic fields in single giants. The first one is the fossil field hypothesis. According to it, since the interstellar medium is permeated by magnetic fields, when the clouds contract to form stars, they trap and amplify the primordial interstellar field. The second hypothesis is existence of a stellar dynamo, which generates the magnetic fields.

1.4.1 *Dynamo action*

Dynamo models are based on mean field dynamo theory and the α- and ω-effects (Moffatt 1978, reviews by Ossendrijver 2003 b, Charbonneau 2010 and references therein). The basic equation, which shows the dynamical evolution of the magnetic field, is the magnetohydrodynamic (MHD) induction equation:

$$\frac{\partial B}{\partial t} = \nabla \times (V \times B) - \nabla \times (\eta \nabla \times B) \tag{1.4.1}$$

where $\eta = c^2/4\pi\sigma$ is the magnetic diffusivity. This equation, Eq. 1.4.1, describes the temporal variation of the magnetic field by two terms – a source term, which depends on the velocity field V, and a dissipation term. The source term shows that the dynamo effect comes from the conversion of kinetic energy into magnetic energy.

The mean field theory is an approach, which consists in splitting the magnetic and velocity fields into large (L) and small (l) parts:

$$B = \langle B \rangle + b' \tag{1.4.2}$$

$$V = \langle V \rangle + v' \tag{1.4.3}$$

Applying the mean field approach, the modified induction equation is:

$$\frac{\partial \langle B \rangle}{\partial t} = \nabla \times (\langle V \rangle \times \langle B \rangle + \langle v' \times b' \rangle - \eta \nabla \times \langle B \rangle) \tag{1.4.4}$$

Next step is to use a Taylor expansion for $\langle v' \times b' \rangle$ around the mean field $\langle B \rangle$, the so called first order smoothing approximation (FOSA)(Moffatt 1978, Ossendrijver 2003 b). Then, the mean field induction equation is:

$$\frac{\partial \langle B \rangle}{\partial t} = \nabla \times (\langle V \rangle \times \langle B \rangle + \alpha \langle B \rangle - (\eta + \beta) \nabla \times \langle B \rangle) \tag{1.4.5}$$

The first term in the above equation describes the transport and stretching of the field $\langle B \rangle$ by the large-scale motions (meridional circulation and differential rotation), the second term represents the α-effect (Coriolis force, turbulent convection, MHD instability) and the latter term is the Ohmic diffusion. When there is a regeneration of the two components of the magnetic field (***poloidal*** along meridians on a sphere and ***toroidal*** along parallels on a sphere) and they are maintained against Ohmic dissipation, there is a dynamo action. Within the classical mean field dynamo framework (Moffat 1978), two effects are invoked to explain the transformation between the two magnetic field components – these are the α- and ω- effects (Fig. 1.9). The relative amplitude between the ω- and α- effect is what enables to classify the dynamo into different types – dynamos are either of the $\alpha - \omega$, α^2 or $\alpha^2 - \omega$ type.

The $\alpha - \omega$ dynamo operates as follows (Fig. 1.9): the ω-effect generates a toroidal field from a poloidal field by the radial differential rotation inside the tachocline. Then the α-effect converts a poloidal field from a toroidal field (but also a toroidal field from a poloidal field) at the base of the convective zone, but above the tachocline. The tachocline (Parker 1993) is a rotational shear layer, uncovered by helioseismology, which is beneath the Sun's convective envelope, providing smooth transition between the latitudinal differential rotation of the envelope and the rigidly rotating radiative core. If the two processes (α- and ω-effects) occur at the same location, it

is expected to have a "catastrophic α-quenching" (Ossendrijver 2003 a, b), i.e. a strong decrease of the α effect in the presence of a strong field, that would prevent any further dynamo action. That's why the toroidal field takes place in the tachocline and the poloidal field is in the convective envelope and in this way the α effect is not taking place where the magnetic field is stored. But the way the field is transported from and to the tachocline is not completely clear.

It seems that the hybrid models, which include all sources of poloidal field, are those that give the most conclusive results – differential rotation, a tachocline, meridional circulation, Babcock-Leighton flux transport model (Babcock 1961, Leighton 1969, Dikpati et al. 2004)), etc.

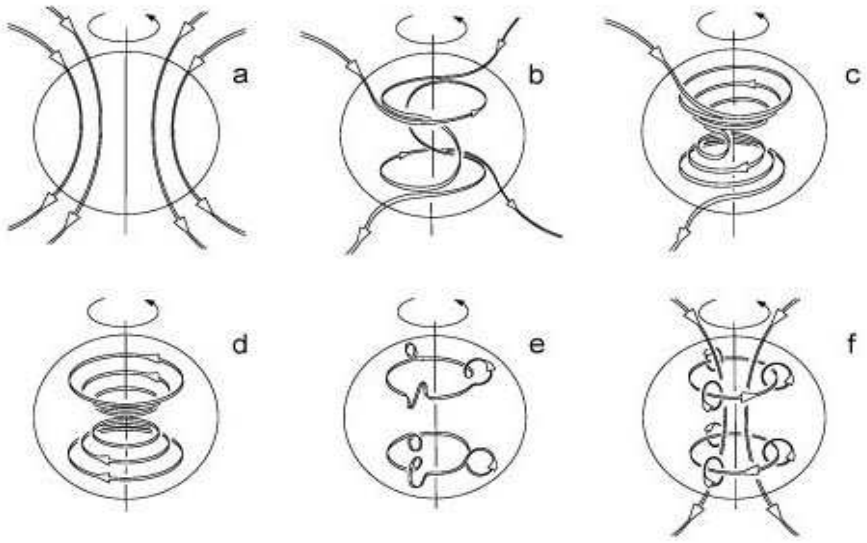

Figure 1.9: *A, b, c – ω-effect generates a toroidal field from a poloidal field. D, e, f – α-effect generates a poloidal field from a toroidal field. Image credit by Love (1999).*

In fast rotating single late-type giants a dynamo could be triggered by angular momentum dredge-up from the stellar interiors or by a planet engulfment. These are giants, which have above $v \sin i = 8\ km/s$ (i.e. about 3 times the average value of $v \sin i$ for G and K giants, de Medeiros et al. 1996 a, b), and are just a few percent of the G and K giants.

Their fast rotation was tried to be explained by the dredge-up of angular momentum from a rapidly rotating stellar core by Simon & Drake (1989). When the stars are in the dredge-up phase, their convective en-

velopes deepen towards the core. In this way, amount of angular momentum would be dredge-up and it would accelerate the stellar rotation and would cause an $\alpha - \omega$ dynamo to operate. Recently, Mosser et al. (2012) showed that indeed an angular momentum transfer occurs from the core to the envelope for red giants, using Kepler asteroseismic data.

The second scenario, which tries to explain the fast rotation and subsequently the dynamo operation, is a planet engulfment. A model of that is proposed by Siess & Livio (1999). According to their model, as the planet spirals in, it will deposit angular momentum in the envelope and finally dissipate close to the core. The deposition of angular momentum can produce a strong differential rotation at the base of the convective envelope. The differential rotation and convection together can generate an $\alpha-\omega$ dynamo. Their model indicates, that only massive planets or brown dwarfs with $M > 5\ M_{Jup}$ can spin-up the giant envelope to a significant fraction of the Keplerian velocity.

But recent studies of single G and K giants (Konstantinova-Antova et al. 2013, 2014, Aurière et al. 2014 in prep.) show the existence of two "magnetic strips" on the HRD, which is not in support of this second scenario for planet engulfment.

These are the two scenarios for the fast rotating giants, e.i. those for which classical models cannot explain the fast rotation. Other giants can have dynamo-driven magnetic fields, as is shown by Konstantinova-Antova et al. (2013, 2014), Aurière et al. (2014 in prep.).

1.4.2 *Ap stars and fossil fields*

"Chemically peculiar magnetic stars" or *"Ap/Bp stars"* (hereafter *Ap* stars) appear similar to normal A and late B main sequence stars, but:

- have peculiar chemical abundance – show spectral lines of abnormal strength or weakness of various elements compared to the lines of typical A and late B stars
- have $v \sin i$ values that are usually less than about 80 km/s compared to values of $200 - 300$ km/s, which are usually found in A and B stars
- have observable magnetic fields

The first *Ap*-type star, which hosts a stellar magnetic field, 78 Vir, was detected by Babcock (1947). Nowadays, Ap/Bp stars are about 5–10 % of the A and B type main sequence stars (Wolff 1968, Moss 2001, Power et al. 2008). It is assumed that the magnetism in these stars is due to *"fossil fields"*. Fossil field hypothesis suggests that the stellar magnetic fields are relics from

the field present in the parental interstellar cloud. It is expected that fossil fields will evolve quite slowly with a time-scale for significant changes of many millenia or more. In these stars, the magnetic field cannot simply decay away through Ohmic dissipation. This long lifetime is a direct result of Maxwell's equations and the very high electrical conductivity of the ionized gas inside a star. The characteristic decay time t_c is of the order of $10^{10}\ yr$, so that the characteristic time for field variation in a main sequence star is considerably longer than the main sequence lifetime (Donati & Landstreet 2009). Such fields are expected to be relatively simple in structure and have simple large-scale topologies. More on general properties of magnetic Ap/Bp stars can be found in Landstreet (1992).

Some authors even suggest that the magnetic field of a main sequence star can survive and show up in magnetic white dwarfs (Angel et al. 1981).

Ap stars generally spin much more slowly than non-peculiar stars of similar masses. Magnetic braking during pre-main sequence evolution phase is assumed to be responsible for the slow rotation of these stars. That question is studied by Stepień (2000), where he varies four parameters (accretion rate, mass loss rate via a wind, the strength of the stellar magnetic field and the lifetime of the disk), in order to see their influence over the lost of angular momentum, which would make the stars to spin down.

An interpretation of Ap/Bp magnetic stars is given by the *"oblique rotator model"*. According to that model, the star is a magnetic dipole, whose magnetic axis is inclined at some angle β to the rotation axis and angle ι to the line of sight (Stibbs 1950, Preston 1967). The dipole strength is greater than about 300 G (Aurière et al. 2007). When an *Ap* star evolves, its fossil field dipole strength weakens with $1/R^2$ (magnetic flux conservation) and interacts with convection, which is the origin of the observed activity.

First published observations of *Ap* stars in both circular and linear polarization, were made by Wade et al. (2000 a, b). Usually, the variations with time of the longitudinal magnetic field B_l are sinusoidal and there is a sign reversal (Aurière et al. 2007, Wade et al. 2000 a, b, Kochukhov & Wade 2010, Silvester et al. 2012).

A star, which is suspected to evolve from an *Ap* star on the main sequence, is 14 Ceti (Aurière et al. 2012). The star has $v \sin i < 4\ km/s$. The longitudinal magnetic field B_l is measured to varry from about $-8\ G$ to about $-30\ G$. The position of the star in the HRD is entering the Hertzsprung gap. The dipole strength of the *Ap* star progenitor is calculated, which is greater than about 370 G (the minimum dipole strength is about 300 G, Aurière et al. 2007). The conclusion of the authors is that the magnetic field of 14 Ceti is of fossil origin.

Two more stars, suspected to possess fossil fields, are β Ceti (Tsvetkova et al. 2013) and EK Eri (Stepień 1993, Aurière et al. 2011), which are discussed in Chapter 3 of the present thesis (Sec. 3.1 and Sec. 3.2, respectively).

1.5 *Aims of the study*

This work is based on the expanded studies of three stars – two of them are the slowly rotating $K0$ giant β Ceti with $v \sin i = 3.5\ km/s$ and the $G8$ giant EK Eri with $v \sin i = 0.5\ km/s$, and the third star is the fast rotating $G8$ giant V390 Aur with $v \sin i = 29\ km/s$. These stars are selected, because of earlier reported evidences for their magnetic activity. They have similar masses (3.5 $M_{\odot}$ for β Ceti, 1.9 $M_{\odot}$ for EK Eri and $1.8 - 2\ M_{\odot}$ for V390 Aur), but they are at different stages of evolution – V390 Aur is evolving along the base of the red giant branch, EK Eri is located at the end of the Hertzsprung gap and the begining of the first dredge-up phase, while β Ceti is already in the central helium-burning phase. Taking into account these important parameters, $v \sin i$, mass and the position of the HRD, we could stuty the properties of the magnetic fields and activity and to test the different hypotheses about their origin in single late-type giants (fossil fields or dynamo action) and their evolution along the giant phase.

Observational data for these three stars are obtained with two twin fiber-fed échelle spectropolarimeters – *Narval* and *ESPaDOnS*. The least square deconvolution (LSD) method is applied for extracting high signal-to-noise ratio line profiles, from which the surface-averaged longitudinal magnetic field B_l is measured. Line activity indicators CaII K&H, $H\alpha$, CaII IRT and radial velocity are also measured. The Zeeman Doppler imaging (ZDI) inversion technique is employed for reconstructing the large-scale magnetic field. Their chemical abundances and evolutionary tracks on the HRD are modeled.

Chapter 2

Measuring Stellar Magnetic Fields

Mechanisms, which have been used for direct detection of stellar magnetic fields are the Zeeman effect (Zeeman 1897) and the Hanle effect (only in solar magnetic field measurements; Hanle 1924). Indirect proxies for stellar magnetic activity are: photometric variability (due to the passage of surface temperature spots on the visible hemisphere due to stellar rotation); rotational modulation of photospheric spectral lines (induced again by spots traveling onto the stellar disk); emission in spectral lines (due to the presence of hot plasma in the chromosphere and corona); radio emission (due to synchrotron electrons spiraling about the large-scale magnetic loops); UV and X-ray emission. There are also other diagnostic techniques for studying stellar activity like broad band polarization, molecular bands modeling, line depth ratios (based on the analysis of depth ratios of a pair of lines – one insensitive and one very sensitive to temperetaure), astroseismology. But all these techniques are not the scope of this thesis and more information could be found in the reviews of Reiners (2012) and Berdyugina (2005).

Indicators, which are used in this study, are Stokes V signatures and the longitudinal magnetic field B_l, the chromospheric lines $H\alpha$, CaII K&H, CaII infrared triplet, radial velocity and S-index measurements.

2.1 *Polarized light, Zeeman effect and Stokes parameters*

The light wave is an electromagnetic wave, which has both an electric and a magnetic component. They are perpendicular to each other and in the same

time they are perpendicular to the direction of propagation (Fig. 2.1). The electric and magnetic charges vibrate in a variety of directions. When all the vibration directions are equally present in a beam, the configuration is symmetrical with respect to the propagation direction, and this is refered to as *unpolarized light*.

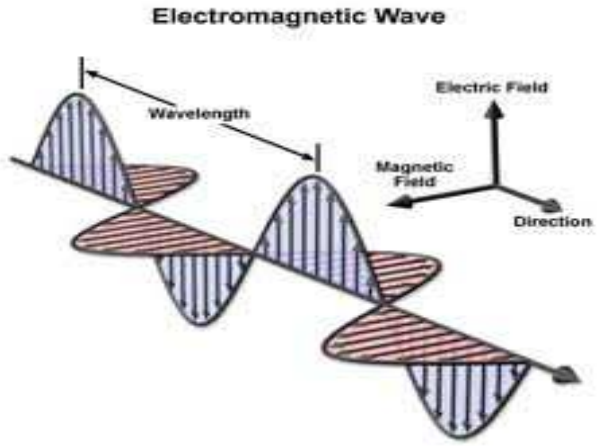

Figure 2.1: *Schematic view of an electromagnetic wave with an electric and a magnetic component.*

Unpolarized light could be transformed into a polarized light using a polarizer. It transmits these vibrations, which are parallel to a certain axis. Polarization could be *linear*, *circular* or *elliptical*.

Linear polarization – vibrations of the light wave occur in a single plane, which should contains the direction of propagation and it is called the *plane of polarization* (electric and magnetic components have the same amplitude and are in phase). There are two parameters, which describe the linear polarization of a light beam – the degree of linear polarization P and the angle θ, which is the angle between the measuring direction and the direction of the maximum flux of the light beam. The degree of linear polarization could be calculated by the equation:

$$P = \frac{I_{max} - I_{min}}{I_{max} + I_{min}} \tag{2.1.1}$$

where I_{max} is the maximum light flux for some orientation of the polarizer and I_{min} is the minimum flux for the perpendicular orientation of the polarizer. For unpolarized light $P = 0$, because $I_{max} = I_{min}$, which means that the flux remains constant in each one orientation of the polarizer. For

totally polarized light $P = 1$, because $I_{min} = 0$. In every other situation P is a fraction smaller that 1 and the light beam is partially polarized.

Circular polarization – within a beam of circularly polarized light, the tip of the electric field vector describes an helix (Fig. 2.2) (electric and magnetic components have exactly the same amplitude and are exactly 90° out of phase). When the rotation is oriented clockwise, the polarization is said to be *right-handed* and when the rotation is counter-clockwise, the polarization is *left-handed*.

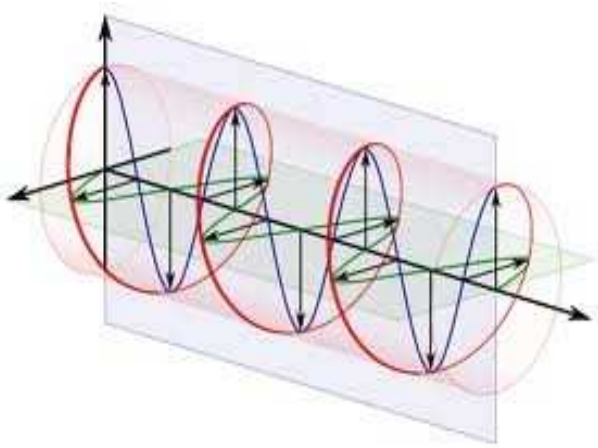

Figure 2.2: *Circular polarization.*

Elliptical polarization – the tip of the electric field vector describes an ellipse. It is a sum of linearly and circularly polarized light (electric and magnetic components do not have the same amplitude and either are not in phase; their amplitude ratio and phase offset are constant in time). Like the circular polarization, elliptical polarization could be *right-handed* and *left-handed*.

The Zeeman effect

The splitting of a spectral line into two or more components when the atom is placed in a magnetic field, is called *the Zeeman effect*. This effect was first observed in 1896 by the Dutch physicist Pieter Zeeman as a broadening of the D-lines of sodium.

A spectral line is emitted when electrons make a transition from one discrete energy level to another. Each electron has its own spin s_i and orbital angular momentum l_i. Electron spins interact among themselves and form a *total spin angular momentum* $\boldsymbol{S}$. In the same manner is forming a *total orbital*

angular momentum $\boldsymbol{L}$. The interaction between the quantum numbers L and S is called *LS-coupling* or *spin-orbit coupling* (Fig. 2.3). This coupling forms a *total angular momentum* J:

$$\overrightarrow{J} = \overrightarrow{L} + \overrightarrow{S} \tag{2.1.2}$$

where

$$\overrightarrow{L} = \sum_{i=1}^{N} l_i \qquad \overrightarrow{S} = \sum_{i=1}^{N} s_i \tag{2.1.3}$$

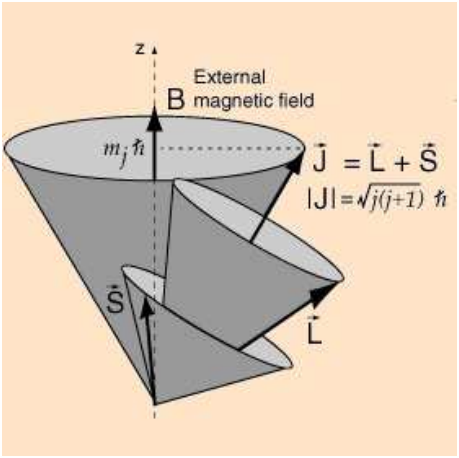

Figure 2.3: *LS-coupling.*

In the presence of a magnetic field, each energy level with total angular momentum quantum number J splits into $(2J+1)$ equally spaced sublevels with different magnetic quantum numbers m_j. In this situation, sublevels with different m_j possess different energy. The difference between subsequent states of energy is proportional to Bg_J, where B is the magnetic field and g_J is the *Landé factor*. This Landé factor is a function of the electron spin g-factor g_S and the electron orbital g-factor g_L:

$$g_J = g_L \frac{J(J+1) - S(S+1) + L(L+1)}{2J(J+1)} + g_S \frac{J(J+1) + S(S+1) - L(L+1)}{2J(J+1)} \tag{2.1.4}$$

The orbital g-factor is $g_L = 1$ and the spin g-factor is $g_S = 2$. Then

$$g_J = \frac{3}{2} + \frac{S(S+1) - L(L+1)}{2J(J+1)} \tag{2.1.5}$$

The transition between two energy levels must follow the selection rule $\Delta m_j = -1, 0, 1$. Spectral lines with $\Delta m_j = 0$ are called π *components*, spectral lines with $\Delta m_j = -1$ are called σ_{blue} *components* and spectral lines with $\Delta m_j = +1$ are called σ_{red} *components*. Usually, two energy levels have different spin and orbital angular momentum quantum numbers, which means that their Landé factors are different. Then, it is used the *effective Landé factor* $\overline{g}$, which is the average displacement of the group of σ components with respect to the line center. Then, the value of $\overline{g}$ is a function of the angular momenta J_1 and J_2 and the Landé factors g_1 and g_2 of the two levels (Beckers 1969):

$$\overline{g} = \frac{1}{2}(g_1 + g_2) + \frac{1}{4}(g_1 - g_2)[J_1(J_1 + 1) - J_2(J_2 + 2)] \tag{2.1.6}$$

The wavelength shift of the σ components in mÅ is $\Delta\lambda$:

$$\Delta\lambda_{\sigma-\pi} = 4.67\overline{g}\lambda_0^2 B \tag{2.1.7}$$

where λ_0 in $\mu\ m$ is the initial wavelength, and B in kG is the magnetic field.

The splitting of the three Zeeman components σ_{blue}, σ_{red} and π is shown in Fig. 2.4. Each component has different magnetic moment and in this way it has different polarization state (Fig. 2.5). The π component is not shifted in energy, while the σ components are shifted according to the formula above. When the magnetic field is perpendicular to the line-of-sight (*transverse field*), the three components exist and they are all linearly polarized, but the polarization of σ components is in perpendicular direction according to the polarization of the π component. When the magnetic field is parallel to the line-of-sight (*longitudinal field*), the π component is not observable and the σ components have opposite circular polarizations. When the magnetic field forms an angle α with the line-of-sight, the intensities of the components are proportional to $(1 + \cos^2\alpha)/2$, $\sin^2\alpha$, $(1 + \cos^2\alpha)/2$ and the π component is linearly polarized, while the σ components are elliptically polarized.

The following information about the magnetic field could be found through the Zeeman effect: *a)* the distance between the components is proportional to the field modulus (if the field strength does not exceed several tens of kiloGauss); *b)* the intensities of the components depend on the angle α between the magnetic vector and the line-of-sight; *c)* the linear polarization at the line center is parallel to the direction of the projected vector field. These 3 points should be sufficient to determine the 3 components of the magnetic

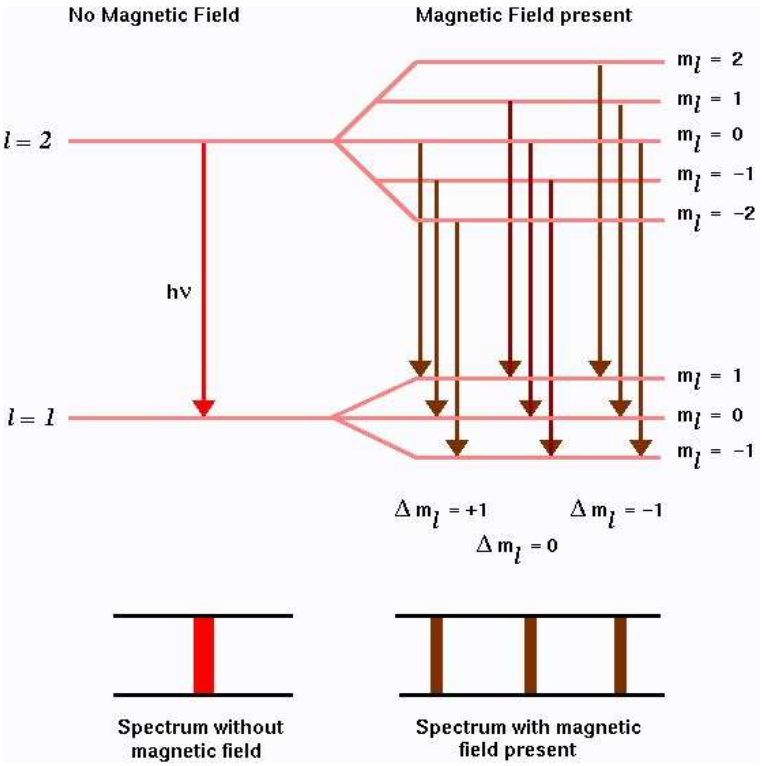

Figure 2.4: *The splitting of the three Zeeman components* σ_{blue} *(*$\Delta m_l = -1$*),* σ_{red} *(*$\Delta m_l = +1$*) and* π *(*$\Delta m_l = 0$*).*

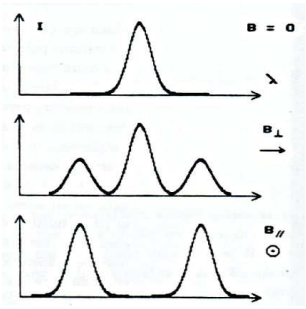

Figure 2.5: *The three Zeeman components depend on the orientation of magnetic field relative to the line-of-sight. Image credit by Leroy (2000), "Polarization of light and astronomical observation".*

vector – B_x, B_y and B_z (the last one being along the line-of-sight) (Leroy 2000).

The state of polarization could be defined by the ***Stokes vector***, which

consists of 4 parameters I, Q, U and V, called *Stokes parameters* (Stokes 1852, Leroy 2000), and illustrated in Fig. 2.6:

- intensity $\boldsymbol{I}$ – the unpolarized light
- the degree of polarization $\boldsymbol{Q} = I_{0^\circ} - I_{90^\circ}$ – differences in intensities between horizontal and vertical linearly polarized beams;
- the plane of polarization $\boldsymbol{U} = I_{45^\circ} - I_{135^\circ}$ – differences in intensities between linearly polarized beams oriented at 45° and 135°;
- the ellipticity $\boldsymbol{V} = I_{right} - I_{left}$ – differences in intensities between right and left circular polarized beams.

It is obvious that for a totally polarized beam $I^2 = Q^2 + U^2 + V^2$. The polarization degree of a beam is defined as the ratio:

$$p = \frac{\sqrt{Q^2 + U^2 + V^2}}{I} \tag{2.1.8}$$

When the polarization is pure circular, then $Q = U = 0$ and the degree of circular polarization is $p = V/I$. When the polarization is pure linear, then $V = 0$ and $p = \sqrt{Q^2 + U^2}/I$.

The four Stokes parameters I, Q, U and V are determined by the atmosphere's thermal and magnetic structure.

The circular polarization is about an order of magnitude stronger than the linear polarization in the case of Zeeman effect (Leroy 2000). Since the giants possess small magnetic fields, the polarization signatures are very small. That's why it is possible to measure only Stokes V in this work.

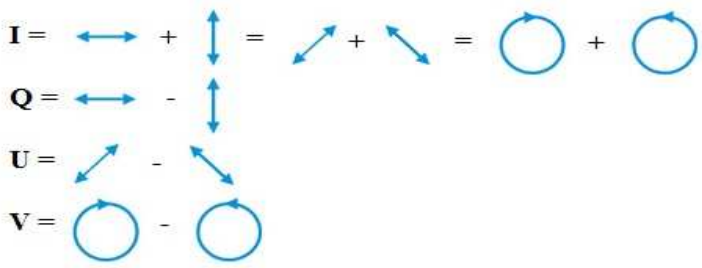

Figure 2.6: *Definition of Stokes parameters.*

2.2 *Instruments – Narval and ESPaDOnS*

Narval and *ESPaDOnS* (Échelle SpectroPolarimetric Device for the Observation of Stars) are twin fiber-fed échelle spectropolarimeters. *Narval* (Aurière 2003) operates at the 2-m Télescope Bernard Lyot (TBL) at Pic du Midi Observatory, France. *ESPaDOnS* (Donati et al. 2006 a) operates at the 3.6-m Canada-France-Hawaii Telescope ($CFHT$) of Mauna Kea Observatory, Hawaii. More technical details could be found at the following webpages – *Narval* (http://www.ast.obs-mip.fr/projets/narval/v1/) and *ESPaDOnS* (http://www.ast.obs-mip.fr/projets/espadons/espadons.html).

In polarimetric mode, both spectropolarimeters have a spectral resolution of about 65 000 and a spectrum coverage from the near-ultraviolet at about 370 nm to the near-infrared domain at about 1050 nm in a single exposure. They consist of a Cassegrain module (including a polarimeter, a calibration module and guiding tools), a fiber link and a spectrograph. Additional information about the technical description of these spectropolarimeters could be found also in Petit et al. (2003), Donati (2003) and Silvester et al. (2012).

Different configurations are available for *Narval* and *ESPaDOnS* – a spectropolarimetric mode (with spectral resolution of about 65 000, recording intensity and polarization spectra of the star) and a spectroscopic mode (with spectral resolution of about 80 000, only intensity spectrum from the star is recorded.)

The polarimeter

The polarimetric module (Fig. 2.7) is located on the Cassegrain bonnette of the reflector and in this way the instrumental polarization and the oblique reflection before the polarization analysis are reduced. The polarimetric analysis is performed through a combination of one Wollaston prism and three Fresnel rhombs (Semel et al. 1993). There is one fixed quarter-wave rhomb located between the two half-wave rhombs, all of them coated with MgF_2 to make them almost perfectly achromatic throughout the whole wavelength domain. These two half-wave rhombs rotate about the optical axis with respect to the fixed quarter-wave rhomb and the Wollaston prism in order to achieve a circular or linear polarization analysis of the stellar light.

In polarimetric mode, the configuration consists of these three Fresnel rhombs and the Wollaston prism. The two beams, produced by the Wollaston prism, are imaged onto the two fibers of the fiber link, called *object fibers*.

The Wollaston prism separates the stellar light into two beams, which are polarized along and perpendicular to the instrumental reference azimuth. Stokes V spectra are produced from a sequence of 4 sub-exposures. For each

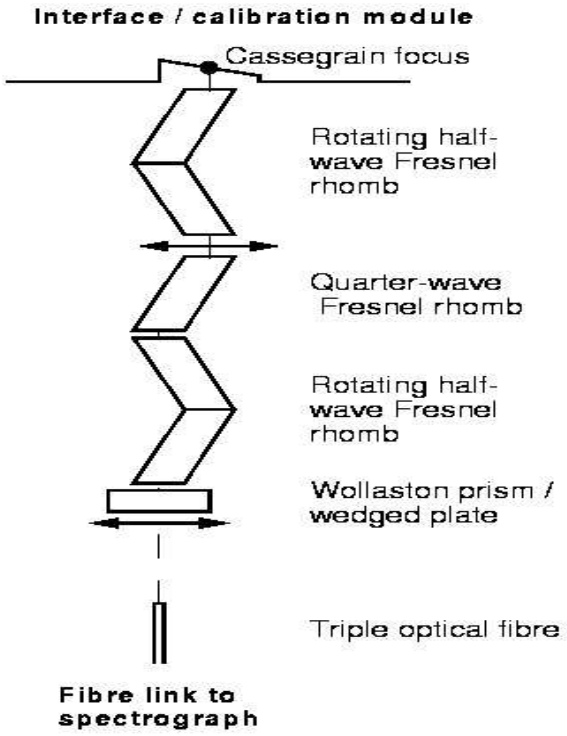

Figure 2.7: *The polarimeter configuration.*

of these sub-exposures the half-wave rhombs are rotated to different angles. Additionally, a diagnostic *Null* spectrum is obtained in other to cancel out the real polarization. The N spectrum tests the system for spurious polarization signals (Semel et al. 1993, Donati et al. 1997, Wade et al. 2000 a).

The interface/calibration module

The interface module is located before the polarimeter entrance (Fig. 2.7). It provides guiding and calibration facilities. There is a field viewing CCD camera for a guiding. For that purpose the camera collects photons, which are redirected from the Cassegrain focus.

When the calibration mode is used, another removable prism is inserted on the optical axis. Its role is to redirect the beam from the calibration lamps to the mirror atop the polarimeter. On the calibration wheel there are calibration lamps, polarizers, diffusers, providing various sorts of calibration light. The wheel is remote controlled. There are two lamps for a wavelength calibration (Th/Ar lamp and Ne lamp) and one lamp for a flat-field calibration (Halogen lamp). The Fabry-Perot filter is inserted in the beam just above the Wollaston prism to produce interference patterns in stellar or

calibration spectra, which is used to check the instruments stability.

This module also includes an atmospheric dispersion corrector, made of 2 separate null-deviation prisms rotating independantly from each other and cancelling out in real time the atmospheric refraction.

The fiber link

The link contains three optical fibres, which are used to transport the stellar light to the échelle spectrograph through a Bowen-Walrawen type image slicer (Fig. 2.8). Only two fibers are used simultaneously – the two object fibers in polarimetric mode; one object fiber and the sky fiber in non-polarimetric mode.

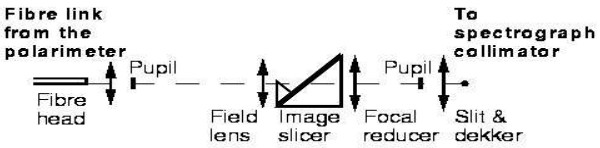

Figure 2.8: *The image slicer position.*

The spectrograph

It is a prism cross-dispersed échelle spectrograph working in dual pupil and quasi Littrow configurations, and including a fully-dioptric camera. The pupil size is about 200 *mm*. A Hartmann mask is located at the entrance of the camera for precise focus adjusting. The whole optical spectrum is divided out in 40 orders and projected on a CCD detector.

The path of the light is shown in Fig. 2.9 – light comes from the image slicer, enters the spectrograph, where it goes to the main collimator, then to the diffraction grating, then back to the main collimator, then to the flat mirror, the transfer collimator, the double prism cross-disperser, the fully-dioptric camera and finally to the CCD detector.

The spectrograph is surrounded by a twin layer enclosure in order to ensure an optimal thermal stability throughout the nights.

All motions of the optical components are remote controlled.

Reduced spectra were extracted using the automatic reduction software LibreEsprit, developed for *Narval* and *ESPaDOnS*. A detailed description of the algorithm implemented in this software can be found in Donati et al. (1997) and also at the following web-page http://www.cfht.hawaii.edu/Instruments/Spectroscopy/Espadons/Espadons_esprit.html.

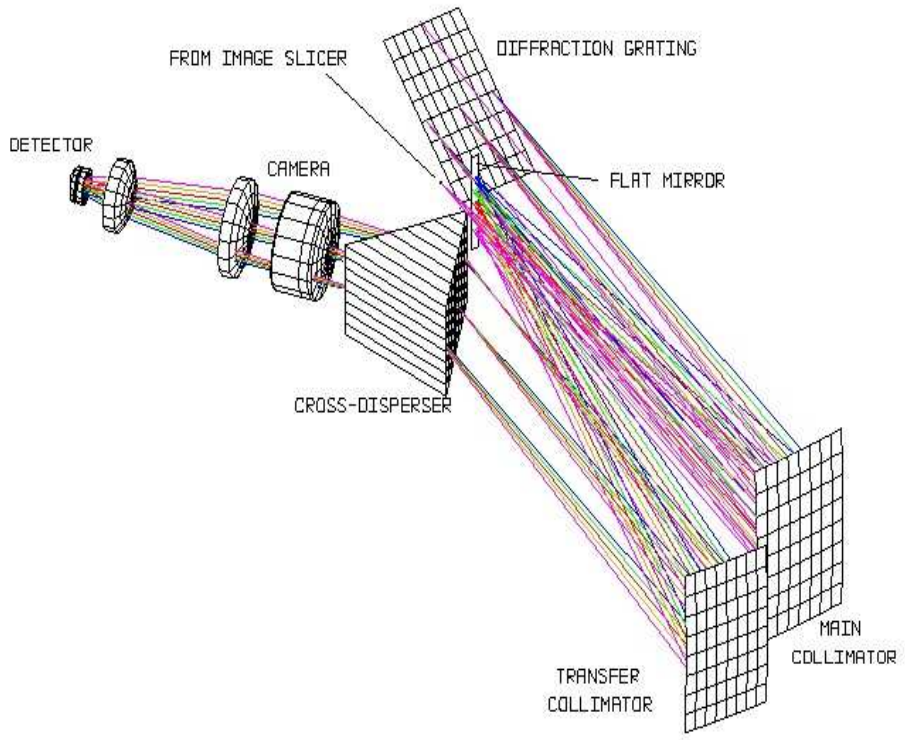

Figure 2.9: *The spectrograph.*

2.3 *Least Squares Deconvolution (LSD) technique*

Least Squares Deconvolution (LSD) technique enables averaging from several hundred to tens of thousand spectral lines from a complete échelle spectrum in order to derive *"mean"* Stokes I, Q, U and V line profiles. It assumes that the spectral lines repeat the same information and thus they have the same Zeeman signatures, i.e. spots affect all spectral lines in a similar way. Using that technique, it is possible to reconstruct an average line shape, *the LSD profile*, with high signal-to-noise ratio (S/N).

One spectrum could be written as a convolution of a *"mean profile"* with a line pattern – a sum of Dirac functions, whose position and amplitude correspond to the wavelength and weight of each selected spectral line. A detailed description of the method could be found in Donati et al. (1997) and Wade at al. (2000 a).

The Zeeman signatures are very small. The relative noise levels in Stokes V profiles should be lower than 10^{-4}. Such low noise levels can not be ob-

tained from a single line in a single spectrum. In the weak-field approximation (for field strengths smaller than 1 kG), each Stokes V local line profile is:

$$V_{loc}(v) \propto g\lambda \frac{\partial I_{loc}(v)}{\partial v} B_z \tag{2.3.1}$$

where v is the velocity coordinate ($c\Delta\lambda/\lambda$) associated with a wavelength shift $\Delta\lambda$ from line center wavelength λ, g is the Landé factor, $I_{loc}(v)$ is the local profile of the selected line, B_z is the local longitudinal magnetic field component. It is assumed that $I_{loc}(v)$ is similar in shape for all lines and also scale it up in depth with the local line central depth d, then it is obtained:

$$V_{loc}(v) = g\lambda\, d\, k_B(v) \tag{2.3.2}$$

where $k_B(v)$ is a proportionality function equal for all lines. Integrating the equation above (Eq. 2.3.2) over the whole rotating star, it is obtained:

$$V(v) = w\, Z(v) \tag{2.3.3}$$

The integral function $Z(v)$ is called *mean Zeeman signature*. It is also assumed the wavelength-independent limb darkening. Then, the function $Z(v)$ is constant for all lines and its shape is reproduced by all Stokes $V(v)$ profiles with a scaling factor $w = g\lambda d$.

Next step is to define *the line pattern function* $M(v)$ (*a line mask*) as:

$$M(v) = \sum_i w_i\, \delta(v - v_i) \tag{2.3.4}$$

where v_i is the position in velocity space of each spectral line, w_i is the weight of each spectral line, δ is the Dirac delta function. Then, *the circularly polarized spectrum* $\boldsymbol{V}$ can be written as a convolution expression:

$$V = M^* Z \tag{2.3.5}$$

The least-squares solution for Z is:

$$Z = ({}^tM \cdot S^2 \cdot M)^{-1}\, {}^tM \cdot S^2 \cdot V \tag{2.3.6}$$

where S is the square diagonal matrix whose element S_{jj} contains the inverse error bar $1/\sigma_j$ of spectral pixel j. The right-hand part of the equation (Eq. 2.3.6) (denoted ${}^tM \cdot S^2 \cdot V$) is a cross-correlation of the observed spectrum V with a line pattern M (a weighted mean of all lines selected for the analysis). In this way it is possible to deconvolve the raw cross-correlation vector from the autocorrelation matrix ${}^tM \cdot S^2 \cdot M$ and to provide a set of error

bars for the mean Zeeman signature Z. This process is called *least-squares deconvolution* or *LSD*. Also, *LSD* has a built-in automatic and iterative stray pixel rejection routine (due to cosmic ray hits or dead CCD lines/columns).

LSD unpolarized Stokes I and circularly polarized Stokes V profiles are shown in Fig. 2.10, obtained on November 20, 2010 at *ESPaDOnS*. A magnetic field was detected. It could be seen from the plot that the spectral location of the Zeeman signatures and the line profiles are very well correlated. In the middle is the diagnostic null profile N, which serves to diagnose the presence of spurious contributions to the Stokes V spectrum. Checking that a signal is detected only in V and not in N and that it is located within the line profile velocity interval, enables us to conclude that it corresponds to a true polarization. Stokes I and V profiles are normalized with respect to the continuum intensity. *Null* profile and Stokes V profile are expanded by a factor of 200 and shifted vertically for display purposes. For computing that Stokes V profile 12 720 spectral lines were used.

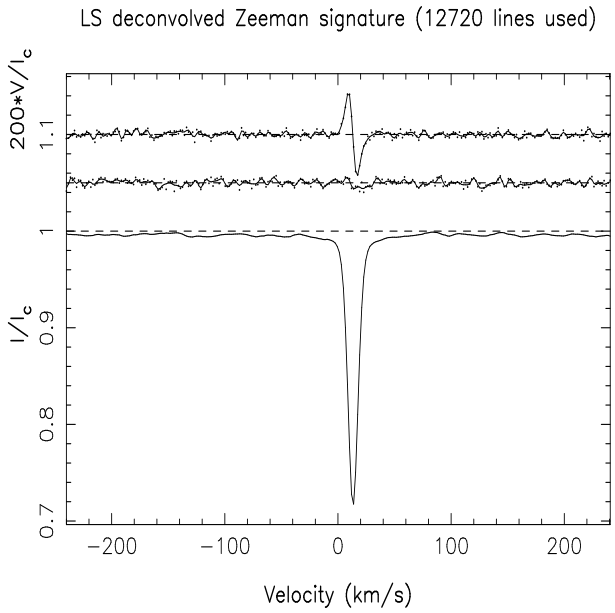

Figure 2.10: *LSD profiles of β Ceti observed on November 20, 2010 at ESPaDOnS. From top to bottom: mean Stokes V profile; diagnostic null spectrum N; mean Stokes I profile.*

The *LSD* method serves to compute the longitudinal magnetic field B_l (the averaged over the visible hemisphere magnetic filed and then projected over the line-of-sight) from both *LSD* Stokes I and V profiles (Stokes V

is only sensitive to the longitudinal component of the magnetic field, while Stokes Q and U are responsible for its transverse component). To obtain B_l (in G) the first-order moment method was used with the following equation (Rees & Semel 1979, Donati et al. 1997, Wade et al. 2000 a, b):

$$B_l = -2.14 \times 10^{11} \frac{\int vV(v)\, dv}{\lambda g_{eff} c \int [1 - I(v)]\, dv} \tag{2.3.7}$$

where v (in km/s) is the radial velocity in the stellar restframe, λ (in nm) is the mean wavelength of all spectral features involved in the LSD process, g_{eff} the effective Landé factor, and c (in km/s) the light velocity in vacuum. The first moment was computed between radial velocity boundaries set to encompass the whole velocity span of Stokes V signatures.

2.4 *Zeeman Doppler Imaging (ZDI) inversion technique*

The term *"Doppler Imaging"* comes from Vogt & Penrod (1983). In their paper they show that spots, moving across the stellar disk due to the rotation of the star, cause bumps in the line profiles and using that information they derive an image of the surface of the RS CVn system HD 1099.

The Doppler Imaging technique (DI) aims to reconstruct a two-dimensional image with the spot distribution over the stellar surface using a time-series of spectral line profiles as a star rotates. The rotation broadening of a line profile should be significantly larger than the local line profile. The idea is that the existence of a spot modifies the flux, which is integrated over the stellar disk. Thus, it produces a bump in the profile of every photospheric absorption line and an overall depression of the continuum. As the star rotates, the bump will move across the line profile. This is shown in Fig. 2.11 for one single spot and in Fig. 2.12 for two spots. Knowing the properties of the spot signatures, like the fraction of the rotational cycle and the length of time for which a spot remains visible, the time at which spot signatures cross the center of the line profile, the amplitude of their sinusoids, could give information about their latitudes, longitudes, the inclination of the stellar rotation axis to the line-of-sight, axial inclination of the star. Spots, which are close to the stellar rotational pole, produce distortions that are visible during most of the rotational cycle and are confined to the line center. Spots, which are near to the stellar equator, produce distortions that are visible during roughly half of the cycle and are observed to move with time from the blue to the red wing.

Spatial resolution of the maps depends on the phase distribution of the spectra.

DI has been used very successfully to reconstruct temperature maps of cool stars (Strassmeier 2002) and abundance maps of *Ap* stars (Kochukhov et al. 2004).

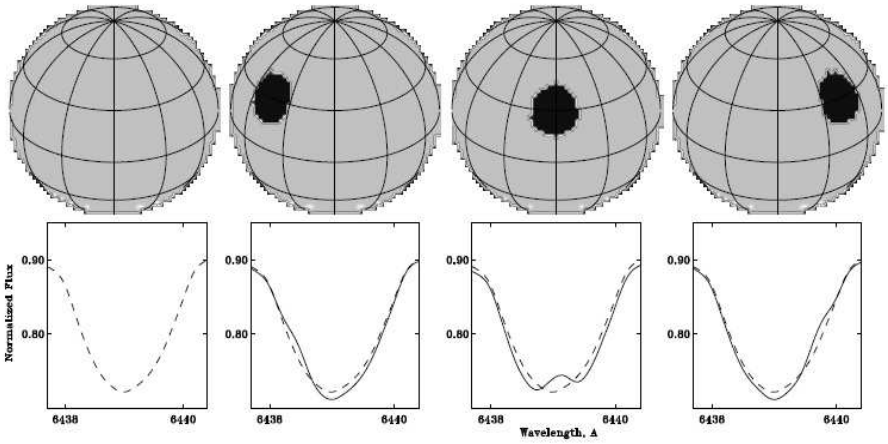

Figure 2.11: *Schematic view of the formation of the "bump" over the rotationally-broadened line profile, produced by one spot. Dashed line is for a star with no spots. Solid line stands for a star with a spot moving across the disk as the star rotates (Berdyugina 2005).*

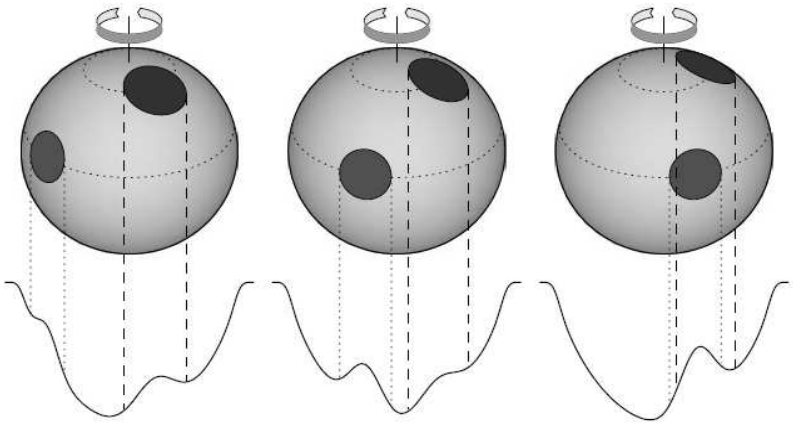

Figure 2.12: *The distortion of a spectral line, produced by two spots.*

Zeeman Doppler Imaging (ZDI) follows the same approach as DI, but investigating polarized light (Semel 1989, Donati & Brown 1997, Donati et al. 2006 b), that could give information about the magnetic field structures on the stellar surface. One star should be observed at different phases, so the magnetic field vector would be observed under different projection angles, which will give different information about the polarized light signatures – field components may be invisible at one phase and visible with large Stokes parameters at other phases. The other requirement of the method is the Stokes profiles to have high signal-to-noise ratio. This could be achieved with the LSD technique, described in Sec. 2.3.

The changes in the profile of Stokes V signatures, caused by a moving spot, are shown in Fig. 2.13. The 2 panels show a spot, which hosts radial field (perpendicular to the stellar surface), so the circular polarization signature keeps the same sign as the spot crosses the line profile.

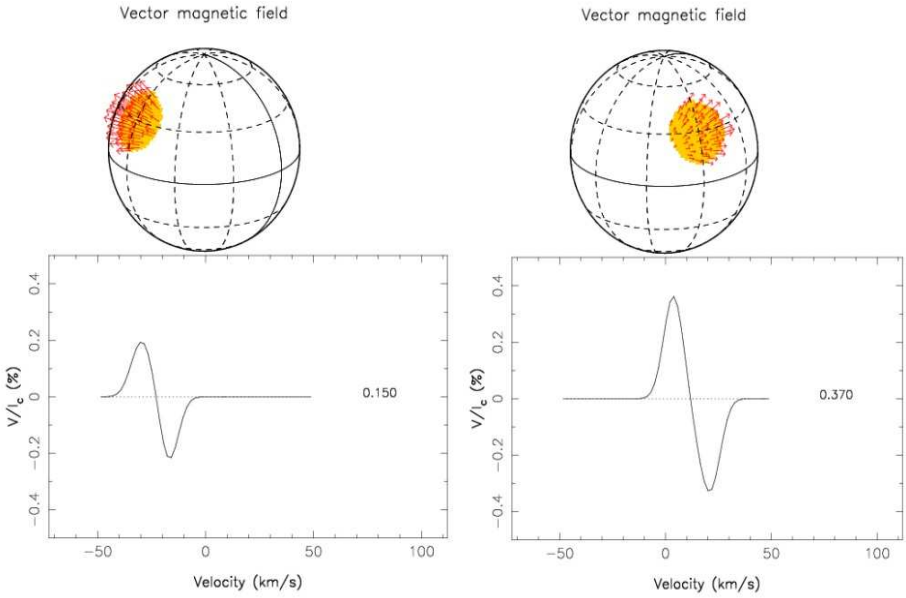

Figure 2.13: *The variation of Stokes V profiles, while a spot, which hosts radial field, is crossing. Image credit by J.-F. Donati (http://www.ast.obs-mip.fr/article.php3?id_article=457).*

ZDI is based on the original algorithm for maximum-entropy image reconstruction by Skilling & Bryan (1984). Details on the maximum-entropy inversion code are described in Brown et al. (1991). The recent implementation of ZDI is that surface magnetic field vector is projected onto a

spherical harmonics frame, which allows to easily distinguish between the poloidal and toroidal components of the magnetic field (Donati 2001, Donati et al. 2006 b). Following this idea, it is used a formalism similar to that of Jardine et al. (1999), so that the field components could be written as:

$$B_r(\theta,\phi) = -\sum_{l,m} \alpha_{l,m} Y_{l,m}(\theta,\phi) \tag{2.4.1}$$

$$B_\theta(\theta,\phi) = -\sum_{l,m} [\beta_{l,m} Z_{l,m}(\theta,\phi) + \gamma_{l,m} X_{l,m}(\theta,\phi)] \tag{2.4.2}$$

$$B_\phi(\theta,\phi) = -\sum_{l,m} [\beta_{l,m} X_{l,m}(\theta,\phi) - \gamma_{l,m} Z_{l,m}(\theta,\phi)] \tag{2.4.3}$$

where

$$Y_{l,m}(\theta,\phi) = c_{l,m} P_{l,m}(\theta) e^{im\phi} \tag{2.4.4}$$

$$Z_{l,m}(\theta,\phi) = \frac{c_{l,m}}{l+1} \frac{\partial P_{l,m}(\theta)}{\partial \theta} e^{im\phi} \tag{2.4.5}$$

$$X_{l,m}(\theta,\phi) = \frac{c_{l,m}}{l+1} \frac{P_{l,m}(\theta)}{\sin\theta} ime^{im\phi} \tag{2.4.6}$$

$$c_{l,m} = \sqrt{\frac{2l+1}{4\pi} \frac{(l-m)!}{(l+m)!}} \tag{2.4.7}$$

where l and m are the order and degree of the spherical harmonic mode $Y_{l,m}(\theta,\phi)$, θ and ϕ are the colatitude and longitude at the surface of the star, $P_{l,m}(\theta)$ the associated Legendre polynomial, $\alpha_{l,m}$ is the radial field component, $\beta_{l,m}$ – the azimuthal and meridional components of the poloidal field term, $\gamma_{l,m}$ – the azimuthal and meridional components of the toroidal field term. A set of complex coefficients $\alpha_{l,m}$, $\beta_{l,m}$ and $\gamma_{l,m}$ allows to produce a magnetic map of a stellar surface and the corresponding Stokes V data set. The inverse problem is to reconstruct a set of complex coefficients from an automated, iterative fit to the observed circularly polarized LSD profiles. So, the method performs iterative adjustment of the observed time series of LSD polarized profiles by a simulated set of Stokes V profiles. The synthetic Stokes profiles are calculated from an artificial star, whose surface is divided into a grid of rectangular pixels of roughly similar area. Each surface pixel is associated with a local Stokes I and V profile. Stokes I line profile is assumed to possess a Gaussian shape, with a depth and width adjusted to

achieve the best fit between synthetic and observed line profiles. Assuming a given magnetic field strength and orientation for each pixel, local Stokes V profiles are calculated under the weak-field assumption (applicable for field strengths lower than 1 kG) (Morin et al. 2008 b, Petit et al. 2010, Morgenthaler et al. 2012). In that weak-field regime circular polarization is sensitive to the magnetic flux and Stokes I profiles are sensitive to field strength and filling factors.

The sensitivity of ZDI from circular polarization alone to the orientation of the magnetic field vectors is studied by Donati & Brown (1997). They show that ZDI code is very good at distinguishing azimuthal from radial/meridional field features. For high latitudes there is no crosstalk between radial and meridional maps. But a crosstalk appears for low latitude features from radial to meridional filed components for low inclination angles and from meridional to radial field components at high inclination angles. Another example about the crosstalk issue could be found in Donati (2001).

2.5 *Differential rotation*

Differential rotation plays an important role in the generation of magnetic fields in the convective zone. According to the theoretical dynamo models, differential rotation is responsible for the Ω-effect, which transforms a poloidal magnetic field into a toroidal field (Chapter 1). The law for solar differential rotation is:

$$\Omega(l) = \Omega_{eg} - d\Omega \, \sin^2 l \tag{2.5.1}$$

where $\Omega(l)$ is the rotation rate at latitude l, Ω_{eq} is the rotation rate of the equator, $d\Omega$ is the difference in the rotation rate between the pole and equator.

The technique, which is used here, is based on the *"entropy landscape method"* using the principles of maximum-entropy image reconstruction and is described in details in Petit et al. (2002) and Donati et al. (2003 b). They derive the differential rotation parameters through magnetic imaging from circularly polarized data. It is also assumed a given surface differential rotation law, presented by Eq. 2.5.1, and is used in the image reconstruction process.

The main idea is that there are pairs of parameters $(\Omega_{eq}, d\Omega)$ in two-dimensional (2D) parameter space. For each of the pairs, there is one reconstructed magnetic image of the stellar surface. The optimal differential rotation parameters are chosen by minimizing the information content of the reconstructed image through a 2D paraboloid fit. In other words, when the

assumed differential rotation law is close to the real one, then the features on the reconstructed image should be sharper, the entropy should be higher, which gives the smaller information content, which in our case is the mean magnetic field intensity over the stellar surface.

The next step consists in deriving the error bars. Now, the value of the mean magnetic field intensity, which is derived from the previos step, is fixed and again are reconstructed magnetic maps for pairs of $(\Omega_{eq}, d\Omega)$, but this time the idea is to minimize the χ^2 of the reconstructed maps at a constant image entropy.

2.6 *Line activity indicators*

The chromosphere is a thick region with non-radiative (mechanical) heating and cooling, which occurs mainly by radiation in strong resonance lines (rather than in the continuum, which is the case for the photosphere) (review on the topic by Hall 2008). A resonance line is a line, produced by transition between the ground state and some of the excited levels of the atom. Example of resonance lines are CaII K&H ($\lambda\lambda$ 3968, 3933), MgII h&k ($\lambda\lambda$ 2803, 2796), CII ($\lambda\lambda$ 1334, 1335) and etc. A subordinate line is a line, produced by transition between two excited levels of the atom. Example of subordinate lines are CaII infrared triplet (CaII IRT $\lambda\lambda\lambda$ 8498, 8542, 8662), $H\alpha$ and other hydrogen lines from Balmer series and etc.

The temperature profile vs. height of the chromosphere of the Sun and the formation regions of some lines are presented in Fig. 2.14 (Vernazza et al. 1981). This figure shows that after reaching a minimum value at the base of the chromosphere ($\sim 4000\ K$), the temperature steeply rises to $10^5\ K$ in the transition region and over $10^6 - 10^7\ K$ in the corona.

The observed overheating of the chromosphere and corona is caused by a non-thermal mechanism. According to the extended studies of Narain & Ulmschneider (1990, 1996) about the extra heating of the outer atmospheres, they discuss various extra heating sources, which could be divided into two main categories – a hydrodynamic mechanism (dissipation of acoustic energy and pulsation waves) and a magnetic mechanism (magnetohydrodynamic waves and magnetic field dissipation).

Because of that extra heat energy, there is a radiative excess in spectral lines, mainly those from singly ionized metals and neutral hydrogen, described in details by Anderson & Athay (1989). The core emission in the lines CaII K&H and MgII h&k is a typical example for such an emission, attributed to an outward temperature rise in the chromosphere, which is ultimately generated by non-thermal heating. Throughout most of the chro-

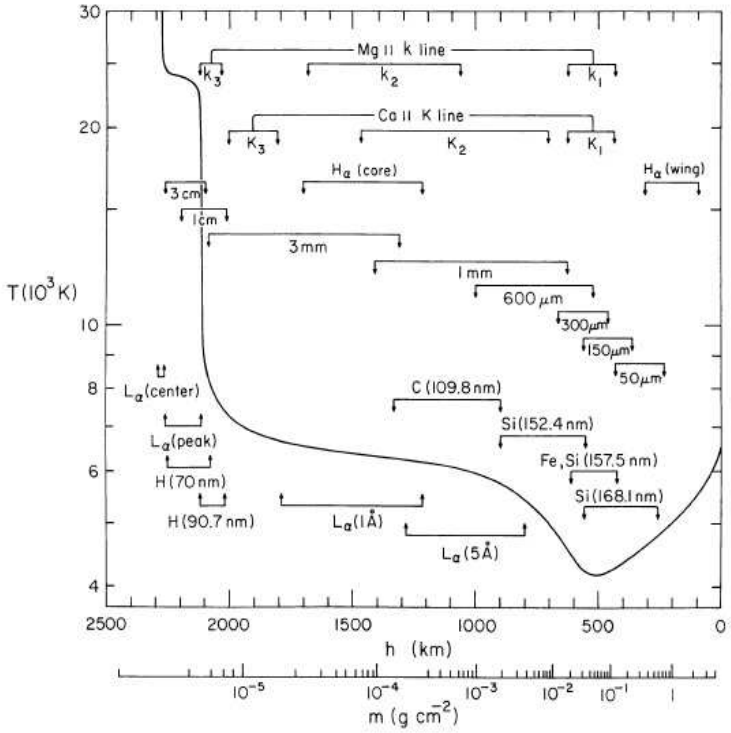

Figure 2.14: *The temperature structure with the height of the Sun, derived from a semi-empirical model of the solar chromosphere, computed by Vernazza et al. (1981). It shows also the regions of formation of some lines.*

mosphere, the cooling is dominated by the three common metal ions with easily excited electrons MgII, CaII and the iron group (Skumanich et al. 1975, Linsky 1980, Anderson & Athay 1989 and the references therein). In the uppermost layers $Ly\alpha$ (λ 1216) begins to contribute to the cooling.

The line activity indicators, which are measured in this work, are $H\alpha$ and CaII infrared triplet component at 854.2 nm regarding the normalized continuum (R_c). Also, it is estimated the core emission of the CaII K line through the intensity ratio between the line core and the continuum intensity at 395 nm. Then, the variability of B_l, which is a vectorial quantity, is compared with the variability of the activity indicators, which are integral quantities, in order to have more information about how complex is the surface magnetic structure and whether there are small-scale elements.

The typical profiles of the lines $H\alpha$, CaII IRT at 854.2 nm and CaII K&H from top to bottom are shown in Fig. 2.15, Fig. 2.16 and Fig. 2.17 for the three studied stars β Ceti, EK Eri and V390 Aur, respectively.

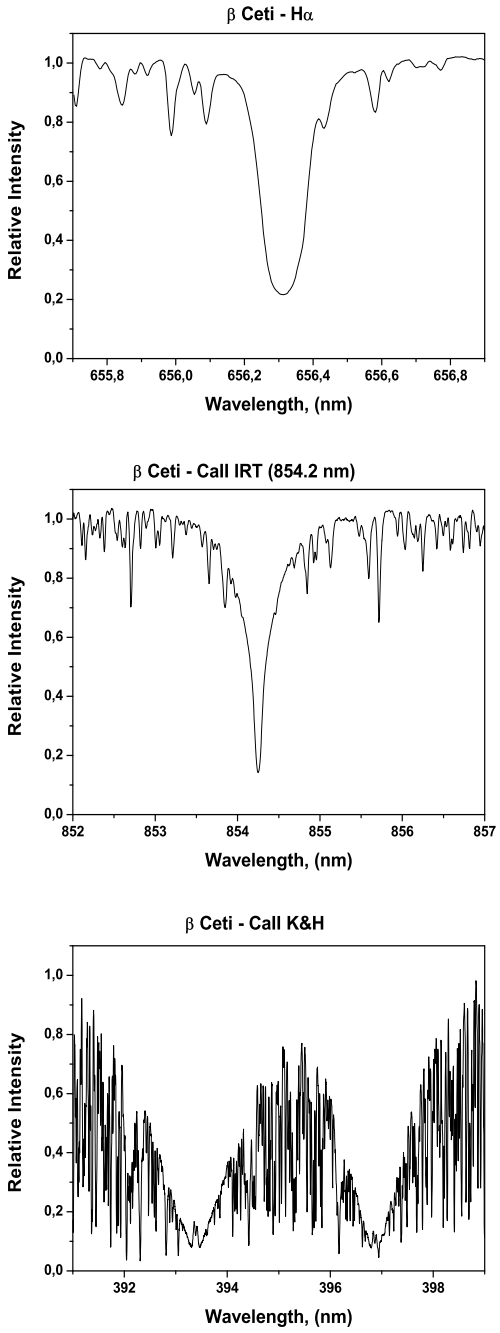

Figure 2.15: *The line profiles of $H\alpha$, CaII IRT at* 854.2 *nm and CaII K&H from top to bottom for β Ceti (July 17, 2010).*

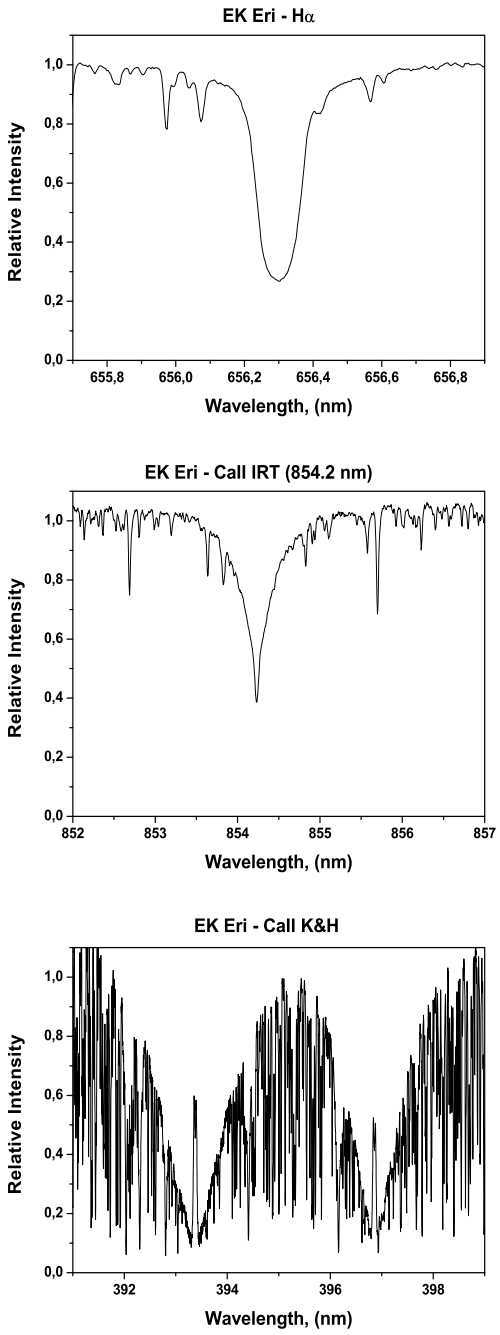

Figure 2.16: *The line profiles of $H\alpha$, CaII IRT at* 854.2 *nm and CaII K&H from top to bottom for EK Eri (March 21, 2011).*

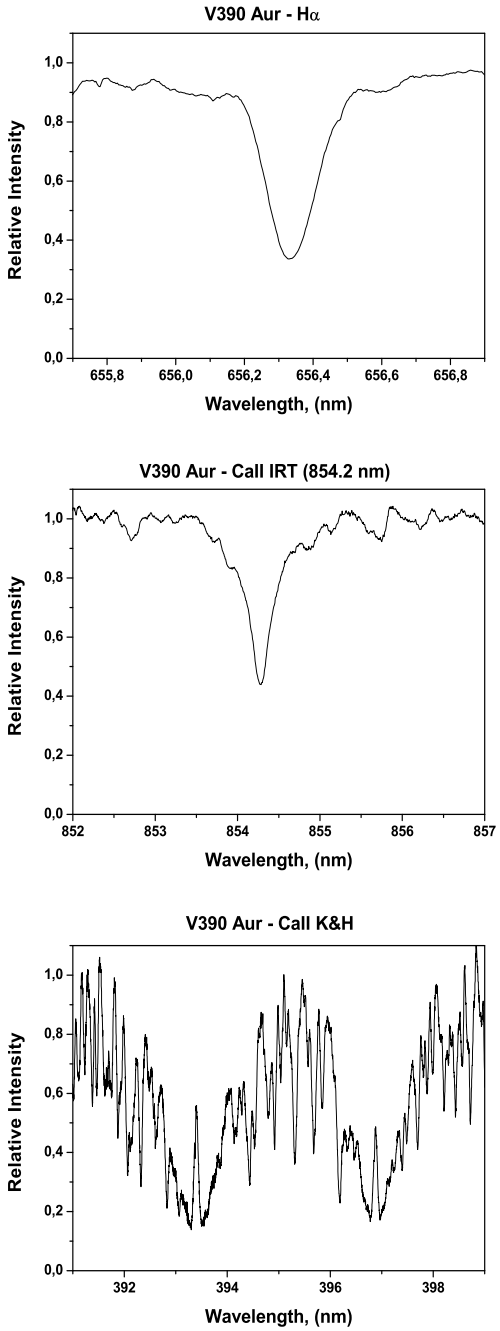

Figure 2.17: *The line profiles of Hα, CaII IRT at* 854.2 *nm and CaII K&H from top to bottom for V390 Aur (September 14, 2008).*

Another qualitative indicator for magnetic activity, measuring chromospheric variations, is the *S-index* – a dimensionless ratio of the emission in the line cores of CaII K&H to the emission in two nearby continuum bandpasses on either side of the H and K lines:

$$S \sim \frac{F_H + F_K}{F_R + F_V} \tag{2.6.1}$$

It was proposed as a magnetic indicator by Wilson in 1966, when he began the *"Mount Wilson HK-Project"* at the Mount Wilson observatory – it was a long-term monitoring program, searching for chromospheric variations in main sequence stars (Wilson 1968, 1978, Vaughan et al. 1978) and including some evolved stars as well (Duncan et al. 1991).

2.7 *Radial velocity*

Radial velocities (RV) are measured from the shift in wavelength of a spectrum compared to a certain standard. The RV variability has been suggested to result from one or more than one of the following mechanisms simultaneously (Setiawan et al. 2004, Setiawan et al. 2005, Hekker 2007, Hekker et al. 2008):

- a stellar companion – the whole spectrum will shift, but retain its shape (except in case of a transit, which provides a spot like variation); a star will show RV variability due to the reflex motion of the star induced by the companion (according to Newton's third law of reaction).

- intrinsic mechanisms, which only mimic the RV variability, such as oscillations and rotational modulation – they change the shape of the spectral lines. The visible stellar surface could be divided in small surface elements. Every element contributes to the overal stellar spectrum. In the case of oscillations, parts of the star are slightly blue shifted, while others are slightly red shifted. At some epoch, the largest fraction of the visible surface of the star is blue shifted and thus the blue part of a spectral line will be enhanced, compared to the red part. At a later epoch, the largest part of the star may be red shifted and the red side of a spectral line will be enhanced, compared to the blue side. The case of dark (light) spots on the stellar surface is similar – a spectral line is reduced (enhanced) on either the red or blue side. But the star rotates and the spots change their possitions on the stellar surface, so another part of the spectral line is reduced (enhanced).

Therefore, line profile analysis can be used to discriminate between these mechanisms.

In the present work, radial velocity is measured on the LSD Stokes I line profiles by simply performing the χ^2 adjustment of a Gaussian function on the line core and then taking the central velocity of the Gaussian as our RV value. Time variations of RV are compared with the time variations of the line activity indicators and B_l.

Chapter 3

The slowly rotating EK Eri and β Ceti

In this chapter are studied two slowly rotating single giants – β Ceti ($K0III$ and $v \sin i = 3.5\ km/s$) and EK Eri ($G8III - IV$ and $v \sin i = 0.5\ km/s$). Observational data were obtained with the spectropolarimeters *Narval* and *ESPaDOnS*. The LSD method and ZDI inversion technique are applied. The surface-averaged longitudinal magnetic field B_l, line activity indicators $H\alpha$, CaII K, CaII IR, S-index and radial velocity are measured and their time variations are compared. The large-scale magnetic fields are reconstructed for both stars. They show that the global magnetic fields of β Ceti and EK Eri are dominated by a dipolar configuration. It is proposed that both stars are descendants of *Ap* stars.

3.1 β *Ceti*

The star β Ceti (HD 4128, HR 188, HIP 3419) is one of the magnetic single late-type giants from the sample of Aurière et al. (2009 a). It is a star of spectral class $K0III$ with $V = 2.04\ mag$ and $B - V = 1.02\ mag$. Its value of $V - R = 0.72\ mag$ places it to the left of the coronal dividing line in the Hertzsprung-Russel diagram, where stars are supposed to have a chromosphere, a transition region, and a corona. That dividing line was proposed by Linsky & Haisch (1979) near $V - R = 0.80\ mag$ and later confirmed by the study of Simon et al. (1982) with a larger sample of stars. In the solar neighborhood ($d \leq 30\ pc$), β Ceti is the single giant star with the highest X-ray luminosity $\log L_x = 30.2\ erg/s$ (Maggio et al. 1998, Hünsch et al. 1996), which is calculated assuming a distance of $d = 29.5\ pc$ based

on the Hipparcos parallax (van Leeuwen 2007). This high X-ray emission reaches a level comparable to that of Capella (RS CVn type) and θ^1 Tau ($K0III$, in the Hyades open cluster) and reveals an extended corona. An atmospheric model of β Ceti was simulated by Eriksson et al. (1983), which suggested there are coronal loops. Ayres et al. (2001) reported a series of striking coronal flare events observed with EUVE during a period of 34 days starting on 1 Aug 2000, confirming the strong activity of this single giant.

3.1.1 *Observations and data reduction*

Observational data were obtained with the two twin fiber-fed échelle spectropolarimeters *Narval* (Aurière 2003) and *ESPaDOnS* (Donati et al. 2006 a) (instruments are described in Chapter 2).

Thirty-eight spectra have been collected for β Ceti in the period June 2010 – January 2012 (Table 3.1). First, reduced spectra were extracted using the automatic reduction software LibreEsprit, developed for *Narval* and *ESPaDOnS*. A detailed description of the algorithm implemented in this software can be found in Donati et al. (1997). As a second step, the *LSD* multiline technique (Donati et al. 1997) was applied to all observations. This widely used cross-correlation technique enables averaging of several thousand absorption atomic lines recorded throughout the échelle spectrum, generating a single Stokes I and V line profile. We employed here a line mask created from Kurucz (1993) atmospheric models. The line mask was calculated for an effective temperature of $T_{eff} = 5000\ K$, $\log g = 3.0$ and a microturbulence of $2\ km/s$, consistent with the literature data for β Ceti (Thevenin 1998, Hekker & Meléndez 2007, Massarotti et al. 2008), resulting in a total of about 12 700 spectral lines (selecting lines with a depth greater that $0.1 I_c$, where I_c is the continuum level, and after removal of chromospheric lines and of spectral domains affected by telluring bands). By doing so, the signal-to-noise ratio (S/N) is increased to the point where weak polarized Zeeman signatures can be detected in all 38 spectra, thanks to a final S/N of up to 56 000.

Table 3.1: *Measured longitudinal magnetic field, activity indicators, radial velocity, and their uncertainties for β Ceti. In the first column capital letters N and E stand for Narval (TBL, Pic du Midi, France) and ESPaDOnS (CFHT), respectively. The fifth column gives the signal-to-noise ratio (S/N) of each Stokes V LSD profile.*

Inst.	Date UT	HJD	Rot. phase	S/N (LSD)	CAII K	σ	$H\alpha$	σ	CaII IR	σ	B_l [G]	σ [G]	RV [km/s]
E	20 Jun 10	2455368.123	0.891	73 412	0.191	0.005	0.211	0.002	0.134	0.003	4.4	0.4	13.36
E	22 Jun 10	2455370.134	0.901	63 268	0.194	0.004	0.214	0.001	0.135	0.003	3.9	0.4	13.36
E	17 Jul 10	2455395.140	0.017	78 329	0.210	0.004	0.220	0.001	0.141	0.001	7.4	0.3	13.36
E	18 Jul 10	2455396.132	0.022	64 598	0.216	0.005	0.217	0.001	0.144	0.002	8.1	0.4	13.38
E	26 Jul 10	2455404.138	0.059	30 276	0.207	0.012	0.215	0.001	0.146	0.000	8.2	0.9	13.47
E	05 Aug 10	2455414.006	0.105	64 982	0.218	0.005	0.213	0.001	0.147	0.001	7.2	0.4	13.45
N	07 Aug 10	2455415.633	0.112	50 740	0.197	0.007	0.211	0.002	0.149	0.001	7.0	0.5	13.44
N	17 Aug 10	2455425.685	0.159	59 498	0.201	0.004	0.221	0.002	0.148	0.003	4.5	0.5	13.43
N	03 Sep 10	2455442.699	0.238	55 431	0.189	0.007	0.218	0.001	0.147	0.001	2.8	0.4	13.36
N	19 Sep 10	2455459.473	0.316	69 382	0.187	0.005	0.211	0.002	0.142	0.001	1.2	0.4	13.36
N	26 Sep 10	2455466.500	0.349	70 223	0.198	0.006	0.215	0.001	0.147	0.002	0.1	0.4	13.35
N	06 Oct 10	2455475.518	0.391	40 356	0.212	0.007	0.215	0.002	0.155	0.002	1.8	0.7	13.43
N	13 Oct 10	2455483.475	0.428	72 465	0.230	0.005	0.213	0.001	0.165	0.001	3.6	0.4	13.44
E	16 Oct 10	2455485.832	0.439	65 746	0.216	0.003	0.223	0.002	0.155	0.002	3.9	0.4	13.43
E	17 Oct 10	2455486.863	0.444	68 396	0.222	0.006	0.217	0.001	0.154	0.001	3.8	0.3	13.42
N	20 Oct 10	2455490.471	0.460	31 993	0.211	0.016	0.213	0.001	0.158	0.001	5.1	0.8	13.46
N	12 Nov 10	2455513.360	0.567	37 268	0.199	0.004	0.212	0.002	0.149	0.004	4.9	0.7	13.40

Table 3.1 Continued:

Inst.	Date UT	HJD	Rot. phase	S/N (LSD)	CAII K	σ	$H\alpha$	σ	CaII IR	σ	B_l [G]	σ [G]	RV [km/s]
E	16 Nov 10	2455516.831	0.583	61 599	0.202	0.003	0.222	0.002	0.142	0.003	4.0	0.4	13.35
E	21 Nov 10	2455521.798	0.606	59 370	0.197	0.007	0.212	0.002	0.137	0.001	4.2	0.5	13.31
E	22 Nov 10	2455522.718	0.610	73 414	0.195	0.006	0.212	0.004	0.137	0.004	3.9	0.4	13.34
N	26 Nov 10	2455527.368	0.632	61 161	0.185	0.004	0.212	0.001	0.136	0.003	4.5	0.4	13.26
E	28 Nov 10	2455528.855	0.639	65 837	0.196	0.006	0.212	0.002	0.137	0.002	3.9	0.4	13.32
N	04 Dec 10	2455535.349	0.669	41 811	0.175	0.009	0.207	0.001	0.138	0.003	4.8	0.6	13.35
N	12 Dec 10	2455543.383	0.706	29 688	0.175	0.010	0.211	0.001	0.139	0.002	5.0	0.8	13.32
N	14 Dec 10	2455545.292	0.715	22 465	0.167	0.013	0.208	0.002	0.147	0.003	5.3	1.1	13.24
E	19 Jun 11	2455732.097	0.584	29 427	0.211	0.016	0.204	0.003	0.136	0.004	4.3	0.8	13.41
E	22 Jun 11	2455735.130	0.598	74 032	0.213	0.007	0.205	0.002	0.135	0.003	4.1	0.4	13.41
E	08 Jul 11	2455751.132	0.673	41 771	0.227	0.010	0.208	0.001	0.145	0.004	4.7	0.6	13.42
E	13 Jul 11	2455756.134	0.696	52 216	0.225	0.009	0.208	0.003	0.145	0.005	4.2	0.5	13.35
E	15 Jul 11	2455758.138	0.705	62 607	0.226	0.007	0.214	0.003	0.145	0.005	4.6	0.4	13.39
N	25 Sep 11	2455829.535	0.037	50 501	0.205	0.005	0.222	0.002	0.157	0.002	6.7	0.5	13.39
N	10 Oct 11	2455845.407	0.111	47 385	0.206	0.008	0.223	0.002	0.151	0.002	6.0	0.6	13.38
E	30 Oct 11	2455865.444	0.204	54 215	0.183	0.006	0.208	0.005	0.141	0.002	3.7	0.5	13.38
N	16 Nov 11	2455882.425	0.283	55 492	0.180	0.009	0.211	0.004	0.143	0.005	4.3	0.4	13.34
N	27 Nov 11	2455893.309	0.334	60 720	0.191	0.006	0.216	0.006	0.147	0.005	2.7	0.4	13.35
N	08 Dec 11	2455904.316	0.385	60 838	0.203	0.006	0.216	0.002	0.154	0.005	1.3	0.4	13.35
N	09 Jan 12	2455936.252	0.534	49 042	0.209	0.005	0.216	0.002	0.159	0.005	4.0	0.5	13.25
N	22 Jan 12	2455949.279	0.594	61 673	0.184	0.004	0.213	0.001	0.145	0.003	5.2	0.4	13.32

As a first estimate of the magnetic field strength, we computed the longitudinal component of the magnetic field (B_l), using the first-order moment method (Rees & Semel 1979, Donati et al. 1997, Wade et al. 2000 a, b). According to the multiline model, we assumed here that the LSD line profiles possess a mean wavelength of 597 nm and a Landé factor of 1.28. The first moment was computed between radial velocity boundaries set to encompass the whole velocity span of Stokes V signatures. For β Ceti that integration window has velocity boundaries of ± 19 km/s around the line center of LSD profiles. The longitudinal magnetic field B_l (expressed in gauss) was computed from both LSD Stokes I and V profiles with the equation Eq. 2.3.7, which is shown in Sec. 2.3.

We also took advantage of several classical activity proxies showing up in the spectra. We measured the line depths for $H\alpha$ and for the CaII infrared triplet component at 854.2 nm regarding the normalized continuum (R_c). We estimated the core emission of the CaII K line through the intensity ratio between the line core and the continuum intensity at 395 nm. We measured the radial velocity (RV) of the LSD Stokes I line profiles by simply performing the χ^2 adjustment of a Gaussian function on the line core and then taking the central velocity of the Gaussian as our RV value.

3.1.2 *Magnetic field, line activity indicators and radial velocity*

All Stokes V profiles of β Ceti have a simple shape with a peak-to-peak amplitude varying from $9.7 \times 10^{-5} I_c$ to $6.4 \times 10^{-4} I_c$ in 2010 and from $1.3 \times 10^{-4} I_c$ to $6 \times 10^{-4} I_c$ in 2011/2012. All line profiles feature a positive blue lobe and a negative red lobe, which corresponds to a field of positive polarity. Accordingly, B_l estimates stay with a positive sign for the whole observational period (see Table 3.1 and Fig. 3.1). Thanks to a typical error bar as low as 0.5 G, significant variations are observed in the interval $0.1 - 8.2$ G in 2010 and $1.3 - 6.7$ G in 2011/2012. The smaller amplitude of variations observed in 2011/2012 may be plausibly explained by the fact that the maximum values of B_l have been missed in this dataset, due to the lack of observations between $HJD = 2455545$ and $HJD = 2455730$. We also noticed that B_l displays almost sinusoidal temporal variations (Fig. 3.1) that would make the large-scale field distribution roughly consistent with a simple dipolar configuration (Landstreet & Mathys 2000).

The chromospheric activity measurements derived from CaII K, CaII IRT, and $H\alpha$, as well as their uncertainties, are also listed in Table 3.1 and overplotted with the B_l estimates in Fig. 3.1. Chromospheric emission follows

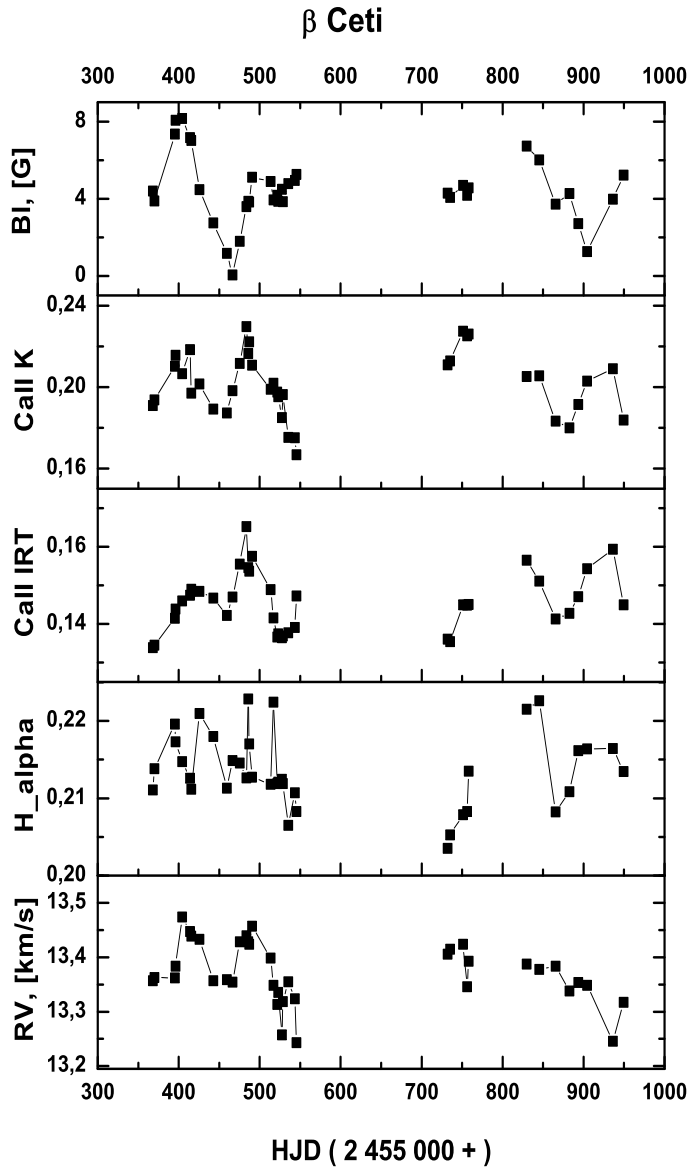

Figure 3.1: *From top to bottom are presented the variations in B_l and the activity indicators CaII K, CaII IRT, Hα, and the radial velocity in the period June 2010 – January 2012.*

the same general variations as B_l, especially for CaII K. This good agreement provides us with another hint that the surface magnetic geometry of β Ceti is topologically rather simple. If B_l provides us with a selective tracer of the largest scale magnetic structures (owing to the mutual cancellation of

polarized signatures of nearby magnetic regions with opposite polarities), the chromospheric emission is sensitive to the field strength alone and is therefore unaffected by this spatial filtering effect. The good temporal agreement between B_l and chromospheric proxies is therefore indicative of a lack of smaller-scale magnetic regions outside rotational phases of maximum B_l, in striking difference to very active cool stars on the main sequence for which B_l and chromospheric emission seem to be mostly uncorrelated (Morgenthaler et al. 2012).

Temporal variations in the radial velocity are shown in the lower right panel of Fig. 3.1, displaying values in the interval $13.24 - 13.47\ km/s$ (while the RV stability of *Narval* and *ESPaDOnS* was estimated by Moutou et al. (2007) to be of the order on 30 m/s), with relatively good correlation with other activity indicators. In early measurements, Frost (1923) reports $RV = 13.5\ km/s$, while Buscombe & Kennedy (1968) obtained a slightly higher value of $14.1 \pm 0.33\ km/s$. A later estimate of $13.32 \pm 0.05\ km/s$ was proposed by Massarotti et al. (2008), in good agreement with our series of values.

3.1.3 *Zeeman Doppler Imaging*

We exploited the rotational modulation of Stokes V signatures to reconstruct the magnetic topology of the star by means of the Zeeman Doppler Imaging tomographic method (Semel 1989, Donati & Brown 1997, Donati et al. 2006 b). We used a recent implementation of this algorithm where the surface vectorial magnetic field is projected onto a spherical harmonics frame, allowing us to easily distinguish between the poloidal and toroidal components of the surface magnetic geometry (Donati et al. 2006 b). This method performs iterative adjustment of the observed time series of LSD polarized profiles by a simulated set of Stokes V profiles computed for an identical sequence of rotational phases. The synthetic Stokes profiles are calculated from an artificial star whose surface is divided into a grid of 2 000 rectangular pixels of roughly similar area. Each surface pixel is associated with a local Stokes I and V profile.

In this simple model, the local synthetic Stokes I line profile is assumed to possess a Gaussian shape, with a depth and width adjusted to achieve the best fit between synthetic and observed line profiles. Assuming a given magnetic field strength and orientation for each pixel, local Stokes V profiles are calculated under the weak-field assumption (Morin et al. 2008 b, Petit et al. 2010, Morgenthaler et al. 2012). The rotation period, inclination angle, and $v \sin i$ adopted for our model are discussed below. The linear limb darkening coefficient is set to 0.75, in agreement with Claret & Bloemen (2011). We as-

sume here that the surface magnetic field of the star contains both a poloidal and toroidal field component. We limited the spherical harmonics expansion to $l \leq 10$ since no improvement is found for the fits between modeled and observed LSD profiles for higher values of l.

The first step towards the ZDI reconstruction of the magnetic topology of β Ceti is to determine the rotational period of the star. We conducted the period search from the full dataset (June 2010 – January 2012), following the approach of Petit et al. (2002). Two hundred ZDI models were computed, assuming a different rotation period of the star for each model, with a uniform sampling of rotation periods in the 100- to 300-day interval. Forcing a constant information content (i.e. a same average magnetic field strength) in all 200 magnetic topologies, we compared them to the observed Stokes V profiles and analyzed the χ^2 variations over the period span (Fig. 3.2). Our best magnetic model, identified by the lowest χ^2 value, suggests a possible period of 215 days, which we use for the final magnetic map. A slightly shorter period of 199 days was derived by Jordan & Montesinos (1991) using the value of $v \sin i = 3$ km/s given by Gray (1982).

We applied the same maximum-entropy method to look for surface differential rotation (Petit et al. 2002), but did not obtain any conclusive result. The rotational phase of every Stokes V profile (Table 3.1) is computed according to the rotation period of 215 d, with a phase origin at $HJD = 2454101.5$. All data are phased according to the following ephemeris:

$$HJD = 2454101.5 + 215\,\phi \tag{3.1.1}$$

where HJD is the heliocentric Julian date of the observations, and ϕ is the rotational cycle.

It was found from the literature that β Ceti has a rotational velocity in the interval $v \sin i = 3{-}4$ km/s ($3.3{\pm}0.8$ km/s from Smith & Dominy (1979); $4{\pm}1$ km/s from Fekel (1997); $3{\pm}1$ km/s from Carney et al. (2008)). Varying the value of $v \sin i$ over this range in our ZDI models did not significantly affect the resulting maps and χ^2 values. In the rest of this work, we therefore chose an intermediate value $v \sin i = 3.5$ km/s. The inclination angle i of the stellar spin axis is the last ZDI input parameter. A value of $i = 60°$ was proposed by Sanz-Forcada et al. (2002), following parameters from Gray (1989 b). Combining our value of $v \sin i$, our estimate of the stellar radius (see next Sec. 3.1.4) and the rotational period derived from ZDI, we also adopt here $i = 60°$ in the tomographic models.

In this study we present two magnetic maps for β Ceti, choosing to split our time series into two subsets (one for June 2010 – December 2010 and the second one for June 2011 – January 2012, see Figs. 3.3 and 3.4, respectively).

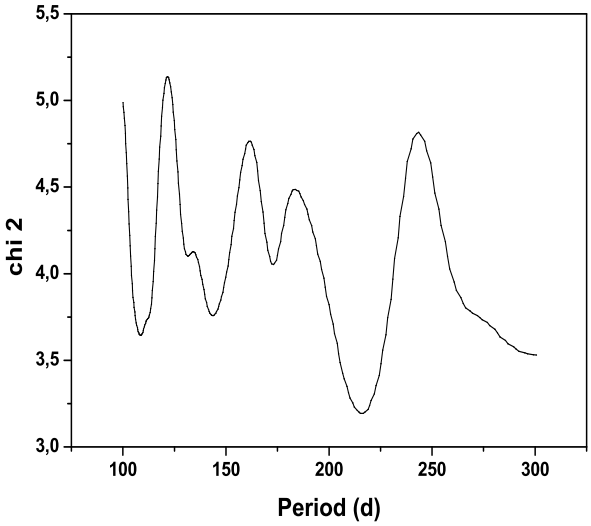

Figure 3.2: *Periodogram obtained using the whole dataset June 2010 – January 2012.*

This strategy is meant to highlight possible changes in the large-scale surface field between the two epochs (if any). The subsets obtained for 2010 and 2011/2012 cover similar time spans and contain 25 and 13 spectra, respectively. According to the rotation period of 215 days, both subsets provide us with sufficiently dense phase sampling to reconstruct a magnetic map, in spite of a lack of observations in the second dataset at phases higher than 0.7.

Both ZDI maps (illustrated in Figs. 3.3 and 3.4) correspond to magnetic models with $\chi^2 = 2.1$. The Stokes V data are therefore not fit at the noise level, mainly because our simplified magnetic model does not offer the possibility of generating asymmetric Zeeman signatures, while the LSD profiles of β Ceti clearly display such asymmetry (with blue lobes generally deeper than red lobes). Such abnormal Stokes V profile shapes have been previously observed on several active stars (Aurière et al. 2008) and most likely originate in vertical gradients of velocity and magnetic field (Lopez Ariste 2002). Previous attempts to get a better fit by implementing an ad hoc asymmetry in the model (Petit et al. 2005) did not significantly modify the resulting magnetic topology.

Most properties of the two magnetic maps are very alike. At both epochs, the magnetic geometry is dominated by the poloidal component of the mag-

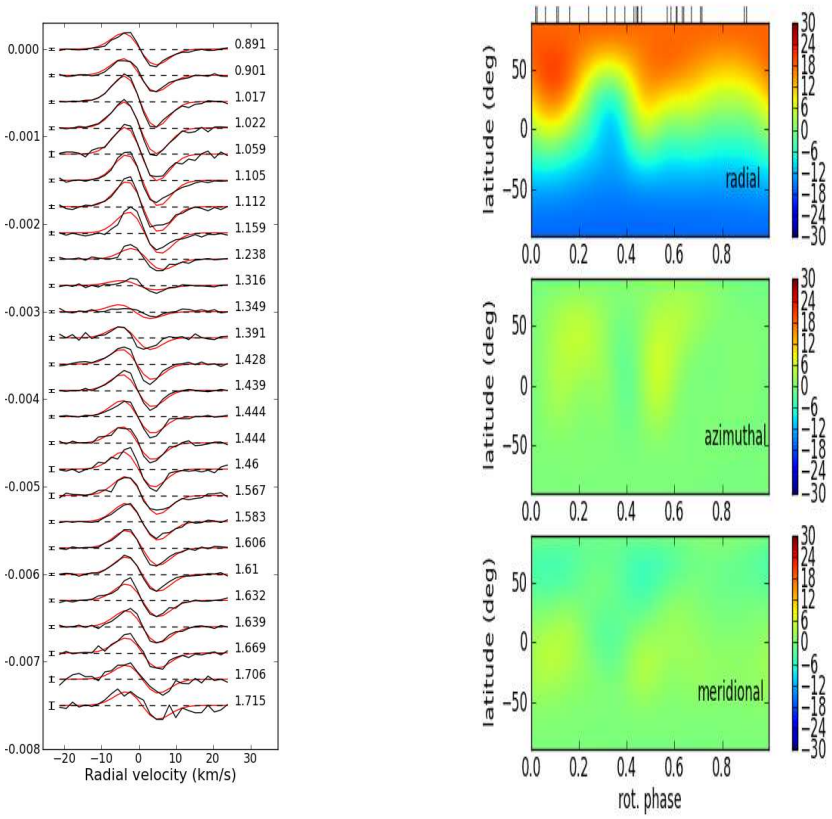

Figure 3.3: *β Ceti in the period June 2010 – December 2010.* ***Left panel:*** *Normalized Stokes V profiles – observed profiles (black lines); synthetic profiles (red lines); zero level (dashed lines). All profiles are shifted vertically for display purposes. The rotational phases of observations are indicated in the right part of the plot and the error bars are on the left of each profile.* ***Right panel:*** *Magnetic map of β Ceti. The three panels illustrate the field components in spherical coordinates (from top to bottom – radial, azimuthal, meridional). The magnetic field strength is expressed in gauss. The vertical ticks on top of the radial map show the phases of observations.*

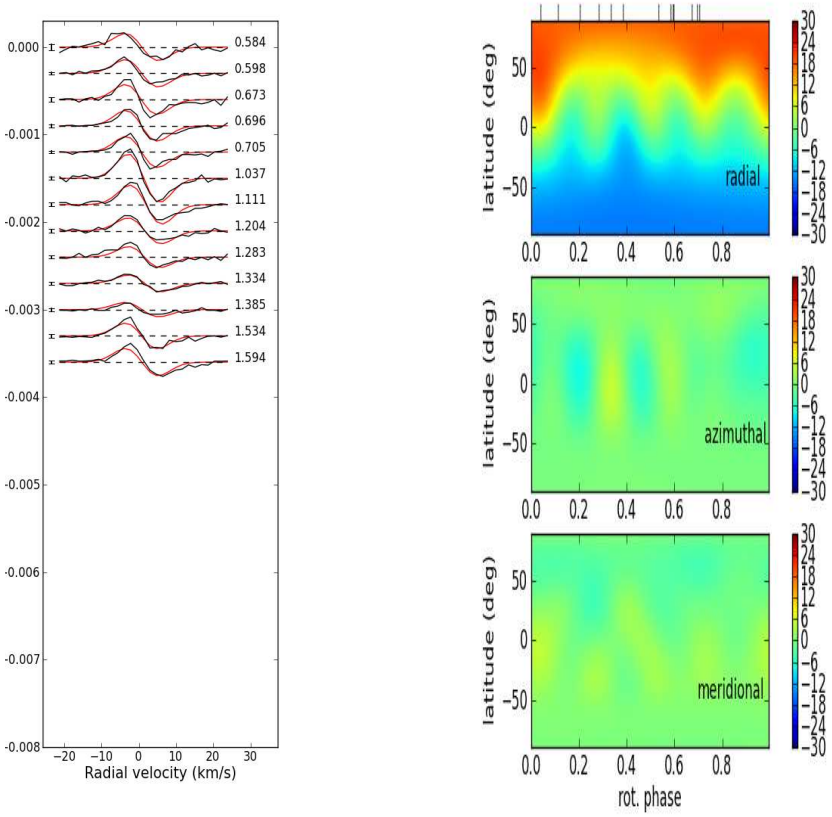

Figure 3.4: *Same as Fig. 3.3, for the period June 2011 – January 2012.*

netic field, which contains about 96 % of the reconstructed magnetic energy (Table 3.2). Most magnetic energy of the poloidal component is also stored in spherical harmonics modes with $\ell = 1$, with 83 % and 85 % (for the first and the second maps, respectively) of the reconstructed poloidal energy. This dominant contribution of low-order modes unveils a very simple topology, dominated by a dipolar configuration (the contribution of which is especially visible in the radial field component). The dipole is almost aligned on the spin axis, leading to a majority of the magnetic energy in modes with $m = 0$. The visible pole of the dipole features a positive field polarity and a polar field strength close to 20 G (see Table 3.2), in agreement with positive B_l values recorded for β Ceti. We also report in Table 3.2 a limited shift in rotational phase of the magnetic pole between the two maps. This apparent phase drift may be linked to the phase gap in the 2011/2012 dataset close to the positive pole (at phases 0.7 and above), which may have induced a less accurate longitudinal positioning of the pole.

Table 3.2: *Magnetic characteristics for the two magnetic maps of β Ceti. The fifth to ninth columns list the fraction of the large-scale magnetic energy reconstructed in the poloidal field component, the fraction of the poloidal magnetic energy stored in the dipolar ($l = 1$), quadrupolar ($l = 2$) and octopolar ($l = 3$) components, and the fraction of the energy stored in the axisymmetric component ($m = 0$).*

Epoch	rotational phase of maximum field strength	latitude of maximum field strength	magnetic dipole strength	pol. comp. (% tot)	dipole comp. (% pol)	quad. comp. (% pol)	oct. comp. (% pol)	axi. comp. (% tot)
2010	0.1	52°	20.5 G	96.7	83.2	20.8	6.2	77.1
2011/2012	0.0	50°	20.6 G	96.5	85.4	11.3	4.0	74.4

To check the good consistency of both magnetic topologies again, we computed another ZDI map (not shown here) combining all the data from June 2010 to January 2012. This global magnetic model is obtained with a χ^2 of 2.6, slightly larger than the χ^2 of the two separate maps. If the slightly worse Stokes V fit suggests a (limited) temporal evolution of the field structure, the resulting topology still agrees with both topologies obtained from individual subsets, which indicates that the temporal changes have left the dipole mostly untouched and are more likely related to smaller-scale features of the magnetic geometry.

3.1.4 *Mass, evolutionary status and surface abundances*

The position of β Ceti in the Hertzsprung-Russell diagram is shown in Fig. 3.5. We adopt the effective temperature of 4797 K from Massarotti et al. (2008) and the luminosity is computed using the stellar parallax from the New Reduction Hipparcos catalog by van Leeuwen (2007), the V magnitude from 1997 Hipparcos catalog, and the bolometric correction from Flower (1996; $BC = -0.403$); the error bar on luminosity reflects only the uncertainty on the parallax. The corresponding stellar radius obtained with the Stefan-Boltzmann law is 18 $R_\odot$.

We infer a mass of 3.5 $M_\odot$ based on the standard evolution tracks at solar metallicity from Lagarde et al. (2012), which are plotted in Fig. 3.5. According to our models, the main sequence progenitor of β Ceti was a late B-type star. Our values for the radius and mass are compatible with those found in the literature ($15-17$ $R_\odot$ and $2.8-3.5$ $M_\odot$, Jordan & Montesinos 1991, Maggio et al. 1998, Schröder et al. 1998, Gondoin 1999, Allende Prieto & Lambert 1999, Massarotti et al. 2008, Berio et al. 2011).

As seen from its position in the HRD in Fig. 3.5, β Ceti could presently either be at the base of the red giant branch or be undergoing core helium-burning. The latest option is actually strongly favored because of the much longer duration of the central helium-burning phase. In addition, the carbon isotopic ratio $^{12}C/^{13}C = 19 \pm 2$ (Luck & Challener 1995, Tomkin et al. 1975) and the Li abundance $N(Li) = 0.01$ (Luck & Challener 1995) derived for β Ceti indicate that this star has already fully undergone the first dredge-up. Indeed as can be seen in Table 3.3 where we give these quantities for standard and rotating 3.5 $M_\odot$ models at the luminosity and effective temperature of β Ceti both for the first RGB ascent and helium-burning options, the observational data are in excellent agreement with the theoretical post-dredge-up

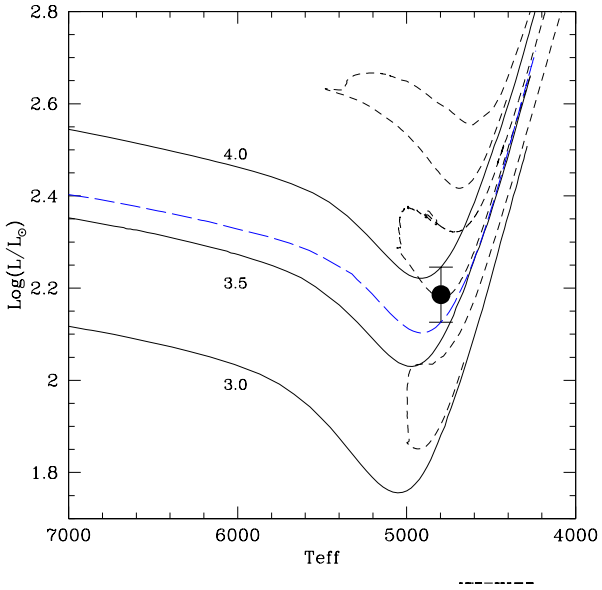

Figure 3.5: *Position of β Ceti in the Hertzsprung-Russel diagram using the effective temperature by Massarotti et al. (2008) and the luminosity derived from Hipparcos data (see text for details). Standard evolution tracks at solar metallicity by Charbonnel & Lagarde (2010) are shown in black for different initial masses as indicated by labels, with solid and short dashed lines indicating the phases of evolution before and after ignition of central helium-burning, respectively. The blue long dashed line is for the* 3.5 $M_{\odot}$ *rotating model (see text).*

predictions for the surface carbon isotopic ratio and lithium abundance of the 3.5 $M_{\odot}$, $Z_{\odot}$ rotating model shown in Fig. 3.5. Clearly, first ascent is excluded by the observed carbon isotopic ratio since at this position the first dredge-up is still going on, while it is fully completed when the star undergoes central helium-burning.

The 3.5 $M_{\odot}$ rotating model was computed with the same input physics and assumptions as Lagarde et al. (2012). In particular, initial velocity on the zero age main sequence is chosen equal to 45 % of the critical velocity, which corresponds to the mean value of the observed velocity distribution for cluster and field B type stars (Huang et al. 2010). At the location of β Ceti (helium-burning), the theoretical surface rotation velocity of the model is 6 km/s, in agreement with the observed $v \sin i$ for this star, although it corresponds to a rotational period of 160 days, i.e. slightly lower than the

value we derived through ZDI.

Table 3.3: *Theoretical predictions for surface Li abundance and carbon isotopic ratio at the luminosity and effective temperature of β Ceti on the first ascent of the red giant branch and on the central helium-burning phase in the 3.5 $M_{\odot}$ standard and rotating models for two initial rotation velocities (50 and 140 km/s). These numbers have to be compared with the observational values for β Ceti, namely N(Li)= 0.01 and $^{12}C/^{13}C = 19 \pm 2$ (see text for references and details).*

	N(Li) RGB	N(Li) He-burning	$^{12}C/^{13}C$ RGB	$^{12}C/^{13}C$ He-burning
standard	1.75	1.27	67	20.6
rotation (50)	1.58	1.12	61	20.6
rotation (140)	0.53	0.007	38	18.32

3.1.5 *Discussion*

The detection of a magnetic field on β Ceti (with a longitudinal strength of about 8 gauss) was first reported by Aurière et al. (2009 a). We present here our extended work for this star. Using spectropolarimetric data, we derived two magnetic maps of β Ceti. We reconstructed the surface magnetic field topology of the star for two sets of observations (June 2010 – December 2010 and June 2011 – January 2012), and our model suggests that the photospheric magnetic geometry is mostly stable and dominated by a simple dipole. Smaller scale features of the surface field topology are simply out of reach of the ZDI technique, because of its low spatial resolution at small $v \sin i$ values (Petit et al. 2005). The sharp line profiles also prevented us from applying the classical Doppler Imaging method to our set of Stokes I LSD profiles for reconstructing the brightness map associated with the magnetic topology, as previously done for giants rotating faster, e.g. Petit et al. (2004 a). In such a situation, the analysis of activity indicators is a useful complementary piece of information to partially reveal the presence and phase distribution of smaller magnetic elements. For β Ceti, it is clear from Fig. 3.1 that the variations in the longitudinal magnetic field B_l and chromospheric indicators correlate rather well, giving further support to the hypothesis of a field distribution limited to a very simple geometry.

The chromospheric activity of β Ceti is at the level observed on giant stars with $P_{rot} \approx 80\ d$ (Young et al. 1989), while the B_l maximum value of 8 G is typical of G and K giants with periods shorter than about 100 days (Aurière et al., in preparation). With a much longer estimated period of 215 days, β Ceti exhibits an abnormally high activity level, at least if we bear in mind the simple picture of a global dynamo efficiency that increases with the surface rotation rate. We also note that the simple field topology reconstructed from our observations is clearly different from the field geometry previously obtained for active giants rotating faster because of its simple structure and because of the lack of any significant toroidal component (Petit et al. 2004 a, Konstantinova et al. 2008 a). Another clear difference with more rapid rotators is the absence of any measurable surface differential rotation. The shear levels reported for other evolved objects are able to deeply modify field topologies within a few weeks (Petit et al. 2004 a), while β Ceti seems to keep a mostly constant field geometry over several years.

Since the magnetic behavior of β Ceti seems to be partly at odds with the global dynamo framework, we propose to explore the alternate option of a fossil magnetic field that may be inherited from the stable field of an *Ap* star, considering that the mass estimated for β Ceti (3.5 $M_{\odot}$) corresponds to a late-B/early-A star on the main sequence. This hypothesis was already proposed for EK Eridani (Aurière et al. 2008, 2011), another abnormally active cool giant sharing with β Ceti a magnetic topology almost purely poloidal and dominated by a dipole (in the relevant inclination range). Assuming that this fossil field is buried in the radiative zone, one may question if it could permeate the deep convective zone of a red giant, up to the photosphere. A similar situation has been simulated in the case of a 1 $M_{\odot}$ on the main sequence, for which the convective envelope occupies about 30 % of the radius. Strugarek et al. (2011 a, b) show that for an aligned or an inclined magnetic dipole, the magnetic field is able to expand from the radiative interior to the convective envelope.

The simple field topology of β Ceti is reminiscent of the mainly dipolar field configurations observed on main sequence Ap/Bp stars (Lüftinger et al. 2010). Following the fossil field hypothesis further, we can derive a rough estimate of the surface field strength of the main sequence progenitor of β Ceti. From our 3.5 $M_{\odot}$ model, we find that the radius of β Ceti must have been $R(zams) = 2.01\ R_{\odot}$ when the star arrived on the zero age main sequence. Assuming that the field measured for β Ceti simply differs from the main sequence field by the dilution effect of its larger radius, we can use the simple formula of Stepień (1993) for estimating the magnetic dipole strength of its main sequence parent star – $B(MS) = B[R/R(MS)]^2$, where B and R are the present dipole strength and radius of the star and $B(MS)$

and $R(MS)$ are the dipole strength and radius on the main sequence. In the hypothesis of conservation of magnetic flux, we derive a magnetic dipole strength of $B(MS) \approx 1650\ G$ on the main sequence, which is consistent with typical field strength measured on *Ap* stars (Landstreet & Mathys 2000, Aurière et al. 2007).

In the assumption of β Ceti being a descendant of an *Ap* star, we finally computed an evolutionary model of slow rotator with magnetic braking after the turnoff. For $V_{init} = 50\ km/s$, we did not find any difference for Li abundance or $^{12}C/^{13}C$ using models with and without magnetic braking after the turnoff. The numbers presented in Table 3.3 are therefore still relevant under this assumption, leaving our conclusions unchanged about the evolutionary state of β Ceti.

3.2 *EK Eri*

EK Eri (HR 1362, HD 27536) is a slowly rotating active $G8III-IV$ giant. It is suspected of being a descendant of a strongly magnetic *Ap* star by Stepień (1993) and Strassmeier et al. (1999). The photometric period of the star is about 300 d according to different authors – $309.6 \pm 1.5\ d$ by Strassmeier & Hall (1988); 330 d by Derman et al. (1989); $335.0 \pm 0.1\ d$ by Strassmeier et al. (1990 b); $306.9 \pm 0.4\ d$ by Strassmeier et al. (1999), but also split the data into two sets, which might represent two different spot cycles with photometric periods of $311 \pm 5\ d$ and $294 \pm 2\ d$; $308.8 \pm 2.5\ d$ by Dall et al. (2010, hereafter DBSS10) and they also suggest a conceptual model with two large low-latitude spots covered areas approximately 180° apart on a star viewed equator-on, so the rotation period is twice the photometric period.

The position of EK Eri in the HR diagram is determined by Aurière et al. (2008) and is shown in Fig. 3.6. The evolutionary tracks are computed for standard, non-rotating models for different stellar masses with solar metallicity. The model shows that EK Eri has an initial mass of $2.0 \pm 0.1\ M_{\odot}$ and a radius of 4.68 $R_{\odot}$. The star is located at the end of the Hertzsprung gap and enters the first dredge-up phase.

3.2.1 *Observations and data reduction*

The 28 observations of EK Eri were obtained between September 20, 2007, and March 21, 2011, with the spectropolarimeter *Narval* (Aurière et al. 2008; Chapter 2).

Least Square Deconvolution method (Donati et al. 1997) was applied to all observations with a line mask calculated for an effective temperature

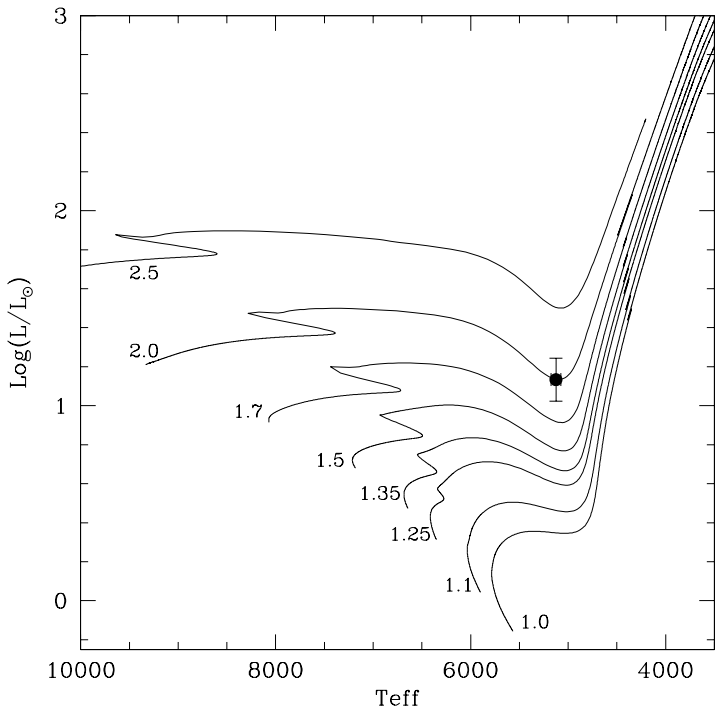

Figure 3.6: *The position of EK Eri in the HR diagram by Aurière et al. (2008).*

of 5250 K, $\log g = 3.5$ and a microturbulence of 2.0 km/s, consistent with physical parameters reported by DBSS10. This method enabled us to average about 11 000 spectral lines and to derive Stokes V profiles with a S/N that improved by a factor of about 40 in comparison with that for single lines. The longitudinal magnetic field B_l in Gauss was computed, using the first-order moment method (Rees & Semel 1979, Donati et al. 1997). Also, S-index (defined from the Mount Wilson survey, Duncan et al. 1991) was computed for the chromospheric CaII K&H line cores. The procedure was first calibrated on the main sequence solar-type stars of Wright et al. (2004), then it was added 0.03 to the index to fit measurements of 5 giant stars observed by Duncan et al. (1991) and Young et al. (1989). The relative intensity with respect to the continuum (R_c) of the CaII IR triplet (854.2 nm component) and $H\alpha$ were also measured. The RV of EK Eri was measured from the LSD Stokes I profiles using a gaussian fit. All the data are summarized in Table 3.4.

Table 3.4: *Measured B_l values and their uncertainties, activity indicators and radial velocity for EK Eri for the photometric phase, based on the ephemeris of DBSS10.*

Date	HJD 2450000+	Phot. Phase	S-index	CaII IR	$H\alpha$	B_l [G]	σ [G]	RV $[km/s]$
20 Sep 07	4364.69	0.212	0.501	0.319	0.226	-98.6	1.0	7.118
12 Nov 07	4417.44	0.383	0.457	0.291	0.233	-21.1	0.7	7.047
13 Nov 07	4418.45	0.386	0.456	0.297	0.233	-21.4	0.9	7.053
19 Jan 08	4485.31	0.603	0.470	0.303	0.230	-28.9	1.2	7.096
20 Jan 08	4486.38	0.606	0.463	0.295	0.227	-31.6	0.9	7.110
06 Feb 08	4503.35	0.661	0.469	0.302	0.234	-45.6	0.8	7.111
03 Apr 08	4560.31	0.845	0.513	0.339	0.250	-62.7	1.2	7.145
28 Aug 08	4707.68	0.323	0.502	0.331	0.251	-12.8	0.7	7.052
14 Sep 08	4724.60	0.378	0.511	0.338	0.262	-27.9	1.4	7.043
24 Sep 08	4734.57	0.410	0.510	0.341	0.270	-18.8	1.1	7.000
29 Sep 08	4739.71	0.426	0.506	0.338	0.264	-13.7	0.8	6.996
20 Dec 08	4821.37	0.691	0.543	0.365	0.266	-36.8	1.1	7.046
30 Jan 09	4862.35	0.824	0.588	0.390	0.291	-46.4	1.0	7.207
25 Feb 09	4888.31	0.908	0.573	0.369	0.270	-67.8	0.9	7.176
28 Sep 09	5103.62	0.605	0.602	0.423	0.286	-48.0	1.2	7.080
27 Oct 09	5132.57	0.699	0.576	0.396	0.280	-56.9	1.3	7.101
15 Jan 10	5212.44	0.957	0.547	0.339	0.254	-88.6	2.7	7.190
03 Feb 10	5231.32	0.018	0.566	0.354	0.259	-90.7	2.1	7.200
13 Feb 10	5241.29	0.051	0.575	0.363	0.263	-90.9	2.1	7.214
06 Mar 10	5262.30	0.119	0.548	0.353	0.258	-77.0	1.2	7.218
22 Mar 10	5278.32	0.171	0.533	0.348	0.260	-58.9	1.0	7.195
21 Sep 10	5461.62	0.764	0.598	0.381	0.278	-90.9	1.2	7.062
13 Oct 10	5483.64	0.836	0.565	0.370	0.262	-94.6	0.9	7.107
12 Nov 10	5513.55	0.932	0.571	0.365	0.264	-93.1	1.1	7.183
04 Dec 10	5535.36	0.003	0.576	0.359	0.270	-87.2	6.8	7.150
03 Jan 11	5565.28	0.100	0.585	0.374	0.268	-77.7	1.0	7.150
23 Jan 11	5585.44	0.165	0.589	0.436	0.272	-57.6	1.0	7.166
21 Mar 11	5642.31	0.350	0.574	0.403	0.277	-39.5	1.2	7.130

3.2.2 *Variations of* B_l

Table 3.4 and Fig. 3.7 show that B_l does not reverse its polarity during the 4 observed seasons. Fig. 3.7 displays B_l measurements with respect to HJD. Vertical marks at the top of Fig. 3.7 indicate the times of photometric minima according to the ephemeris of DBSS10, i.e. when the cool spot is centred on the visible hemisphere of the star (phase 0.0). We see that the unsigned B_l is approximately at maximum at these dates. In the third season (2009-2010), which is well-centred on the spot passage, $|B_l|$ is confirmed to peak at phase 0. This trend is clearly visible in Fig. 3.8 (upper panel) which contains the same data as in Fig. 3.7, but folded with respect to the photometric ephemeris (DBSS10, $P = 308.8\ d$, $HJD_0 = 2453372.679$). This is consistent with a picture, in which the center of the dark spot of EK Eri coincides with the strongest $|B_l|$. DBSS10 suggested that the dark spot could correspond to the pole of the remnant of the dipole of an evolved Ap star.

Since B_l does not reverse its polarity, in this scenario, only one pole of the putative dipole is observed, and the rotational period would then be equal to the photometric period, and not its double, contrary to the suggestion of DBSS10.

Fig. 3.8 also shows that the (year to year) scatter of the points is significant with respect to the error bars. It could be due to an incorrect period, or in changes in activity level, as observed in photometry. In the scenario where the rotational period is the photometric one, this would show that an oblique rotator model (ORM, Stibbs 1950) alone could not explain the variations of B_l. Some dynamo process would therefore need to be invoked.

3.2.3 *Variations of activity indicators and* RV

Fig. 3.8 (lower panels) shows the variations of the activity indicators versus photometric phase. Though the points are scattered, their lower envelope follows the variations of $|B_l|$ with respect to phase, with a maximum near phase 0, and a minimum near phase 0.5. This trend is more visible for CaII (S-index and IR lines) than for $H\alpha$. Some points are significantly above the lower contours of the plots and they are discussed below. In particular, during the 2010-2011 season, the modulation of activity indicators disappears (this season is highlighted in red in Fig. 3.8). Error bars are computed for each measurement of CaII IR and $H\alpha$ measurement. They are generally of order 0.001, and never reach 0.01. As to S-index, an internal error of 0.007 is estimated for the whole sample in agreement with the day-to-day scatter (Table 3.4, 12/13 November 2007, 19/20 January 2008). These error bars for activity indicators are smaller than the symbols used in Fig. 3.8 (lower

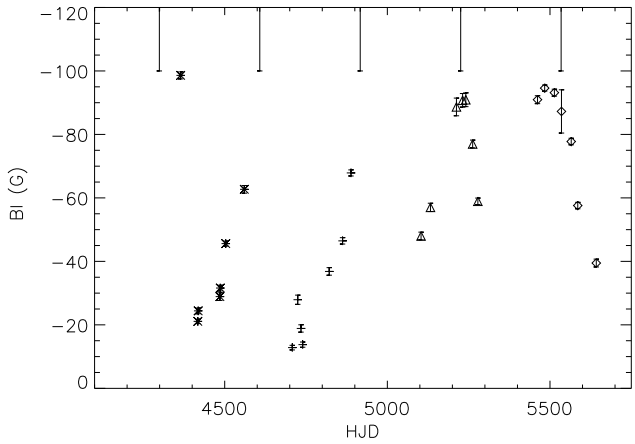

Figure 3.7: *Variations of the longitudinal magnetic field B_l in G versus HJD (minus 2450000). Different symbols represent different observing seasons: stars: 2007-2008, crosses: 2008-2009, triangles: 2009-2010, diamonds: 2010-2011. Vertical marks at the top of the figure indicate the times of photometric minima according to the ephemeris of DBSS10.*

panel) and are therefore not plotted there.

Fig. 3.9 shows the variations of RV versus phase. The long term stability of *Narval* is about 30 m/s (Aurière et al. 2009 b). RV is found to vary with photometric phase, as already reported by Dall et al. (2005, DBSS10). There is some scatter near phase 0 and a delay of the RV maximum by about 0.1 cycles with respect to B_l. This trend strongly suggests that the cool/magnetic spot is responsible for the RV variations (Dall et al. 2005, DBSS10). Because of the small $v \sin i$ of EK Eri, classical Doppler imaging is not possible for this star. On the other hand, a small $v \sin i$ does not prevent mapping using Zeeman-Doppler imaging (Petit et al. 2008).

3.2.4 *Discrepant points in B_l and activity indicators*

Fig. 3.8 shows that the seasonal variations of B_l and the activity indicators generally vary coherently with photometric phase, and that there is seasonal scatter greater than the measurement error bars. In addition there are some outstanding deviations from the mean variation.

As far as the B_l measurements are concerned, the observations of 20 September 2007 (the first one, which is our "discovery observation"), as well as those obtained on 21 September and 13 October 2010 present outstanding

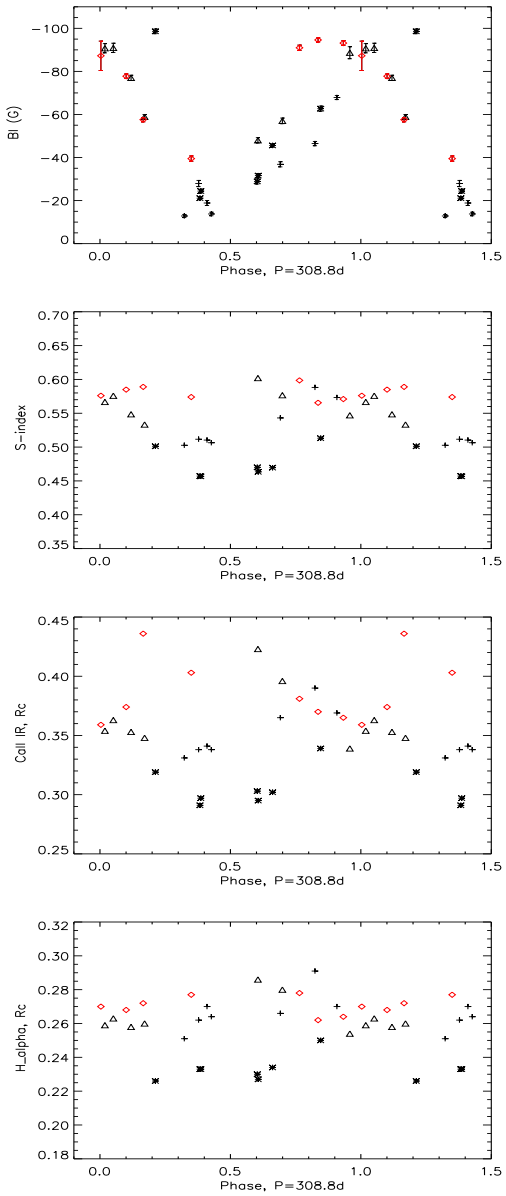

Figure 3.8: *Variations of the longitudinal magnetic field B_l (upper panel) and of the activity indicators (lower panels), with photometric phase. The lower panels, from top to bottom, show: S-index, R_c for CaII IR lines and Hα. Different symbols represent different observing seasons: stars for 2007-2008, crosses for 2008-2009, triangles for 2009-2010, diamonds for 2010-2011; the 2010-2011 season is shown in red.*

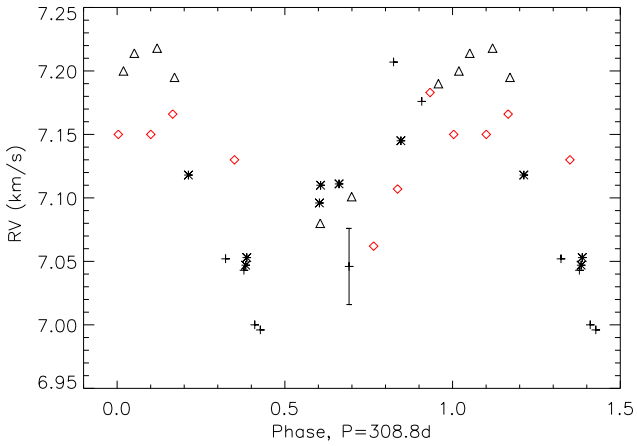

Figure 3.9: *Variations of radial velocity with photometric phase. An error bar of* 30 m/s *is indicated. Different symbols represent different observing seasons: stars for 2007-2008, crosses for 2008-2009, trianglesfor 2009-2010, diamonds for 2010-2011; the 2010-2011 season is shown in red.*

deviations from the general phase variations. On 20 September 2007, the S-index and other activity indicators do not deviate from the general phase variation. On the other hand, for the 2 first autumn 2010 observations, both B_l and activity indicators are stronger than expected at their respective phases.

Remarkably, in the 2010-2011 season, the modulation of activity indicators disappears: this season is highlighted in red in Fig. 3.8. While B_l values approach the typical level and modulation at the end of 2010, the intensity of the activity indicators remains high. Also, on some occasions, in particular 28 September 2009, the activity indicators are surprisingly high, while the B_l value is quite normal with respect to the phase. Looking closely at the data, we find that we may have a problem of normalization of the continuum for this date, which can affect the measurements of activity indicators, but not B_l (as the Stokes V measurement is a differential measurement). To further investigate this potential background problem, we have computed the CaII H emission index used by Morgenthaler et al. (2011 b, 2012). This method makes use of a synthetic spectrum from the POLLUX database (Palacios et al. 2010) to normalise the continuum. It was found to be very effective in the case of solar-type dwarfs, enabling those authors to reach internal errors of about 0.001 for chromospheric emission index measurements (Morgenthaler et al. 2011 b, 2012). However, in the case of EK Eri this method did not

allow us to reduce the deviations, and we present our S-index measurements in Table 3.4 and Fig. 3.8 as they are.

Of peculiar interest are the isolated enhancements of B_l, activity indicators or both. They may be associated with flares as observed in active giants (Konstantinova-Antova et al. 2000, 2005 a). In this case it would be the first time that simultaneous observations of magnetic field and activity indicators have been performed during flares in the stellar context. In the solar case, a simultaneous increase of magnetic field and $H\alpha$ has been observed (Lozitsky et al. 2000).

The outlying magnetic observations of September 2007 and autumn 2010 were found to increase dramatically the reduced χ^2 of our model fitting in Sec. 3.2.5. We will use only data between November 2007 and March 2010 (spanning about 3 rotations) for forthcoming magnetic analysis.

3.2.5 *Zeeman Doppler imaging*

In order to model our series of Stokes V line profiles and to reconstruct the surface magnetic geometry of the star, we have used the ZDI inversion method (Donati and Brown 1997, Donati et al. 2006 b) – the surface magnetic field is projected onto a spherical harmonics frame and the magnetic field is resolved into poloidal and toroidal components.

Because of the very slow rotation of EK Eri, its $v \sin i$ has been impossible to determine up to now due to the degeneracy between $v \sin i$ and macroturbulence (DBSS10). These authors consider that 0.8 km/s is a safe upper limit for $v \sin i$. In our models we used $v \sin i = 0.5$ km/s and found that varying this value did not significantly change our results.

We used a linear limb darkening coefficient equal to 0.75. We limited the spherical harmonics expansion to $\ell \leq 3$ since increasing this threshold do not significantly change the results.

3.2.6 *The rotational period of EK Eri*

Knowing the rotational period of EK Eri is essential to be able to perform ZDI. Photometric variations of EK Eri have been now monitored during more than 30 years and a period of 308.8 ± 2.5 d has been adopted (DBSS10) as well as an ephemeris. This period may have changed slightly during the span of the photometric observations (Strassmeier et al. 1999). DBSS10 argued that the rotational period could be equal to twice the photometric period, i.e. 617.6 ± 5 d.

To determine independently the rotational period of EK Eri, we have followed the approach of Petit et al. (2002), and calculated a set of magnetic

maps, assuming for each map a different value for the rotational period. We impose a constant entropy for all the images and calculate as a goodness-of-fit parameter the reduced χ^2 (χ^2_r hereafter) by comparing the set of synthetic Stokes V profiles produced by ZDI to the observed time-series of Stokes V profiles. We then study the variations of χ^2_r over the range of rotation periods, to determine the period value producing the best magnetic model (identified by the lowest value of χ^2_r). Here we scanned 400 values of the period between 200 and 700 days, a range which encompasses the photometric and rotational periods proposed for EK Eri by DBSS10. Our periodograms show a favoured period near 311 days. However the minimum χ^2_r value is high (about 25), notwithstanding that we limited our observational sample to the timespan November 2007 – March 2010 in order to avoid the effect of the strong deviations observed on 20 September 2007 and during the autumn of 2010. We therefore introduced a possible differential rotation (Petit et al. 2002). Ultimately, we could not improve the results and deduced a negligible differential rotation for EK Eri. We also considered that our approximate line profile model might be the source of the high χ^2_r: the current local line profile used in our model is a gaussian function. In an attempt to improve the fit of the line profile, we introduced a Lorentzian function and some asymmetry, but we still could not reduce significantly the χ^2_r. Ultimately, we consider that the relatively poor detailed fit to the Stokes V profiles resulting from our best-fit model is mainly due to the seasonal scatter of the magnetic field strength.

Fig. 3.10 shows the periodogram obtained for the whole data set between November 2007 and March 2010, assuming a rotational axis inclination of EK Eri of $i = 60°$ and truncating the expansion at $\ell = 3$. For rotational periods of 311.5 d, 308.8 d and 625 d, we obtain respectively values for χ^2_r of 25 (our minimum), 25.3 and 38.2. The 600-day period suggested by DBSS10 is therefore eliminated both by our periodogram analysis and by the fact that their scenario to explain $P_{rot} = 2P_{phot}$ is not supported by the B_l variations. Since we found that phase 0.0 of the ephemeris of DBSS10 corresponds to approximately the center of the magnetic spot which dominates the magnetic map (see below), we decided to use the photometric period of 308.8 days (and $HJD_0 = 2453372.679$) for our analysis of the magnetic topology.

Fig. 3.11 presents the fit of our best model to the observed Stokes V LSD profiles, for $P_{rot} = 308.8$ d, and $i = 60°$.

3.2.7 *Possible topologies of the surface magnetic field*

In the two previous subsections, we have presented the models and the parameters employed to infer the magnetic topology of EK Eri. Because $v \sin i$

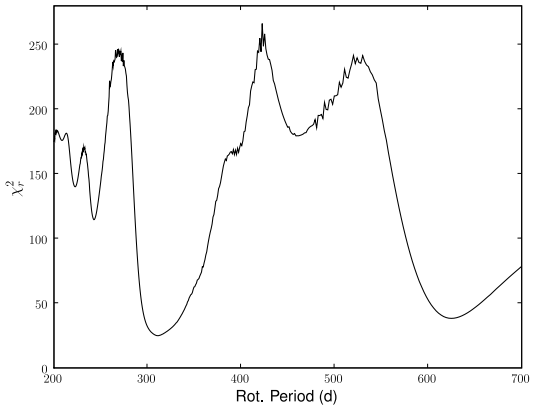

Figure 3.10: *Periodogram obtained using the entire data set between November 2007 and March 2010.*

cannot be determined precisely, the value of the inclination i is also only weakly constrained. This is our main remaining uncertain parameter which we have attempted to constrain as part of the ZDI reconstruction. We have therefore fit our Stokes V data with our models and i varying from 85° to 40°.

For all models we find that the poloidal component contains more than 98 % of the reconstructed magnetic energy. When i decreases, we find the ZDI procedure to provide us with a better magnetic model, in the sense that the total information content of the reconstructed magnetic geometry decreases (we follow here the maximum entropy criterion, Donati 2001, explicited in Morin et al. 2008 b). For high inclination, $i > 80°$, the topology is dominated by a quadrupolar configuration. In this case, the two rotation poles correspond to positive polarity while there is a nearly equatorial band, with a single enormous magnetic spot, both of negative polarity. The magnetic spot corresponds to the phase of the dark (and therefore presumably cool) photometric spot to better than 0.1 cycles.

For $i < 80°$, the dipole component dominates and corresponds to about 90 % of the magnetic energy at about $i = 60°$. Fig. 3.12 shows the corresponding ZDI map. This map also features a strong magnetic spot of negative polarity, corresponding to the negative pole of the magnetic dipole. Again the magnetic maximum corresponds in phase to the photometric spot. The characteristics of this model are compatible with the scenario of Aurière et al. (2008) and DBSS10, in which the magnetic/photometric spot would correspond to the remnant of a magnetic pole of the *Ap* star progenitor of

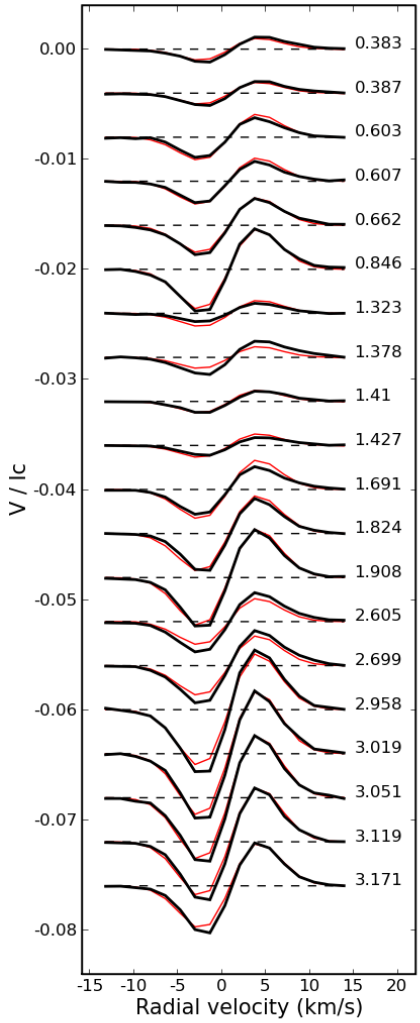

Figure 3.11: *Fit of our best-fit model (for $P_{rot} = 308.8$ d, $i = 60°$) (thin red curves) to the Stokes V LSD profiles (thick black curves), after correction of the mean radial velocity of the star. Rotational phases (according to the ephemeris of DBSS10) are indicated.*

EK Eri.

Given the lower information content (i.e. higher entropy) associated with the predominantly dipolar configuration, we consider this model to be better, or at least more likely, than the quadrupolar model. In addition, this model suggests an obvious physical interpretation: that the corresponding magnetic pole is at the position of the photometric spot of EK Eri, and that the dipole could be the remnant of the magnetic field of an *Ap* star progenitor. Both Fig. 3.11 – presenting the variations of the Stokes V profiles – and Fig. 3.8 (upper panel) – presenting the variations of B_l – show that the magnetic field varies on a large scale and does not experience a sudden drop when the "magnetic spot" is not visible, as it would do in the case of a very localized strong magnetic spot: a dipolar configuration naturally explains the observed behavior. However, even if the quadrupolar configuration is less favoured by our modeling procedure and if this topology does not appeal for an obvious formation scenario, we cannot rule it out as a possible solution. As explained in Sec. 3.2.4, the present ZDI study was made using only the 20 spectra corresponding to about 3 rotations, between November 2007 and March 2010, to avoid epochs when activity appeared to deviate significantly form the mean variation. However, the main results as described above would be the same if we employed the entire data set, except that the χ^2_r would have been significantly worse.

From the dipolar model (corresponding to $i = 60°$ and Fig. 3.12) we can measure β (the angle between rotational and magnetic axes of the dipole component) and the dipole strength (since the dipolar component dominates, the strength of the dipole corresponds to about the maximum magnetic field measured on our map) (following the equations in Stibbs 1950, Preston 1967): we find $\beta = 45°$, $B_d \sim 207$ G.

We have also fit our data with a model with a pure dipole, corresponding to spherical harmonic $\ell = 1$ (and assuming $i = 60°$). The goodness of fit is (naturally) worse than for the models described above, and the inferred dipole parameters are $\beta = 22°$, $B_d \sim 198$ G.

The magnetic maximum is measured to occur at phases 0.04 and 0.96, respectively, for the two ZDI models described above.

It could also be of interest to use the measurements of B_l from Sec. 3.2.2 (Table 3.4) to fit a dipolar oblique rotator model using the relations of Preston (1967) and reviewed by Aurière et al. (2007). In this case we find $\beta = 23°$ and dipole strength of 370 G (taking $i = 60°$ as suggested above).

The smaller value obtained for B_d from our ZDI models with respect to B_d inferred from the B_l variations is due in part to the fact that our ZDI models correspond to Stokes V signatures at phases near magnetic maximum that are weaker than those observed (Fig. 3.11).

Taking $i = 60°$, in the case of rigid rotation, using $R = 4.68\ R_\odot$ from the evolutionary model of Charbonnel & Lagarde (2010) used by Aurière et al. (2008), we get $v \sin i = 0.69\ km/s$.

3.2.8 *Discussion*

The evolution of a magnetic (2 $M_\odot$) *Ap* star from the main sequence to the red giant branch is characterized by a surface magnetic field, which is expected to weaken (as $1/R^2$ if conservation of magnetic flux is assumed) while the convective envelope deepens. The rotational period on the surface also lengthens as the star expands. For an *Ap* star progenitor of EK Eri, one can infer a magnetic field of several thousand gauss (Stepień 1993, Aurière et al. 2008). At the main sequence evolutionary stage, the magnetic field would be sufficient to suppress convection (e.g. discussion by Théado et al. 2005). At the present evolutionary stage of EK Eri we measure a large scale surface magnetic field dominated (for $i = 60°$) by a dipole of about 200 G strength, when the convective envelope of our 2 $M_\odot$ model contains $\sim 0.37\ M_\odot$ of the star's mass (Aurière et al. 2008). The outstanding magnetic activity properties of EK Eri are therefore the result of the interplay of the remaining magnetic field from one *Ap* star and deep convection. Such an interaction between a pre-existing magnetic field and thermal convection has been studied through numerical simulations mostly in the solar context (Hurlburt et al. 1996, Cattaneo et al. 2003, Proctor 2004, Thomson 2005, Strugarek et al. 2011 b) and in the cases of core convection (Featherstone et al. 2009). For example, the transition between regimes when the imposed magnetic field is strong (magnetoconvection) and when the magnetic field is weak (dynamo) is investigated (Cattaneo et al. 2003).

No differential rotation is inferred from our modeling (Sec. 3.2.6): this can be expected both from a strong (fossil) magnetic field and from a slow rotator. Fig. 3.11 shows that an average magnetic field can be defined during the 3 observed rotational periods used for modeling. Fig. 3.8 shows that significant deviations occur during that period of time, and some are even stronger before (20 September 2007) and afterward (21 September and 13 October 2010; see also Sec. 3.2.4). This shows that even if a magnetic dipole dominates the magnetic topology, we are not in the presence of a stable, large-scale magnetic field as in an *Ap* star. Fig. 3.11 also shows that it was not possible to perfectly fit our observations at phases near maximum magnetic strength. Therefore, the interplay of the remaining field and convection appears to induce some variable magnetic component.

Another striking difference between the magnetic spot of EK Eri and the magnetic pole of an *Ap* star, is that for an *Ap* star surface features ("spots")

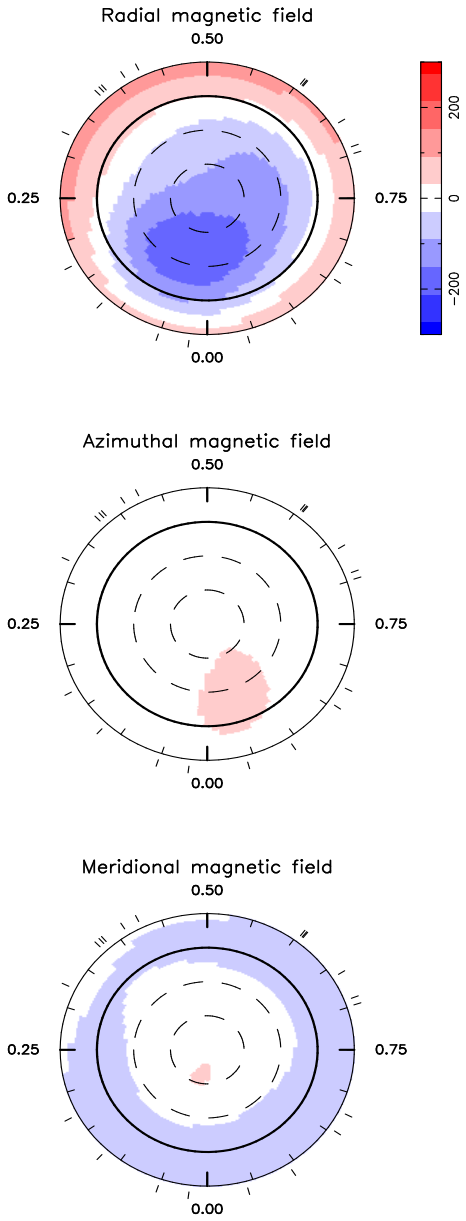

Figure 3.12: *Magnetic map of EK Eri for* $i = 60°$*. Each chart illustrates the field projection onto one axis of the spherical coordinate frame. The magnetic field strength is expressed in G. The star is shown in flattened polar projection down to latitudes of* $-30°$ *, with the equator depicted as a bold circle and parallels as dashed circles. Radial ticks around each chart indicate the observed rotational phases.*

correspond generally to chemical over-abundances of some elements, and are expected to be bright (Krticka et al. 2007, Lüftinger et al. 2010). In the case of EK Eri, the spot is dark and redder (and presumably cool), while the abundances are found to be similar to those of the Sun at all phases (DBSS10); the spot of EK Eri therefore appears to be a temperature spot, as observed in the late-type stars, where dynamo operates. As discussed by Aurière et al. (2008), the overabundances observed at the surface of an *Ap* star would have been erased by the deep mixing occuring during the first dredge-up, in which EK Eri is currently engaged. The differences between models for the magnetic poles of *Ap* stars and sunspots have been investigated (Shibahashi 2004).

This work shows that the magnetic variations of EK Eri are dominated by stellar rotation (i.e. rotational modulation of a dipole in our prefered scenario). The survival of a fossil dipole can explain the long term stability of the location of the dark spot, and magnetic cycles of varying photometric amplitude may be due to dynamo-like activity. Because of the very small $v \sin i$ of EK Eri, only large scale features of the surface magnetic field can be mapped with ZDI. However, the activity indicators are sensitive to all scales of magnetic regions. The observations of the 2010-2011 season show (Fig. 3.8) that while in September–October 2010 both the magnetic field and activity indicators were stronger than expected for that rotational phase, the magnetic field became "normal" at the beginning of 2011 while the values of the activity indicators remained high. Therefore the large scale magnetic component could be more stable than the small-scale field. In this context, it would be worthwhile to investigate if the possible magnetic cycles suggested by photometry (DBSS10) exist as well in the magnetic data. Studying the correlation between photometric amplitude and surface magnetic strength/topology of EK Eri would certainly help to understand the interplay of the dipole remnant and convection.

Chapter 4

The fast rotating V390 Aur

The $G8III$ star V390 Aur = HD33798 is already known for its magnetic activity. A modulation of the photometric light curve due to spots is observed by Spurr & Hoff (1987) and a period of 9.825 days that is considered the rotational period of the star is determined by Hooten & Hall (1990). It has been classified as a chromospherically active giant by Fekel & Marshall (1991) on the basis of its CaII K emission and fast rotation ($v \sin i = 29\ km/s$). Later, enhanced X-ray emission (Hünsch et al. 1998, Gondoin 1999, Gondoin 2003) and optical flares (Konstantinova-Antova et al. 2000, 2005 a) were detected for this star. Recently, Konstantinova-Antova et al. (2008 b) reported direct detection of magnetic field using the spectropolarimeter *Narval* at the 2-m Telescope Bernard Lyot at Pic du Midi Observatory, France.

According to the literature, V390 Aur has a mass of about $1.8-2\ M_{\odot}$ and is evolving along the base of the red giant branch (Gondoin 2003, Konstantinova-Antova et al. 2009). It is the primary of a wide multiple physical system, ADS 3812, and it was shown that the giant could be considered as effectively single with respect to its activity, i.e. synchronization plays no role in its fast rotation and activity (Konstantinova-Antova et al. 2008 b).

4.1 *Observations and data processing*

The observations of V390 Aur were performed at the 2-m Télescope Bernard Lyot (TBL) of Pic du Midi Observatory with the spectropolarimeter *Narval* (Aurière 2003, Chapter 2).

Thirteen observations were obtained in the period 14 – 30 September 2008 (Table 4.1). The extraction of the spectra was performed using Libre-ESpRIT (Donati et al. 1997). Then, *LSD* (Donati et al. 1997) was applied with a

mask calculated for an effective temperature of 5000 K, $\log g = 3.0$ and a microturbulence of 2.0 km/s, consistent with physical parameters given by Gondoin (2003). For the case of V390 Aur, the method enabled us to average about 12 300 lines and to get Stokes I and Stokes V profiles with a significantly improved signal-to-noise ratio (S/N). A significant Zeeman Stokes V signal was detected for each observation. The null spectrum given by the standard procedure (Donati et al. 1997) was also examined, which showed no signal. We then computed the longitudinal magnetic field B_l in G, using the first-order moment method (Donati et al. 1997, Rees and Semel 1979). To determine B_l values, we integrated the LSD profiles between -17 and $+66$ km/s, which reduced the significant blending by the profiles of the faint stellar companion of V390 Aur (which is a SB2 star, Konstantinova-Antova et al. 2008 b). These profiles present in some of our spectra.

The activity of the star for the same period has been monitored with measurements of the relative intensity regarding the continuum (R_c) for the line activity indicators CaII IR 854.2 nm and $H\alpha$. For CaII K the relative intensity of the emission core $I/I(395\ nm)$ is measured. The S/N is greater than 50 for the CaII K&H emission cores and greater than 500 for the rest of the spectral lines mentioned above. The B_l and activity indicators behaviour is presented in Table 4.1 and in Fig. 4.1.

In addition, we performed ZDI (Donati et al. 2006 a) for V390 Aur, using all these observations. In spite of a large $v \sin i$ value, that makes V390 Aur a possible target for classical Doppler Imaging, we do not present here a photospheric map of brightness inhomogeneities, because of the occasional Stokes I contamination by the double-lined stellar system associated with the giant. Without any accurate orbital parameters available for this system, no clean removal of its Stokes I signatures can be performed following the approach of Donati (1999). The primary is the only detected contributor to the Stokes V line profiles, so that other components of the system do not affect the magnetic map reconstruction.

4.2 *Zeeman Doppler Imaging*

In order to reconstruct the magnetic field geometry of V390 Aur based on modelling of the rotational modulation of the Stokes V profiles, it was applied the ZDI inversion method (Donati & Brown 1997, Donati et al. 2006 b), which enables the split of the magnetic field in poloidal and toroidal components.

To calculate the rotation phases of the observations, we took as rotational period the photometric one of 9.825 d, $v \sin i = 29$ km/s, inclination angle

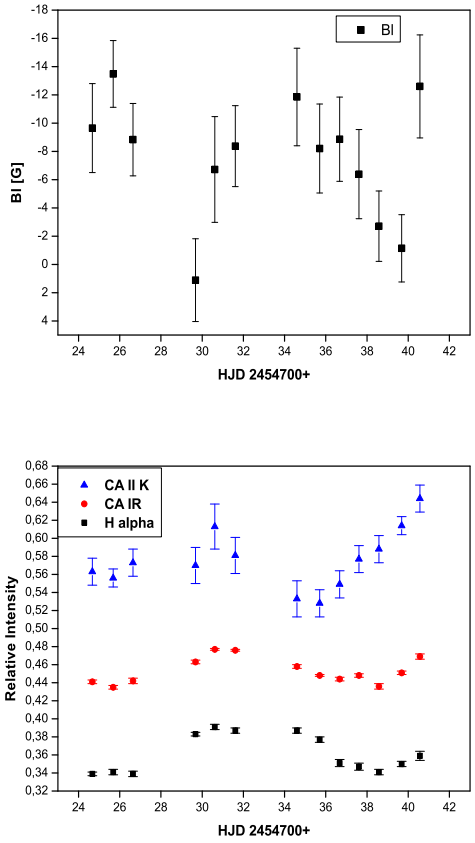

Figure 4.1: *Variability of B_l (top), CaII K, CaII IR 854.2 nm and Hα (bottom) for V390 Aur.*

Table 4.1: *Data for activity indicators, B_l values and their uncertainties. Phase is for 9.825 d photometric period, considered as the rotational period of V390 Aur.*

Date	Phase	CaII K	$H\alpha$	CaII IR	B_l [G]	σ [G]
14 Sep 08	0.00	0.56	0.339	0.441	-10	3
15 Sep 08	0.10	0.55	0.341	0.435	-13	2
16 Sep 08	0.20	0.57	0.339	0.442	-9	3
19 Sep 08	0.51	0.57	0.383	0.463	1	3
20 Sep 08	0.60	0.61	0.391	0.477	-7	4
21 Sep 08	0.71	0.58	0.387	0.476	-8	3
24 Sep 08	0.01	0.53	0.387	0.458	-12	3
25 Sep 08	0.12	0.52	0.377	0.448	-8	3
26 Sep 08	0.22	0.55	0.351	0.444	-9	3
27 Sep 08	0.32	0.58	0.347	0.448	-6	3
28 Sep 08	0.42	0.59	0.341	0.436	-3	2
29 Sep 08	0.53	0.61	0.350	0.451	-1	2
30 Sep 08	0.62	0.64	0.359	0.469	-13	4

of the axis of rotation 56° (Konstantinova-Antova et al. 2008 b) and a limb darkening coefficient of 0.75. We also assumed a constant radial velocity of 23.4 km/s. Taking into account the complex structure of the Stokes V profiles, we extend the order of the spherical harmonics modes to $l \leq 25$, since no improvement in the fit to the data is achieved by increasing further the maximum allowed value for l.

Prior to reconstructing the final magnetic map, we have estimated the surface differential rotation of V390 Aur, using the method proposed by Petit et al. (2002). We assume a simple latitude dependence of the rotational shear in the form $\Omega(l) = \Omega_{eq} - \Delta\Omega \sin^2 l$, where $\Omega(l)$ is the rotation rate at latitude l, Ω_{eq} the rotation rate of the equator and $\Delta\Omega$ the difference in rotation rate between the polar region and the equator. The best magnetic model is achieved for differenial rotation parameters equal to $\Omega_{eq} = 0.652 \pm 0.002\, rad/d$ and $\Delta\Omega = 0.048 \pm 0.007\, rad/d$, with a reduced χ^2 equal to 1. The value of the photometric period lies between the equatorial and polar periods estimated here and corresponds to the rotation period obtained around a latitude of 30°, which is the latitude seen orthogonally by the observer, assuming an inclination angle of 56°.

The result of our modelling is presented in Fig. 4.2. In this figure, the

upper pannel displays the Stokes V profiles fitted with the model, and the three other panels show the surface magnetic field distribution for V390 Aur as maps of the radial, azimuthal and meridional components of the magnetic field.

Our map of the radial magnetic field reveals a strong polar spot of positive polarity and several groups of spots of negative polarity situated at lower latitudes. The azimuthal component of the field presents a middle to high latitude belt. We reconstruct about 80 % of the surface magnetic energy in the poloidal magnetic component, where the dipole structure dominates.

4.3 B_l *and activity indicators*

Figure 4.3, upper panel, shows the variations of B_l with respect to the photometric phase already used in the ZDI work. The folding appears good, with the unsigned $|B_l|$ being maximum at phase 0 and minimum at phase 0.5.

The activity indicators vary smoothly (Fig. 4.1). The indicators CaII 854.2 and $H\alpha$ are synchronous, whereas CaII K deviates slightly. Though they appear to vary in opposition with $|B_l|$, folding of the data does not fit to the photometric period, but suggests a longer period (Fig. 4.3). We performed a period search analysis for the activity indicators CaII K, CaII IR and $H\alpha$. We applied several period search techniques: Lomb-Scargle (Lomb 1976, Scargle 1982), Lafler-Kinnman (Lafler & Kinman 1965), Bloomfield (Bloomfield 2000), CLEANest (Foster 1995) and Deeming (Deeming 1975). Some of them gave indications of periods longer than the photometric one and mainly in the interval 10-15 days, but with an accuracy of 2-3 days due to the short dataset we have.

It might be a tendency for longer periods of CaII IR and $H\alpha$, compared to CaII K, but as mentioned above, we are unable to determine precise values by a period search analysis due to the short dataset. Further study on this topic with a longer dataset is required.

Taking into account possible longer rotational periods of the activity indicators and comparing them with the B_l behaviour regarding the surface rotational period (the photometric one), there might be a correlation in their behaviour, and also a good coincidence with the ZDI map (Fig. 4.2). The indicators have a stronger intensity at phases around $0.4 - 0.5$ when we observe areas with positive and negative polarities and the resultant B_l is close to 0. At the opposite, they have a weaker intensity near phase 0 when the negative polarities are dominant in the resultant longitudinal magnetic field.

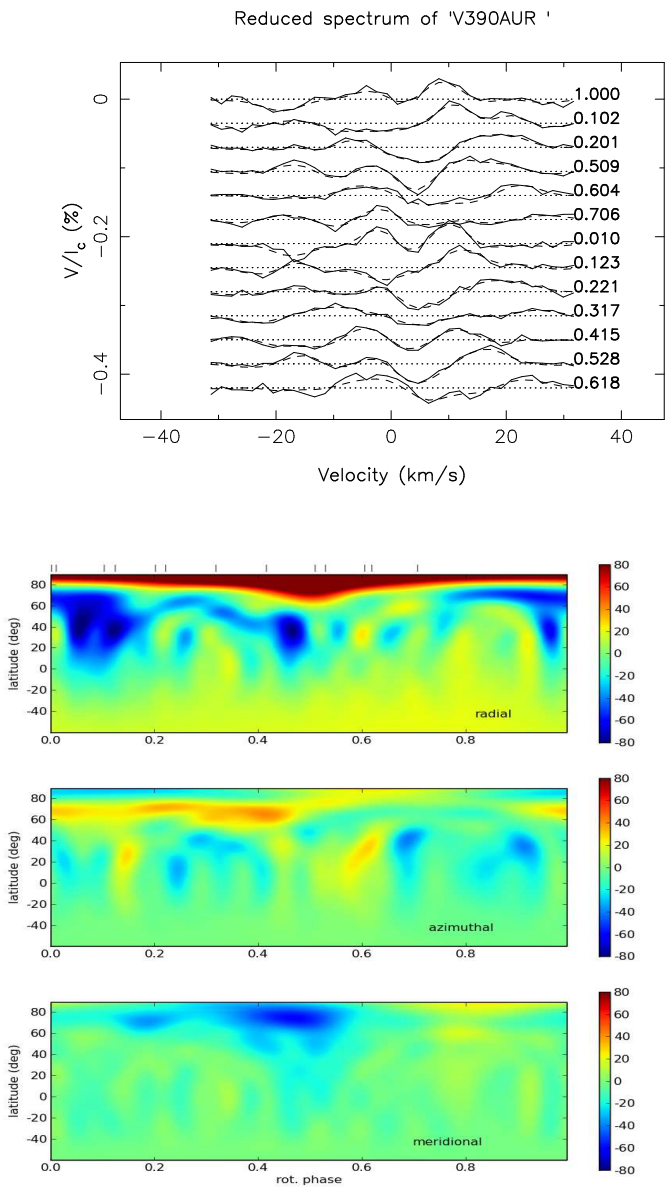

Figure 4.2: Upper pannel: *LSD Stokes V profiles (solid lines) and their fit (dashed lines) after a correction of the mean radial velocity of the star. For display purposes the profiles are shifted vertically and the dotted horizontal lines indicate the zero level.* ***Lower pannels:*** *Radial, azimuthal and meridional maps for the reconstructed magnetic field for V390 Aur. The vertical ticks in the upper part of the radial map show the phases when there are observations.*

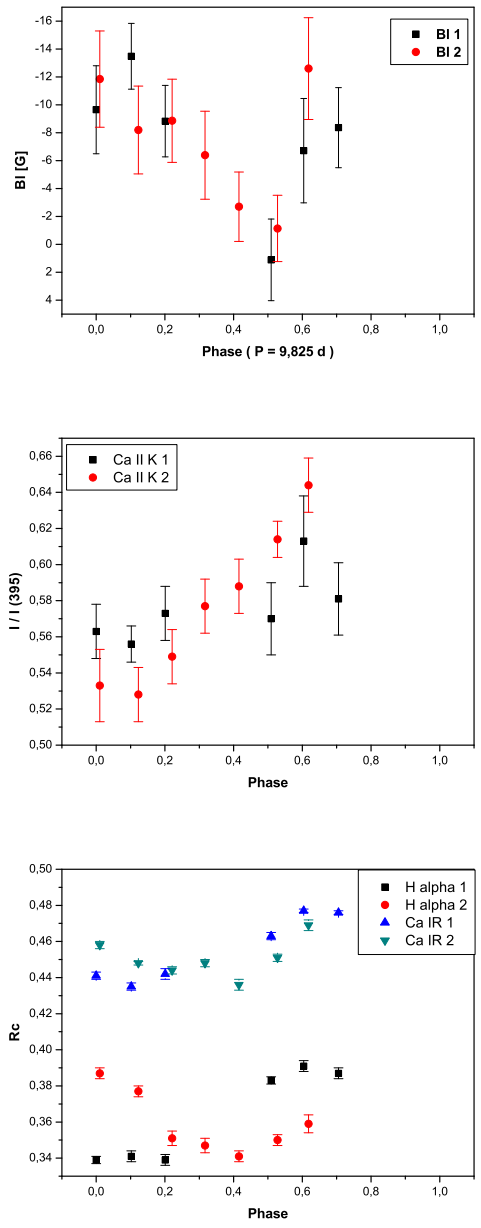

Figure 4.3: *B_l, CaII K, Hα and CaII IR 854.2 nm behaviour for V390 Aur. Phase is for the photometric period of 9.825 d. The different colors in each of them correspond to a different rotation (see the legend on each pannel).*

4.4 *Stellar parameters, Li abundance and* $v \sin i$

With the aim of improving the precision on lithium abundance ($N_{Li} = \log[n(Li)/n(H)] + 12$) and stellar parameters (T_{eff}, $\log g$ and $[Fe/H]$), we performed a spectral synthesis analysis on the Stokes I spectra of V390 Aur. We used MARCS models of atmosphere (Gustafsson et al. 2008) and the TurboSpectrum code (Alvarez & Plez 1998) in order to produce high resolution synthetic spectra of the lithium line region around 671 nm (see Canto-Martins et al. 2006 and 2011 for the complete method and for atomic and molecular line lists references). Best fit is displayed in Figure 4.4. It is obtained for $T_{eff} = 4970\ K \pm 50\ K$, $\log g = 3.0 \pm 0.2\ dex$, and $[Fe/H] = -0.05 \pm 0.05\ dex$ with a microturbulence velocity of 1.5 km/s and taking into account (with a radial tangent profile) a macroturbulence velocity of 8 km/s. Line broadening is then correctly reproduced with a rotation profile and $v \sin i = 25 \pm 1\ km/s$. We checked that this solution also easily and correctly fits other spectral regions throughout the *Narval* wavelength range. Our T_{eff} value is in perfect agreement with that derived by Gondoin (2003) and Bell & Gustafsson (1989) ($4970 \pm 200\ K$) and is very similar to the value of 5000 K obtained by Fekel & Balachandran (1993). We determined a lithium abundance $N_{Li} = 1.6 \pm 0.15\ dex$. This value is in very good agreement with the previous determination of 1.5 ± 0.2 made by Fekel & Balachandran (1993) and slightly lower than the value of 1.8 obtained by Brown et al. (1989).

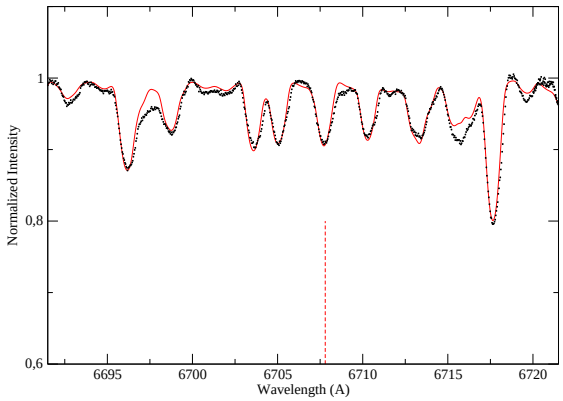

Figure 4.4: *The solid line is fit with the model of the spectral lines in the Li region (671 nm). The dashed vertical line indicates the position of the LiI 670.8 nm.*

4.5 *Evolutionary status*

The position of V390 Aur in the HRD is shown in Fig. 4.5. We adopt the effective temperature of 4970 ± 50 K that we derived from the Stokes I spectra. The luminosity is obtained using the parallax of the star given in the New Reduction Hipparcos catalogue by van Leeuwen (2007), the V magnitude from the 1997 Hipparcos catalogue, and the bolometric correction following Buzzoni et al. (2010) prescription (i.e., $BC = -0.253$); the error bar reflects only the uncertainty of the parallax. The adopted parameters lead to a stellar radius of 6.4 $R_{\odot}$.

Figure 4.5 also presents evolutionary tracks corresponding to up-to-date stellar models of various initial masses computed with the code STAREVOL[1] at solar metallicity, which is very close from the $[Fe/H] = -0.05 \pm 0.05$ dex derived from the Stokes I spectra and only slightly higher than that derived by Fekel & Balachandran (1993; $[Fe/H] = -0.3$). We plot standard (non-rotating) tracks, except in the 2.25 $M_{\odot}$ case, for which we also show predictions for rotating models with initial rotation velocities on the zero age main sequence of 50 and 110 km/s (the higher the rotation velocity, the brighter the track). Rotating models are computed using Zahn (1992) and Maeder & Zahn (1998) formalism where the transport of angular momentum and chemicals is dominated by the Eddington-Sweet meridional circulation and shear instabilities (see Charbonnel & Lagarde 2010 for details on the model assumptions and input microphysics). For clarity the tracks are drawn up to the RGB tip only, but the dashed-dotted line shows the location of the clump (i.e., the beginning of central He-burning) for the various masses considered. Additionally the dashed lines indicate the beginning and the end of the first dredge-up (warmer and cooler lines respectively).

Based on these up-to-date models and taking into account the observational uncertainties, we determine a mass of 2.25 ± 0.25 $M_{\odot}$ for V390 Aur. Note that at the location of V390 Aur the effect of rotation on the mass determination is negligible compared to the uncertainties on the parallax and on the effective temperature. The star appears to start the ascent of the RGB and is not bright enough to lie in the clump. This agrees with previous studies by Gondoin (2003) and Konstantinova-Antova et al. (2009), which identified V390 Aur as a star of about $1.8 - 2$ $M_{\odot}$ located at the base of the RGB.[2]

[1] Most of the models shown in Fig. 4.5 are from Charbonnel & Lagarde (2010) and Lagarde et al., in prep. The 2.25 $M_{\odot}$ models were computed especially for the present study with the same assumptions and input physics.

[2] Charbonnel & Balachandran (2000) determined a mass of 1.1 ± 0.5 $M_{\odot}$ for V390 Aur, due to an error in the assumed T_{eff} for this star (see their Table 1).

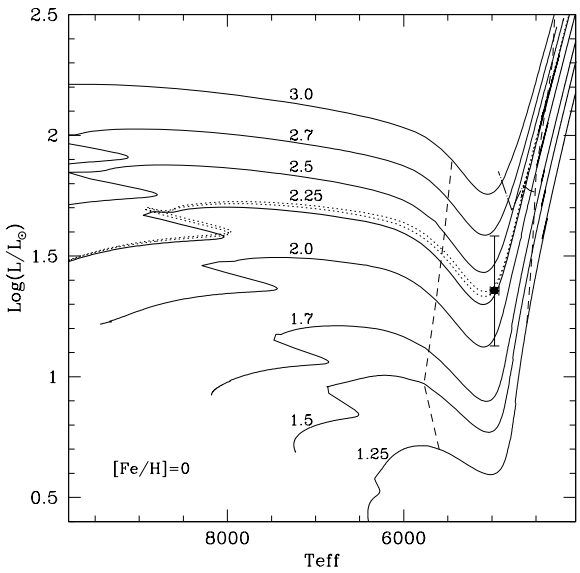

Figure 4.5: *Position of V390 Aur in the HRD. The adopted effective temperature is determined from our analysis of the Stokes I spectra of V390 Aur. The luminosity is estimated using the parallax from the New Reduction Hipparcos catalogue by van Leeuwen (2007; see text for more details). Standard evolutionary tracks (solid lines) computed for* $[Fe/H] = 0$ *are shown up to the RGB tip for different labelled stellar masses. For the* $2.25\ M_{\odot}$ *case, the predictions for models with rotation-induced mixing treated as in Charbonnel & Lagarde (2010) are also shown for two initial rotation velocities of 50 and* $110\ km/s$ *(dotted lines). The dashed lines delimit the first dredge-up, the cooler line marking the deepest penetration of the convective envelope. The dashed-dotted line indicates the beginning of central He-burning for the mass range covered by the tracks.*

4.6 *Lithium abundance and rotation*

At the base of the RGB, the star experiences the so-called first dredge-up (see the dashed lines in Fig. 4.5). Although its convective envelope has not yet reached its maximum extent in depth, it already encompasses $\sim 0.83\ M_{\odot}$ and $\sim 0.54\ R_{*}$ at the location in the HRD of V390 Aur. Starting from the lithium interstellar medium abundance of 3.3, the corresponding standard Li dilution is found to lead to a theoretical surface abundance $N(Li)$ equal to 1.68 (where $N(Li) = \log[n(Li)/n(H)] + 12$) at this evolutionary point. This prediction is in rather good agreement with our observational value of 1.6 ± 0.15. We note however that in this domain in stellar mass and effective temperature many subgiant and giant stars exhibit Li abundances significantly lower than predicted by the standard dilution models (do Nascimento et al. 2000, de Laverny et al. 2003, Canto Martins et al. 2011). This is well accounted for by additional Li depletion due to rotational mixing on the main sequence (Charbonnel & Talon 1999, Palacios et al. 2003, Pasquini et al. 2004, Charbonnel & Lagarde 2010 and references therein). For initial rotation velocities of 50 and 110 km/s our 2.25 $M_{\odot}$ rotating models predict respectively $N(Li)$ of 1.46 and 0.87 at the effective temperature of V390 Aur. The Li content of V390 Aur can thus be explained by assuming that the star arrived on the main sequence with a modest rotation velocity of the order of 50 km/s.

Additionally, let us recall that V390 Aur has a rather high rotation velocity for its evolutionary stage (35 km/s for $v \sin i = 29\ km/s$ and $i = 56°$), as already noted by Fekel & Balachandran (1993). This is rather peculiar since most (i.e., more than 95%) of the stars of the same spectral class have already been spun down to a rotational velocity of $\sim 5\ km/s$ or less (Gray 1982, de Medeiros et al. 1996 b, de Medeiros & Mayor 1999). This general behaviour can be explained simply by changes in the moment of inertia and in the stellar radius when the stars evolve to the RGB, and the transition to a slow rotation occurs at an effective temperature at the order of 5500 K. Taking into account this secular effect and assuming rigid-body rotation and conservation of angular momentum for our 2.25 $M_{\odot}$ model, one can obtain a maximum rotation velocity of only $\sim 15\ km/s$ (for a rotation velocity of 180 km/s on the zero age main sequence) at the location of V390 Aur in the HRD.

Although fast rotation is observed only in few percents of red giant stars, it appears to be a common feature of a group of chromospherically active single giants (Fekel & Balachandran 1993, Konstantinova-Antova et al. 2009). For the moment, possible explanations for their faster rotation could be angular momentum dredge-up from the faster rotating interior during the first

dredge-up phase (Simon & Drake 1989), or spin-up from planet engulfment that could also increase the lithium abundance (Siess & Livio 1999, Livio & Soker 2002, Massarotti et al. 2008, Carlberg et al. 2009). The first option requires rotation gradient in the stellar interior with the near core region spinning much faster than the more external layers. According to the theoretical works by Palacios et al. (2006) and Brun & Palacios (2009) rotational gradients, both radial and longitudinal ones, should appear in the convective envelope and the radiative zone for stars with mass up to $2 - 2.5\ M_{\odot}$ during the first dredge-up phase and the beginning ascend of the RGB. Our observations support their predictions for gradients in the convective envelope. In addition, a gradient between the envelope and (presumable) fast rotating radiative interior could dredge-up angular momentum and speed-up the upper convective layers and the surface (as we observe in V390 Aur and other fast rotating single giants).

On the other hand, recent discoveries of Jupiter-mass planets orbiting their host star at inner-solar system distances could also be considered as a possible explanation of the Li content and fast rotation in V390 Aur. Applying the formula by Massarotti (2008) with the parameters obtained by our model and assuming a circular orbit with a semi-major axis equal to the radius of the star (hypothesis for the just engulfed planet, that could explain not only the fast rotation, but also the enchanced Li), we estimate that the star has to engulf a brown dwarf of about 20 M_{Jup} to explain its V_{eq} of 34 km/s. In the same time, however, Alibert et al. (2011) point out the observed lack of short period planets orbiting 2 $M_{\odot}$ stars.

As to the forcing of stellar rotation by a close companion, let us recall that V390 Aur was found to be a wide binary system and synchronization cannot play a role in its fast rotation (Konstantinova-Antova et al. 2008 b).

4.7 *Dynamo*

On the basis of the theoretical convective turnover time and assuming that the photometric period (9.825 d) is the rotational one, we can estimate the value of the Rossby number for V390 Aur. If the value of 126 d (for a layer that corresponds to $1/2H_p$ above the base of the convective envelope) is considered, which is obtained from our standard 2.25 $M_{\odot}$ model (computed with a mixing length parameter of 1.6) at the location of V390 Aur in the HRD, then the Rossby number is 0.08. In the case of convective turnover time of 52 days, i.e. the value determined for the middle (in radius) of the convective envelope, the Rossby number is 0.19. In both cases, these values are indicative of a very efficient $\alpha - \omega$ dynamo.

4.8 *Discussion*

The present study revealed a complex structure of the magnetic field at the surface of V390 Aur. In addition to the magnetic polar spot of positive polarity, groups of close situated magnetic spots of negative polarity are detected at mid-latitudes. Such polar spots are predicted for fast rotators by Schüssler (1996), and observed by Petit et al. (2004). Temperature polar spots are reported for giants in RS CVn systems and for FK Com-type stars by Strassmeier (1997), Korhonen et al. (2002) and Strassmeier (2002).

This surface structure with close magnetic spots could explain the flare activity properties of the star reported in optical and X-ray (Konstantinova-Antova et al. 2000, Gondoin 2003, Konstantinova-Antova et al. 2005 a), like the groups of optical flares and the "continuous flare activity" in the corona.

The observed azimuthal map belt at high-latitude could be interpreted as a toroidal component near the surface (like in the FK Com-type star HD 199178 and in the RS CVn star HR 1099, Petit et al. 2004 a, b) and is indicative of the site of the dynamo operation. In this star, it is possible for the dynamo to operate not close to the base of the convective envelope, but in a whole region within it. The other possibility is the toroidal magnetic field to be formed near the base of the convection zone and to rise up as one whole. This possibility is less likely, because of the vigorous convection during the first dredge-up phase. The first assumption, however, presumes the existence of a gradient of rotation in the convective envelope closer to the surface, not only at its base. The fast surface rotation of V390 Aur and the significant differential rotation $\Delta\Omega = 0.048\ rad/d$ are in support of such a rotational gradient.

The comparison to solar-type dwarfs revealed that Sun-like stars seem to display a higher fraction of toroidal field for a rotation period similar to that of V390 Aur (Petit et al. 2008). The mostly poloidal field geometry is more reminiscent of M dwarfs with deep convective envelopes (Morin et al. 2008 b, 2010). But, one must be cautious about this question, because the fraction of toroidal field can vary significantly during stellar cycles (Petit et al. 2009).

Conclusions

Studying magnetic activity in cool single giants is crucial for understanding the role of magnetic fields in the late stages of stellar evolution. By analogy with cool stars on the main sequence, large-scale magnetic fields of cool evolved stars may be the product of a large-scale dynamo, triggered by the interplay between internal differential rotation and convection in the stellar envelope (Konstantinova-Antova et al. 2012). Their magnetic fields may also be a fossil remnant inherited from previous evolutionary stages, still frozen in stable internal layers of the star and either pervading convective layers up to the surface or interacting with a global dynamo (Aurière et al. 2008, 2011, 2012).

This second scenario may be of particular importance for those cool giants that are the descendants of Ap/Bp stars. The fossil field hypothesis is generally preferred to account for the strong and topologically simple surface magnetic fields of main sequence Ap/Bp stars, and this fossil magnetism may still remain hidden in the internal layers of the Ap star after their departure from the main sequence, leading to magnetic properties different from those of a global dynamo.

Observations are obviously essential for deciding between these different scenarios or unveil other possible physical explanations for the manifestations of the magnetic activity recorded in cool, evolved stars. To understand better the overall picture of magnetism of late type giants, three stars are studied in this work – β Ceti, EK Eri and V390 Aur. Two of them, β Ceti and EK Eri, are slowly rotating giants with $v \sin i$ of 3.5 km/s and 0.5 km/s, respectively. The third one, V390 Aur, is a fast rotator with $v \sin i$ of 29 km/s. Observational data are obtained with the spectropolarimeters *Narval* (β Ceti, EK Eri, V390 Aur) at Pic du Midi Observatory, France, and *ESPaDOnS* (β Ceti) at CFHT. Summarized results for individual stars are as follows:

β *Ceti*

The data for the cool giant β Ceti cover the period June 2010 – January 2012. The temporal modulation of polarized signatures is consistent with a rotation period of 215 d. Using the spectropolarimetric dataset, we were able to reconstruct two magnetic maps (taken one year apart) of the surface magnetic field topology of the star employing the Zeeman Doppler Imaging technique. Both magnetic maps display very similar magnetic geometries, with a global magnetic field dominated by a dipolar configuration (the poloidal component contains about 96 % of the reconstructed magnetic energy), with a dipole axis almost aligned on the spin axis. The polar field strength is close to 20 G for both maps.

The longitudinal magnetic field B_l has significant variations in the interval $0.1 - 8.2$ G and stays with a positive polarity for the whole observational period. Sinusoidal variations of B_l are consistent with a large-scale dipole field configuration. The behavior of the line activity indicators $H\alpha$, CaII K, CaII IR, and the radial velocity correlate rather well with the B_l variations, giving further support to the dipolar model produced by ZDI.

Based on a comparison with recent stellar models (computed with the same assumptions and input physics as in Charbonnel & Lagarde 2010), we derive a mass of 3.5 $M_{\odot}$ for β Ceti and propose that this star is already in the central helium-burning phase rather than starting the first ascent of the red giant branch. The evolutionary status is also supported by comparison between observed and theoretical values for the lithium abundance and carbon isotopic ratio at the stellar surface. Based on our evolutionary models, we derive a convective turnover time equal to $\tau_c = 171$ days, and we estimate the Rossby number of β Ceti to be $Ro = 1.26$ ($Ro = P_{rot}/\tau_c$, on the basis of the rotation period, which we determine using ZDI technique), suggesting that a large-scale dynamo alone may not be able to account for the high activity of the star.

We derived four useful clues here to better understand the magnetic nature of β Ceti with: (a) a mass of 3.5 $M_{\odot}$, which is consistent with the typical masses of chemically-peculiar stars; (b) a long rotation period of 215 d and a $Ro = 1.26$, that seem unable to account for the high activity level recorded for this object through dynamo action alone; (c) a simple and stable magnetic topology consistent with dominantly dipolar field geometries observed in Ap/Bp stars; (d) a polar field strength of about 20 G, which when back-extrapolated to the main sequence, is consistent with typical field strengths of Ap/Bp stars. Considering all this information together, we propose that the magnetism of β Ceti may be of fossil origin and inherited from a main sequence Ap/Bp star.

EK Eri

Spectropolarimetric observations of EK Eri (located at the end of the Hertzsprung gap and the beginning of the first dredge-up phase) have been obtained during 4 seasons, September 2007 – March 2011, corresponding to about 4 photometric periods of 308.8 d duration.

The longitudinal magnetic field B_l is detected consistently, with B_l variations of up to about 80 G without any reversal of its sign. The maximum of $|B_l|$ is observed to coincide with the phase of photometric light minimum (i.e. phase 0.0 of the photometric ephemeris of DBSS10).

The activity indicators measured from CaII K&H, the CaII IR triplet and $H\alpha$ are shown to vary with small amplitude and in phase with $|B_l|$. However some strong deviations are observed, which may suggest episodes of flares.

The radial velocity also varies in a reasonably coherent way according to the photometric ephemeris, but with a phase delay of about 0.1 cycles.

For the Zeeman Doppler imaging investigation it was used the 308.8 d photometric period (DBSS10), which is similar to our best rotational period, based on quality-of-fit of the ZDI maps, of about 311 d.

For all the described models we find that the large-scale magnetic field of EK Eri is poloidal (more than 98 % of the magnetic energy is contained in this component). In addition, the surface magnetic field variations of EK Eri appear to be dominated by a strong magnetic spot (of negative polarity), which is phased with the darker, redder (and therefore presumably cool) photometric spot.

The ratio between dipolar and quadrupolar components of the magnetic field increases with decreasing value of the rotational axis inclination i. Whereas the quadrupolar component dominates for i greater than 80°, for $i = 60°$ we obtain a model that is almost purely dipolar. In the dipolar model, the photometric spot at phase 0 corresponds to the pole of negative polarity of the dipole, which could be the remnant of that of the Ap star progenitor of EK Eri.

V390 Aur

The observaional data for V390 Aur were collected during September 2008.

The complex structure of the surface magnetic field in the ZDI map and the analysis of the poloidal and toroidal field components suggest a dynamo operation in V390 Aur. It is rather likely for the dynamo to be of $\alpha-\omega$ type, taking into account the fast rotation and the evolutionary stage of V390 Aur

(base of the RGB) with a well-developed convective envelope. The calculated Rossby number obtained from tailor-made stellar evolution models is also in support of an efficient $\alpha - \omega$ dynamo. A significant toroidal component is developed, which results in low-latitude spots and an azimuthal field belt at the surface. Such a belt is already observed in FK Com and RS CVn-type stars. A possible explanation is that there is a gradient of the rotation in the extended convective envelope, which exists during the first dredge-up phase and it is possible for the dynamo to operate within it, not only at the base of this envelope, as it is the case of a classical solar-type dynamo, but also closer to the surface.

The structure of the surface magnetic field with close situated active areas could also explain the properties of the flare activity in V390 Aur, observed in the past: groups of optical flares and continuous flaring in the corona.

The activity indicators behavior points to a possible decrease of the rotation rate in the chromosphere compared to the rate in the photosphere. Further study is necessary to determine the exact rotation periods for the activity indicators in the chromosphere.

Main Contributions

1. The properties of the magnetic field of two magnetic late-type single giants, EK Eri and β Ceti, are studied by means of ZDI and the behavior of the activity indicators with time – the magnetic model is almost purely dipolar. These two stars are at different evolutionary stages – EK Eri is at the first dredge-up and β Ceti is at the core He-burning phase, and both of them are suspected of being descendants of Ap stars during the main sequence. The study indicates that the magnetic fields in Ap stars survive till advanced evolutionary stages, like core He-burning is. In this way for the first time is answered the question what is the fate of an Ap star after the main sequence.

2. Another star of similar mass, studied in the same way, and being at the first dredge-up phase is the fast rotator V390 Aur. It is rather likely that the magnetic activity of the star is due to an $\alpha - \omega$ dynamo. The surface magnetic field shows a complex structure and an azimuthal field belt is presented, which indicates a toroidal field close to the surface and a dynamo operation within the convective envelope. For the first time is observed a vertical gradient of rotation in the atmosphere, in agreement with the predictions of the theoretical works by Palacios et al. (2006) and Brun & Palacios (2009).

List of publications, talks and posters

Publications on the PhD topic

"Magnetic field structure in single late-type giants: β Ceti in 2010-2012"
Tsvetkova, S., Petit, P., Aurière, M., Konstantinova-Antova, R., Wade, G.A., Charbonnel, C., Decressin, T. & Bogdanovski, R., 2013, A&A, 556, 43

"Magnetic field structure in single late-type giants: the effectively single giant V390 Aurigae"
Konstantinova-Antova, R., Aurière, M., Petit, P., Charbonnel, C., **Tsvetkova, S.**, Lèbre, A. & Bogdanovski, R., 2012, A&A, 541, 44

"A dominant magnetic dipole for the evolved Ap star candidate EK Eridani"
Aurière, M., Konstantinova-Antova, R., Petit, P., Roudier, T., Donati, J.-F., Charbonnel, C., Dintrans, B., Lignières, F., Wade, G.A., Morgenthaler, A. & **Tsvetkova, S.**, 2011, A&A, 534, 139

Talks and posters

"Magnetic field structure in single late-type giants: β Ceti in 2010-2012"
Tsvetkova, S., Petit, P., Aurière, M., Konstantinova-Antova, R., Wade, G.A., Charbonnel, C., Decressin, T. & Bogdanovski, R., 2012, "The second

Bcool workshop", Germany (talk)

"The magnetic field structure of the single late-type giant β Ceti in the period June 2010-January 2012"

Tsvetkova, S., Petit, P., Aurière, M., Konstantinova-Antova, R., Charbonnel, C., Wade, G.A. & Bogdanovski, R., 2012, "The 17th Cambridge Workshop on Cool Stars, Stellar Systems and the Sun", Barcelona, Spain (poster)

"Magnetic field and activity indicators in the single late-type giant β Ceti"

Tsvetkova, S., Aurière, M., Konstantinova-Antova, R., Wade, G.A., Bogdanovski, R. & Petit, P., 2011, "International advanced research school in physics: Physics of stars", Turkey (talk)

"Magnetic Field Structure and Activity in the Single Late Type Giant β Ceti"

Tsvetkova, S., Aurière, M., Petit, P., Konstantinova-Antova, R., Wade, G.A. & Bogdanovski, R., 2011, "30 years NAO Rozhen", Bulgaria (talk)

Citations found in ADS

"Magnetic field structure in single late-type giants: β Ceti in 2010-2012" – Tsvetkova et al. 2013, A&A, 556, 43

1. Korhonen 2013, Invited review in the IAU Symposium 302 "Magnetic Fields Throughout Stellar Evolution", [arXiv1310.3678]

"Magnetic field structure in single late-type giants: the effectively single giant V390 Aurigae" – Konstantinova-Antova et al. 2012, A&A, 541, 44

1. Mathur et al. 2014, JSWSC, 4, 15
2. Gaulme et al. 2014, ApJ, 785, 5
3. Landstreet 2013, EAS, 63, 67
4. Hedges et al. 2013, ASPC, 479, 197

"A dominant magnetic dipole for the evolved Ap star candidate EK Eridani" – Aurière et al. 2011, A&A, 534, 139

1. Gaulme et al. 2014, ApJ, 785, 5
2. Bychkov et al. 2013, AJ, 146, 74
3. Mathys 2012, ASPC, 462, 295
4. Kochukhov et al. 2012, MNRAS, 421, 3004
5. Mathys et al. 2012, IAUTA, 28, 203

Acknowledgements

The present study is a project performed in collaboration with other people, it is not an effort of one person. It is a great pleasure for me to thank all of them.

Foremost, I would like to express my deep respect and gratitude to my supervisor, Assoc. Prof. Dr. Renada Konstantinova-Antova, for the patient guidance and encouragement she provided to me and sharing her immense knowledge with me, during all these years of education and research in astronomy. Without her assistance and dedicated involvement in every step throughout the process, this thesis would have never been accomplished.

I am grateful to Prof. Michel Aurière and Dr. Pascal Petit for their mentorship and sharing a lot of time with me to teach me in some methods, programs and knowledges in the field of magnetism and activity in stars. I appreciate their hospitality during my stay in France.

I am thankful to Dr. Rémi Cabanac, who is the Director of the 2-m Télescope Bernard Lyot, Pic du Midi Observatory, France, for giving me the opportunity to work at TBL as a service observer during 2010. I thank the TBL staff that they accept me as a member of their team.

In addition, I also would like to thank all my colleagues and the administrative staff from the Institute of Astronomy and NAO, and my foreign co-authors, who gave me some help at any moment during my PhD.

Last but not the least, I am beyond grateful to my parents and my brother for their support, understanding and love.

I am thankful to the contracts BG05PO001-3.3.06-0047 and DO 02-85 for some financial support.

References

- Alibert, Y., Mordasini, C. & Benz, W. 2011, A&A, 526, 63
- Allende Prieto, C. & Lambert, D.L. 1999, A&A, 352, 555
- Alvarez, R. & Plez, B. 1998, A&A, 330, 1109
- Anderson, L.S. & Athay, R.G. 1989, ApJ, 346, 1010
- Angel, J.R.P, Borra, E.F. & Landstreet, J.D. 1981, ApJS, 45, 457
- Aurière, M. 2003, in "Magnetism and Activity of the Sun and Stars", Eds J. Arnaud and N. Meunier, EAS Publ. Series 9, 105
- Aurière, M., Wade, G.A., Silvester, J. et al. 2007, A&A, 475, 1053
- Aurière, M., Konstantinova-Antova, R., Petit, P. et al. 2008, A&A, 491, 499
- Aurière, M., Konstantinova-Antova, R., Petit, P., Wade, G. & Roudier, T. 2009 a, IAUS, 259, 431
- Aurière, M., Wade, G.A., Konstantinova-Antova, R. et al. 2009 b, A&A, 504, 231
- Aurière, M., Donati, J.-F., Konstantinova-Antova, R. et al. 2010, A&A, 516, L2
- Aurière, M., Konstantinova-Antova, R., Petit, P. et al. 2011, A&A, 534, 139
- Aurière, M., Konstantinova-Antova, R., Petit, P. et al. 2012, A&A, 543, 118

- Ayres, T.R., Osten, R.A. & Brown, A. 2001, ApJ, 562, L83
- Babcock, H.W. 1947, ApJ, 105, 105
- Babcock, H.W. 1961, ApJ, 133, 572
- Basri, G. Marcy, G.W. & Valenti, J.A. 1992, ApJ, 390, 622
- Beckers, J.M. 1969, Physical Science Research Papers no. 371, SPO and Air Force Cambridge Research Laboratories, Bedford, MA.
- Bell, R.A. & Gustafsson B. 1989, MNRAS, 236, 653
- Berdyugina, S.V. 2002, Astron. Nachr., 323, 192
- Berdyugina, S.V., "Starspots: A Key to the Stellar Dynamo", 2005, *Living Rev. Solar Phys.*, 2, 8
- Berdyugina, S.V. & Marsden, S.C. 2006, ASPC, 358, 385
- Berio, P., Merle, T., Theverin, F. et al. 2011, A&A, 535, 59
- Bloomfield, P. 2000, *"Fourier analysis of time series: an introduction"*, second edition, New York, John Wiley & Sons, Inc., 261
- Bopp, B.W. & Rucinski, S.M. 1981, IAUS, 93, 177, *"The Rapidly Rotating Giants of the FK Comae Type"*, in Fundamental Problems in the Theory of Stellar Evolution, (Eds.) Sugimoto, D., Lamb, D.G., Schramm, D.N., IAU Symposium 93, held at Kyoto University, Kyoto, Japan, July 22–25, 1980, p. 177, D. Reidel, Dordrecht, Netherlands; Boston, U.S.A.
- Bopp, B.W. & Stencel, R.E. 1981, ApJ, 247, L131
- Borra, E.F., Edwards, G. & Mayor, M. 1984, ApJ, 284, 211
- Bouvier, J., Alencar, S.H.P., Harries, T.J., Johns-Krull, C.M. & Romanova, M.M. 2007, *"Protostars and planets" conference*, University of Arizona Press, Tucson, 951 pp., 2007, p. 479-494
- Brown, D.N. & Landstreet, J.D. 1981, ApJ, 246, 899
- Brown, J.A., Sneden, C., Lambert, D.L. & Dutchover, E. Jr. 1989, ApJS, 71, 293
- Brown, S.F., Donati, J.-F., Rees, D.E. & Semel, M. 1991, A&A, 250, 463

- Brun, A.S. & Palacios, A. 2009, ApJ, 702, 1078
- Buscombe, W. & Kennedy, P.M. 1968, MNRAS, 139, 341
- Buzzoni, A., Patelli, L., Bellazzini, M. et al. 2010, MNRAS, 403, 1592
- Canto Martins, B.L., Lèbre, A., de Laverny, P. et al. 2006, A&A, 451, 993
- Canto Martins, B.L., Lèbre, A., Palacios, A. et al. 2011, A&A, 527, A94
- Carlberg, J.K., Majewski, S.R. & Arras, P. 2009, ApJ, 700, 832
- Carney, Bruce W., Gray, David F., Yong, D. et al. 2008, AJ, 135, 892
- Cattaneo, F., Emonet, T. & Weiss, N. 2003, ApJ, 588, 1183
- Charbonneau, P. 2010, *"Dynamo models of the solar cycle"*, Living Rev. Solar Phys. 7, (2010), 3.
- Charbonnel, C. 1994, A&A, 282, 811
- Charbonnel, C. 1995, ApJ, 453, L41
- Charbonnel, C. & Talon, S. 1999, A&A, 351, 635
- Charbonnel, C. & Balachandran, S.C. 2000, A&A, 359, 563
- Charbonnel, C. & Zahn, J.-P. 2007, A&A, 467, L15
- Charbonnel, c. & Lagarde, N. 2010, A&A, 522, 10
- Charbonnel, C., Lagarde, N. & Eggenberger, P. 2012, Proc. of the workshop "Red Giants as Probes of the Structure and Evolution of the Milky Way", Astrophysics and Space Science Proceedings, Springer-Verlag Berlin Heidelberg, 2012, p. 115
- Claret, A. & Bloemen, S. 2011, A&A, 529, 75
- Dall, T.H., Bruntt, H., Stello, D. & Strassmeier, K.G. A&A, 2010, 514, 25 (DBSS10)
- de Laverny, P., do Nascimento, J.D.,Jr., Lèbre, A., De Medeiros, J.R. 2003, A&A 410, 937
- de Medeiros, J.R., Melo, C.H.F. & Mayor, M. 1996 a, A&A, 309, 465

- de Medeiros, J.R., Da Rocha, C. & Mayor, M. 1996 b, A&A, 314, 499
- de Medeiros, J.R. & Mayor, M. 1999, A&AS, 139, 433
- Dearborn, D.S.P., Eggleton, P.P. & Schramm, D.N. 1976, ApJ, 203, 455
- Deeming, T.J. 1975, Ap&SS, 36, 137
- Derman, E., Demircan, O. & Özeren, F.F. 1989, PASP, 101, 677
- Deutsch, A.J. 1958, "Harmonic Analysis of the Periodic Spectrum Variables", in Electromagnetic Phenomena in Cosmical Physics, (Ed.) Lehnert, B., IAU Symposium no. 6, pp. 209–221, Cambridge University Press, Cambridge, U.K.
- Dikpati, M., de Toma, G., Gilman, P.A., Arge, C.N. & White, O.R. 2004, ApJ, 601, 1136
- do Nascimento, J.D., Jr., Charbonnel, C., Lèbre, A., de Laverny, P. & de Medeiros, J.R. A&A, 357, 931
- Donati, J.-F., Semel, M. & Praderie, F. 1989, A&A, 225, 467
- Donati, J.-F., Semel, M., Rees, D.E., Taylor, K. & Robinson, R.D. 1990, A&A, 232, L1
- Donati, J.-F., Semel, M. & Rees, D.E. 1992, A&A, 265, 669
- Donati, J.-F. & Brown, S.F. 1997, A&A, 326, 1135
- Donati, J.-F., Semel, M., Carter, B.D., Rees, D.E. & Collier Cameron, A. 1997, MNRAS, 291, 658
- Donati, J.-F. 1999, MNRAS, 302, 457
- Donati, J.-F. 2001, "Imaging the Magnetic Topologies of Cool Active Stars", in *Astrotomography: Indirect Imaging Methods in Observational Astronomy*, (Eds.) Boffin, H.M.J., Steeghs, D., Cuypers, J., vol. 573 of Lecture Notes in Physics, pp. 207 – 231, Springer
- Donati, J.-F. 2003, ASPC, 307, 41
- Donati, J.-F., Collier Cameron, A., Semel, M. et al. 2003 a, MNRAS, 345, 1145

- Donati, J.-F., Collier Cameron, A. & Petit, P. 2003 b, MNRAS, 345, 1187
- Donati, J.-F., Catala C., Landstreet J. & Petit P. 2006 a, in Casini R., Lites B., eds, Solar Polarization Workshop n4 Vol.358 of ASPC series, 362
- Donati, J.-F., Howarth, I.D., Jardine, M.M. et al. 2006 b, MNRAS, 370, 629
- Donati, J.-F., Jardine, M.M., Gregory, S.G. et al. 2007, MNRAS, 380, 1297
- Donati, J.-F., Jardine, M.M., Gregory, S.G. et al. 2008 a, MNRAS, 386, 1234
- Donati, J.-F., Morin, J., Petit, P., Delfosse, X., Forveille, T. et al. 2008 b, MNRAS, 390, 545
- Donati, J.-F. & Landstreet, J.D. 2009, ARA&A, 47, 333
- Donati, J.-F., Bouvier, J., Walter, F.M. et al. 2011 a, MNRAS, 412, 2454
- Donati, J.-F., Gregory, S.G., Montmerle, T. et al. 2011 b, MNRAS, 417, 1747
- Dorren, J.D. & Guinan, E.F. 1982, AJ, 87, 1546
- Drake, S.A., Simon, T. & Linsky, J.L. 1989, ApJ Suppl. Ser. 71, 905
- Duncan, D.K., Vaughan, A.H., Wilson, O.C. et al. 1991, ApJS, 76, 383
- Eriksson, K., Linsky, J.L. & Simon, T. 1983, ApJ, 272, 665
- Featherstone, N.A., Browning, M.K., Brun, A.S. & Toomre, J. 2009, ApJ, 705, 1000
- Fekel, F.C. & Marschall, L.A. 1991, AJ, 102, 1439
- Fekel, F.C. & Balachandran, S. 1993, ApJ, 403, 708
- Fekel, F.C. 1997, PASP, 109, 514
- Flower, P.J. 1996, ApJ, 469, 355
- Foster, G. 1995, AJ, 109, 1889

- Frost, Edwin B. 1923, Popular Astronomy, 31, 289
- Gilroy, K.K. 1989, ApJ, 347, 835
- Gilroy, K.K. & Brown, J.A. 1991, ApJ, 371, 578
- Goncharskii, A.V., Stepanov, V.V., Khokhlova, V.L. & Yagola, A.G. 1977, "Reconstruction of local line profiles from those observed in an Ap spectrum", *Sov. Astron. Lett.*, 3, 147–149
- Gondoin, P. 1999, A&A, 352, 217
- Gondoin, P. 2003, A&A, 404, 355
- Gratton, R.G., Sneden, C., Carretta, E. & Bragaglia, A. 2000, A&A, 354, 169
- Gray, D.F. 1982, ApJ, 262, 682
- Gray, D.F. 1989 b, PASP, 101, 1126
- Gustafsson, B., Edvardsson, B., Eriksson, K. et al. 2008, A&A, 486, 951
- Hale, G.E. 1908, ApJ, 28, 315
- Hall, D.S. 1976, ASSL, 60, 287, *"The RS CVn binaries and binaries with similar properties"*, in Multiple Periodic Variable Stars, (Ed.) Fitch, W.S., Proceedings of the International Astronomical Union colloquium no. 29, held at Budapest, Hungary, 1–5 September 1975, p. 287, D. Reidel, Dordrecht, Netherlands; Boston, U.S.A.
- Hall, J.C. 2008, "Stellar Chromospheric Activity", *Living Rev. Solar Phys.*, 5, (2008), 2
- Hanle, W. 1924, Z. Phys., 30, 93
- Hekker, S. 2007, *"Radial velocity variations in red giant stars: pulsations, spots and planets"*, Doctoral thesis, Leiden University
- Hekker, S. & Meléndez, J. 2007, A&A, 475, 1003
- Hekker, S., Snellen, I.A.G., Aerts, C. et al. 2008, JPhCS, 118, 2058
- Hewish, A., Bell, S.J., Pilkington, J.D., Scott, P.F. & Collins, R.A. 1968, Nature, 217, 709

- Hooten, J.T. & Hall, D.S. 1990, ApJS, 74, 225
- Huang, Wenjin, Gies, D.R. & McSwain, M.V. 2010, ApJ, 722, 605
- Hurlburt, N.E., Matthews, P.C. & Proctor, M.R.E. 1996, ApJ, 457, 933
- Hussain, G.A.J., Collier Cameron, A., Jardine, M.M. et al. 2009, MNRAS, 398, 189
- Hünsch, M., Schmitt, J.H.M.M., Schröder, K.-P. & Reimers, D. 1996, A&A, 310, 801
- Hünsch, M., Schmitt, J.H.M.M. & Voges, W. 1998, A&AS, 127, 251
- Iben, I., Jr. 1964, ApJ, 140, 1631
- Iben, I., Jr. 1967 a, ApJ, 147, 624
- Iben, I., Jr. 1967 b, ApJ, 147, 650
- Iben, I., Jr. 1967 c, ARA&A, 5, 571
- Iben, I., Jr. 1991, ApJS, 76, 55
- Jardine, M., Barnes, J., Donati, J.-F., Cameron, A. 1999, MNRAS, 305, L35
- Jordan, C. & Montesinos, B. 1991, MNRAS, 252, 21P
- Kemp, J.C., Swedlund, J.B., Landstreet, J.D. & Angel, J.R.P 1970, ApJ, 161, L77
- Kochukhov, O., Drake, N.A., Piskunov, N.E. & de la Reza, R. 2004, A&A, 424, 935
- Kochukhov, O. & Wade, G.A. 2010, A&A, 513, 13
- Kochukhov, O., Makaganiuk, V., Piskunov, N.E. et al. 2011, ApJ Letters, 732, L19
- Kochukhov, O., Mantere, M.J., Hackman, T. and Ilyin, I. 2013, A&A, 550, 84
- Konstantinova-Antova, R.K., Antov, A.P. & Bachev, R.S. 2000, IBVS, 4867, 1

- Konstantinova-Antova, R.K., Antov, A.P., Zhilyaev, B.E. et al. 2005 a, AN, 326, 38
- Konstantinova-Antova, R., Aurière, M., Alecian, E. et al. 2008 a, AIPC, 1043, 405
- Konstantinova-Antova, R., Aurière, M., Iliev, I.K. et al. 2008 b, A&A, 480, 475
- Konstantinova-Antova, R., Aurière, M., Schröder, K.-P. & Petit, P. 2009, IAUS, 259, 433
- Konstantinova-Antova, R., Aurière, M., Charbonnel, C. et al. 2010, A&A, 524, 57
- Konstantinova-Antova, R., Aurière, M., Petit, P. et al. 2012, A&A, 541, 44
- Konstantinova-Antova, R., Aurière, M., Charbonnel, C. et al. 2013, BlgAJ, 19, 14
- Konstantinova-Antova, R., Aurière, M., Charbonnel, C. et al. 2014, Proceedings IAU Symposium No. 302
- Korhonen, H., Berdyugina, S.V. & Tuominen, I. 2002, A&A, 390, 179
- Kron, G.E. 1947, PASP, 59, 261
- Krticka, J., Mikulasek, Z., Zverko, J. & Ziznovsky, J. 2007, A&A, 470, 1089
- Kurucz, R.L. 1993, SAO, Cambridge, CDROM 18
- Lafler, J. & Kinman, T.D. 1965, ApJS, 11, 216
- Lagarde, N., Decressin, T., Charbonnel, C., Eggenberger, P., Ekström, S., Palacios, A. 2012, A&A, 543, A108
- Landstreet, J.D. 1992, A&A Rev., 4, 35
- Landstreet, J.D. & Mathys, G. 2000, A&A, 359, 213
- Leighton, R.B. 1969, ApJ, 156, 1
- Leroy, Jean-Louis 2000, *"Polarization of light and astronomical observation"*, vol. 4 of the Gordon and Breach Science Publishers

- Linsky, J.L. & Haisch, B. M. 1979, ApJ, 229, L27
- Linsky, J.L. 1980, ARA&A, 18, 439
- Livio, M. & Soker, N. 2002, ApJ, 571, L161
- Lockwood, G.W., Thompson, D.T., Radick, R.R. et al. 1984, PASP, 96, 714
- Lomb, N.R. 1976, Ap&SS, 39, 447
- Lopez Ariste, A. 2002, ApJ, 564, 379
- Love, J.J. 1999, Astronomy & Geophysics, Vol. 40, Issue 6, p.14
- Lozitsky, V.G., Baranovsky, E.A., Lozitska, N.I. & Leiko, U.M. 2000, Solar Phys., 191, 171
- Luck, R. Earle & Challener, Sharon L. 1995, AJ, 110, 2968
- Lüftinger, T., Fröhlich, H.-E., Weiss, W.W. et al. 2010, A&A, 509, 43
- Maeder, A. & Zahn, J.-P. 1998, A&A, 334, 1000
- Maggio, A., Favata, F., Peres, G. & Sciortino, S. 1998, A&A, 330, 139
- Marsden, S.C., Donati, J.-F., Semel, M., Petit, P. & Carter, B.D. 2006, MNRAS, 370, 468
- Marsden, S.C., Jardine, M.M., Ramirez Velez, J.C. et al. 2011, MNRAS, 413, 1922
- Marsden, S.C., Petit, P., Jeffers, S. et al. 2014, MNRAS accepted (also on 2013arXiv1311.3374)
- Massarotti, A. 2008, AJ, 135, 2287
- Massarotti, A., Latham, D.W., Stefanik, R.P. & Fogel, J. 2008, AJ, 135, 209
- Mekkaden, M.V. 1985, ASS, 117, 381
- Middelkoop, F. 1981, A&A, 101, 295
- Moffatt, H.K. 1978, "Magnetic field generation in electrically conducting fluids", Cambridge: Cambridge Univ. Press

- Morgenthaler, A., Petit, P., Morin, J. et al. 2011 a, AN, 332, 866
- Morgenthaler, A., Petit, P., Aurière, M. et al. 2011 b, ASPC, 448, 1203
- Morgenthaler, A., Petit, P., Saar, S. et al. 2012, A&A, 540, 138
- Morin, J., Donati, J.-F., Forveille, T. et al. 2008 a, MNRAS, 384, 77
- Morin, J., Donati, J.-F., Petit, P., Delfosse, X., Forveille, T. et al. 2008 b, MNRAS, 390, 567
- Morin, J., Donati, J.-F., Petit, P. et al. 2010, MNRAS, 407, 2269
- Moss, D. 2001, ASPC, 248, 305
- Mosser, B., Goupil, M.J., Belkacem, K. et al. 2012, A&A, 548, 10
- Moutou, C., Donati, J.-F., Savalle, R. et al. 2007, A&A, 473, 651
- Narain, U. & Ulmschneider, P. 1990, SSRv, 54, 377
- Narain, U. & Ulmschneider, P. 1996, SSRv, 75, 453
- Ossendrijver, M. 2003 a, ANS, 324, 64
- Ossendrijver, M.A.J.H. 2003 b, "The solar dynamo", Astron. Astrophys. Rev. 11, 287-367
- O'Neal, D., Saar, S.H. & Neff, J.E. 1996, ApJ, 463, 766
- Palacios, A., Talon, S., Charbonnel, C., & Forestini, M. 2003, A&A, 399, 603
- Palacios, A., Charbonnel, C., Talon, S. & Siess, L. 2006, A&A, 453, 261
- Palacios, A., Gebran, M., Josselin, E. et al. 2010, A&A, 516, 13
- Pallavicini, R., Golub, L., Rosner, R. et al. 1981, ApJ, 248, 279
- Parker, E.N. 1993, ApJ, 408, 707
- Pasquini, L., Randich, S., Zoccali, M. et al. 2004, A&A, 424, 951
- Petit, P., Donati, J.-F. & Colier Cameron, A. 2002, MNRAS, 334, 374

- Petit, P., Donati, J.-F. & The Espadons Project Team 2003, *"Stellar polarimetry with ESPaDOnS"* in EAS Publication Series (ed. J. Arnaud & N. Meunier), vol.9, pp.97
- Petit, P., Donati, J.-F., Oliveira, J.M. et al. 2004 a, MNRAS, 351, 826
- Petit, P., Donati, J.-F., Wade, G.A. et al. 2004 b, MNRAS, 348, 1175
- Petit, P., Donati, J.-F., Aurière, M. et al. 2005, MNRAS, 361, 837
- Petit, P., Dintrans, B., Solanki, S.K. et al. 2008, MNRAS, 388, 80
- Petit, P., Dintrans, B., Morgenthaler, A. et al. 2009, A&A, 508, L9
- Petit, P., Lignières, F., Wade, G.A. et al. 2010, A&A, 523, 41
- Petit, P., Aurière, M., Konstantinova-Antova, R. et al. 2013, LNP, 857, 231
- Pilachowski, C., Sneden, C., Freeland, E. & Casperson, J. 2003, AJ, 125, 794
- Power, J., Wade, G.A., Aurière, M., Silvester, J. & Hanes, D. 2008, Contr. Astron. Obs. Skalnaté Pleso, 38, 443-444
- Preston, G.W. 1967, ApJ, 150, 547
- Proctor, M.R.E. 2004, A&G, 45, 14
- Rees, D.E. & Semel, M.D. 1979, A&A, 74, 1
- Reiners, A. 2012, *"Observations of cool-star magnetic fields"*, Living Reviews in Solar Physics, vol. 9, no. 1
- Robinson, R.D., Worden, S.P. & Harvey, J.W. 1980, ApJ, 236, L155
- Rosén, L., Kochukhov, O. & Wade, G.A. 2013, MNRAS, 436, 10
- Saar, S.H. & Linsky, J.L. 1985, ApJ Lett., 299, 47
- Sackmann, I.-J. & Boothroyd, A.I. 1999, ApJ, 510, 217
- Sanz-Forcada, J., Brickhouse, N.S. & Dupree, A.K. 2002, ApJ, 570, 799
- Scargle, J.D. 1982, ApJ, 263, 835

- Schröder, K-P., Hünsch, M. & Schmitt, J.H.M.M. 1998, A&A, 335, 591
- Schüssler, M. 1996, IAUS, 176, 269
- Schwarzschild, M. 1975, ApJ, 195, 137
- Semel, M. 1989, A&A, 225, 456
- Semel, M., Donati, J.-F. & Rees, D.E. 1993, A&A, 278, 231
- Sennhauser, C. & Berdyugina, S.V. 2011, A&A, 529, 100
- Setiawan, J., Pasquini, L., da Silva, L. et al. 2004, A&A, 421, 241
- Setiawan, J., von der Lühe, O., Pasquini, L. et al. 2005, ESASP, 560, 963
- Shibahashi, H. 2004, in "The A-Star Puzzle", proceedings IAU Symposium N_0 224, J. Zverko, J. Ziznovsky, S.J. Adelman, W.W. Weiss, eds. (Cambridge University Press, Cambridge), 451
- Siess, L. & Livio, M. 1999, MNRAS, 308, 1133
- Silvester, J., Wade, G.A., Kochukhov, O. et al. 2012, MNRAS, 426, 1003
- Simon, T., Linsky, J.L. & Stencel, R.E. 1982, ApJ, 257, 225
- Simon, T. & Fekel, F.C. 1987, ApJ, 316, 434
- Simon, T. & Drake, S.A. 1989, ApJ, 346, 303
- Skilling, J. & Bryan, R.K. 1984, MNRAS, 211, 111
- Skumanich, A. 1972, ApJ, 171, 565
- Skumanich, A., Smythe, C. & Frazier, E.N. 1975, ApJ, 200, 747
- Smith, M.A. & Dominy, J.F. 1979, ApJ, 231, 477
- Spurr, A.J. & Hoff, D.B. 1987, IBVS, 3028, 1
- Stepień, K. 1993, ApJ, 416, 368
- Stepień, K. 2000, A&A, 353, 227
- Stibbs, D.W.N. 1950, MNRAS, 110, 395

- Stokes, G.G. 1852, *Trans. Cambridge Philos. Soc.*, 9, 399, 416
- Strassmeier, K.G. & Hall, D.S. 1988, ApJS, 67, 453
- Strassmeier, K.G., Fekel, F.C., Bopp, B.W., Dempsey, R.C. & Henry, G.W. 1990 a, ApJS, 72, 191
- Strassmeier, K.G., Hall, D.S., Barksdale, W.S., Jusick, A.T. & Henry, G.W. 1990 b, ApJ, 350, 367
- Strassmeier, K.G. 1997, A&A, 319, 535
- Strassmeier, K.G., Stepień, K., Henry, G.W. & Hall, D.S. 1999, A&A, 343, 175
- Strassmeier, K.G. 2002, AN, 323, 309
- Strugarek, A., Brun, A.S. & Zahn, J.-P. 2011 b, A&A, 532, 34
- Tautvaišiene, G., Edvardsson, B., Tuominen, I. & Ilyin, I. 2000, A&A, 360, 499
- Tautvaišiene, G., Edvardsson, B., Puzeras, E. & Ilyin, I. 2005, A&A, 431, 933
- Thevenin, F. 1998, VizieR Online Data Catalog, 3193, 0
- Théado, S., Vauclair, S. & Cunha, M.S. 2005, A&A, 443, 627
- Thompson, S.D. 2005, MNRAS, 360, 1290
- Tomkin, J., Lambert, D.L. & Luck, R.E. 1975, ApJ, 199, 436
- Tsvetkova, S., Petit, P., Aurière, M. et al. 2013, A&A, 556, 43
- van Leeuwen, F. 2007, A&A, 474, 653
- Vaughan, A.H., Preston, G.W., Wilson, O.C. 1978, PASP, 90, 267
- Vaughan, A.H., Preston, G.W., Baliunas, S.L. et al. 1981, ApJ, 250, 276
- Vernazza, J.E., Avrett, E.H. & Loeser, R. 1981, ApJS, 45, 635
- Vilhu, O. 1984, A&A, 133, 117
- Vogt, S.S. & Penrod, G.D. 1983, PASP, 95, 565

- Wade, G.A., Donati, J.-F., Landstreet, J.D. & Shorlin, S.L.S. 2000 a, MNRAS, 313, 823
- Wade, G.A., Donati, J.-F., Landstreet, J.D. & Shorlin, S.L.S. 2000 b, MNRAS, 313, 851
- Walter, F.M. & Bowyer, S. 1981, ApJ, 245, 671
- Wilson, O.C. 1968, ApJ, 153, 221
- Wilson, O.C. 1978, ApJ, 226, 379
- Wolff, S.C. 1968, PASP, 80, 281
- Wright, J.T., Marcy, G.W., Butler, R.P. & Vogt, S.S. 2004, ApJS, 152, 261
- Young, A., Ajir, F. & Thurman, G. 1989, PASP, 101, 1017
- Zahn, J.-P. 1992, A&A, 265, 115
- Zeeman, P. 1897, ApJ, 5, 332